Rogue waves in the Dutch North Sea

An experimental study into the occurrence of extreme waves due to abrupt depth transitions at future offshore wind farm locations along the Dutch coast

M.W. Doeleman

Rogue waves in the Dutch North Sea

An experimental study into the occurrence of extreme waves due to abrupt
depth transitions at future offshore wind farm locations along the Dutch
coast

by

M.W. Doeleman

In partial fulfillment of the requirements for the degree of

Master of Science
in Hydraulic Engineering

at the Delft University of Technology,
to be defended publicly on April 14th

Studentnumber:	4453549
Project duration:	September 2020 - April 2021

Thesis committee:	Prof. Dr. Ir. A.J.H.M. Reniers	TU Delft, Chair
	Dr. Ir. T.S. van den Bremer	TU Delft, Supervisor
	Dr. Ir. B. Hofland	TU Delft
	Ir. M. Westra	MetOcean Consult
	Dr. J. Groeneweg	Deltares

TUDelft

Preface

For as long as I can remember I have spent my summer holidays sailing. The hours of looking at waves in the IJsselmeer, Wadden Sea and North Sea are in-numerous. The sound of the waves near the boat and the wind blowing in the sails gives a certain kind of relaxation and a feeling of happiness. It is therefore not that strange that I have developed a great interest into wave dynamics.

During the course Ocean Waves, which is part of the Master's program Hydraulic Engineering, I first learned about the existence of rogue waves. The phenomenon immediately caught my attention and I am grateful to have been able to write my thesis on this subject.

M.W. Doeleman

Delft, March 2021

Summary

Large morphological features, so-called sand ridges, with an average height and length in the order of 10 meters and 3 kilometers respectively are located at future offshore wind farm locations in the Dutch North Sea. Recent literature, considering relatively deep water conditions ($kh \approx 1$, with k the wave number and h the water depth), has shown that a wave field propagating over a shallowing depth transition shows an increase in kurtosis. Kurtosis is a measure for the vertical deviation from the commonly applied linear ocean wave model, and therefore describes a higher probability of occurrence of "rogue" waves. These "rogue" waves are known to the general public from sailors' tales and thrilling videos. Scientifically, rogue waves are described as statistically abnormal waves and are generally classified as waves that exceed twice the significant wave height. Because these waves have an abnormal height, they are associated with extreme forces. Considering the sand ridges at future offshore wind farm locations, and possible increased damages to wind turbines due to rogue waves, it is questioned if the increased probability of occurrence of rogue waves due to the local bathymetry as observed in the relatively deep water literature also applies to relatively shallow water conditions and the Dutch North Sea.

To achieve this objective, literature is reviewed and physical experiments have been performed at the Hydraulic Engineering laboratory at the Delft University of Technology. The literature review consists, amongst others, of the elaboration and evaluation of an existing statistical model developed by Li et al. (2020b). This model is valid for narrow-banded wave fields up to second-order in steepness in a relatively deep regime ($kh > 0.5$). The model describes a rogue wave mechanism as the interaction between the transmitted wave field and second-order components: the free sub- and super-harmonic components generated by the depth transition. Using the model, predictions of the peak kurtosis are obtained for typical regular ($T_p = 7$ seconds (Bosboom and Stive, 2012), with T_p the peak wave period) and storm ($T_p = 12$ seconds (Paulsen et al., 2019)) wave North Sea conditions ($k_p h \approx 1$).

The physical experiments are scaled on the long wave field ($T \approx 25$ seconds) measured some minutes prior to a potential rogue wave event. This wave record was measured by a wave buoy in the vicinity of a sand ridge (depth transition) in the North Sea. The experimental study subsequently considers a relatively shallow regime ($kh < 0.5$) and therefore contributes to the knowledge gap in current (relatively deep water) literature. The experiments consist of highly idealised irregular wave tests using Gaussian wave spectra valid up to second order in steepness for a steep (step) and gentle (1:20 slope) depth transition. The experimental results are compared to the prediction of the statistical model and it is found that, for tests within the model limits, the prediction matches the laboratory observations. Also, it is shown that the experimental results with a step and slope are equal. This result is not in accordance with observations made in relatively deep water studies, where it is shown that gentler slopes show a reduced increase in kurtosis (Gramstad et al., 2013; Zheng et al., 2020; Viotti and Dias, 2014; Zeng and Trulsen, 2012). Furthermore, all experiments, including tests exceeding the steepness limit, have shown a significant increase in kurtosis down-wave of the depth transition. Also, each test shows that this increase in kurtosis is described with a distinct bell-shape, which is in accordance with the statistical model prediction.

As the sand ridges in the North Sea (with some exceptions) have an approximate slope of 1:200, which according to literature reduces the peak kurtosis significantly in relatively deep water, it is concluded that for regular North Sea conditions no increase in kurtosis (the probability of occurrence of rogue waves) is expected. Considering North Sea storm conditions, the typical wave field is described with a longer peak wave period and could therefore, at some times, approach relatively shallow water conditions (wave fields consist of a range of frequencies). Because the physical experiments have shown no influence of slope for relatively shallow water conditions, an increase in kurtosis is expected for storm conditions if these long waves ($T \approx 25$ seconds) indeed (frequently) occur. For this reason it is recommended to research the data of the wave buoy that measured the potential rogue wave to obtain accurate (regular and) storm wave conditions. Using these conditions, the model predictions, and laboratory observations, a definite answer can be given to the question if rogue waves occur in the Dutch North Sea due to the local bathymetry.

Contents

List of symbols

Parameter	Unit	Description
a	m	Amplitude
$a(f)$	m/Hz	Amplitude spectrum
A	m	Envelope surface elevation signal
c_g	m/s	Group velocity
d	m	Water depth
$E(f)$	m^2/Hz	Spectral density
f	Hz	Frequency
g	m/s^2	Gravitational acceleration
h	m	Water depth
h_d	m	Deeper water depth
h_s	m	Shallower water depth
H	m	Wave height
H_s	m	Significant wave height
k	m^{-1}	Wave number
k_p	m^{-1}	Wave number following peak wave period
k_0	m^{-1}	Wave number
L	m	Wave length
$L_{0,p}$	m	Deep water wave length
m_0	m^2	First order spectral moment, variance
n_f	-	Froude scaling factor
N	-	Number of waves
s	-	Skewness
$s_{0,p}$	-	Wave steepness
$S(f)$	m^2/Hz	Spectral density
T	s	Wave period
T_p	s	Peak wave period
x	m	Distance
X_{11}	m	First order paddle movement
X_{10}	m	Sub-harmonic paddle movement
α	rad/s	angular frequency
δ	-	Spectral bandwidth
ϵ	rad	Phase
ϵ_d	-	Wave steepness deep water side
ζ	m	Surface elevation
η	m	Surface elevation
η_c	m	Crest elevation
ϕ	rad	phase
Φ	m^2/s	Velocity potential
κ	-	Kurtosis
λ	m	Wave length
ρ	-	Correlation coefficient
σ	-	Standard deviation
ϕ	rad	Phase
ω	rad/s	Angular frequency

<div align="right">

1

</div>

<div align="right">

Introduction

</div>

In this chapter first a brief history of rogue waves is given to enthuse the reader on this topic. Hereafter, the problem description is given. Next, the scope is described. Following, the objective and research questions are shown. Hereafter, the research approach is explained and last, the thesis outline is described.

1.1 Brief history of rogue waves

For decades the existence of so-called "rogue" or statistically abnormal waves has been ignored by scientists. Stories of seaman that reportedly encountered unexpected and unusually large waves were labelled as myths (Collins, 2013; The European Space Agency, 2004b; Liu, 2007). In a story told by Captain Ronald Warwick of the cruise liner *Queen Elizabeth II* after experiencing a 29-meter rogue wave in 1995, he described the wave as "a great wall of water - it looked as if we were going into the White Cliffs of Dover" (The European Space Agency, 2004b; Liu, 2007). In contrast to the seaman that could tell their stories ashore, it is assumed that several large vessels with their crew were lost at sea due to the presence of huge waves. For example, in 1978 the at the time largest ship ever built and -claimed to be- unsinkable super-tanker *MS München* with her 26 crew members disappeared. All that was found was a severely damaged lifeboat. (Liu, 2007)

A few rogue (or also called extreme, killer, freak and monster) waves and their damage done to vessels have been photographed since the late 1960s. Figure 1.1 shows the *World Glory* tanker carrying thousands of tons of crude oil in 1968 after being broken in half due to the encounter with an extreme wave. The whole tanker, located 105 kilometers east of Durban, South Africa, sunk within four hours (Liu, 2007).

Figure 1.1: Sinking of the World Glory tanker in 1968 (Parker, 2020)

In 1977 a chemical tanker called *Stolt Surf* sailing from Singapore to Portland got caught in a storm and encountered huge waves. An on-board Danish photographer Karsten Peterson took pictures (figure 1.2) of the event and said; "when the big waves came crashing towards us, we had to look UP in order to see the top of the waves! And that was from the bridge deck, which is already 22 meters above sea level!" (Liu, 2007). Another rare photo of a rogue wave was taken in 1980 by first mate Philippe Lijour aboard the supertanker *Esso Languedoc*, figure 1.3. It was reported that during a storm off the coast of Durban, South Africa, a wave approached the ship from behind after which it started breaking over the deck. The mast on starboard has a height of 25 meters above mean sea level. The mean wave height at the time was said to be just 5 to 10 meters (Liu, 2007; The European Space Agency, 2004a).

Figure 1.2: 1977 the Stolt Surf, picture taken by Karsten Peterson (The New York Times, 2006)

Figure 1.3: 1980 the Esso Languedoc, picture taken by Philippe Lijour (The European Space Agency, 2004a)

One of the most famous and frequently shown photographs when talking about the impact of rogue waves is the damaged bow of the Norwegian tanker *Wilstar*, figure 1.4. The tanker is known to have encountered a rogue wave in the Agulhas current. (Liu, 2007; Kharif et al., 2009) This photograph clearly shows the forces that come along with these large steep/breaking waves.

Figure 1.4: Damaged bow of the Norwegian tanker Wilstar (Kharif et al., 2009)

It took until New Years Day 1995 when a rogue wave was measured by the Draupner E oil platform to draw the attention of researchers. The oil platform, owned by Statoil, took measurements of the wave height because it used a new foundation technology which the company wanted to monitor. According to the laser-based wave height measurements an extreme wave of 26 meters was measured in a sea with a significant wave height, H_s of 12 meters (Røsjø, B. and Hauge, K., 2011; Bidlot et al., 2016). H_s is the average of the highest 1/3 of the waves in a wave record of a length of 15-30 minutes. Rogue waves, according to the rogue wave criteria, can be classified as waves that are larger than $2H_s$. This will be elaborated in section 2.2. The wave height measured at Draupner E had a ratio of $H/H_s = 2.24$ and can thus be classified as a rogue wave (Kharif et al., 2009).

The measured wave signal, which is duplicated from Walker et al. (2004) can be observed in figure 1.5. The signal is measured on January 1st in 1995 from 15:20 until 16:20. The peak can clearly be observed. Remarkable is the sudden appearance of the event. It would be expected that two to three other large waves precede the extreme wave however, this is not the case. Seemingly, the occurrence of the extreme wave cannot be related to the prevailing wave conditions (Holthuijsen, 2007). This caught the interest of scientists and still until today extensive research is performed to understand the physics behind this phenomenon. The Draupner event also lead to the review of ship and wind turbine design as the existence of these statistically abnormal powerful waves had now been proven (Smith, 2007; Røsjø, B. and Hauge, K., 2011).
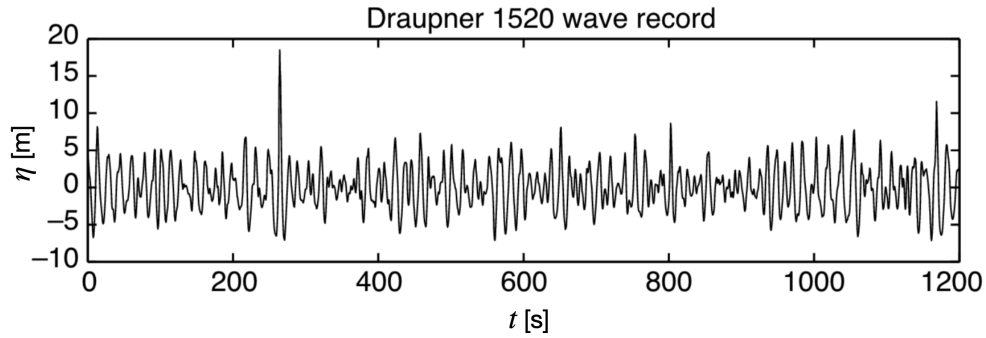
Figure 1.5: Draupner wave record (Walker et al., 2004)

Following this brief historical overview, three definitions of rogue waves can be identified. First, the thrilling definition which describes rogue waves by sailors' stories, photographs and videos that involve huge waves. Second, the rogue wave criteria which describe the unexpectedly large wave height of the considered wave with respect to the total wave record. And last, the fully statistical description, which classifies rogue waves as waves that do not comply with the currently used linear model for ocean waves. The last two definitions of rogue waves are especially of interest to researchers and will be further elaborated in chapter 2.

1.2 Problem description

During a recent measurement campaign, funded by the Netherlands Enterprise Agency (RVO), a remarkable wave has been recorded, see figure 1.6. The measurement campaign was set-up in order to gain more information about, amongst others, wave and soil conditions at future offshore wind farm locations in the Dutch North Sea (RVO, 2020). It can be seen in figure 1.6 that the wave crest has an exceptional height of 15 meters. Noticeable is the cut-off at the trough and crest at exactly -15 and 15 meters. This could be due to measurement limitations of the buoy and would mean that the actual wave height was even larger than 30 meters. This enormous wave can undoubtedly be classified as an unexpectedly large wave following the rogue wave criteria ($H > 2H_s$, with H and H_s the wave height and significant wave height respectively. For an elaborate definition of rogue waves please see chapter 2). It must be noted, however, that besides the rogue wave explanation, the wave could also be the result of a measurement or processing error. As the deployed buoys register accelerations (pitch, roll, heave) and the heading, thus not the actual wave height in time, it could be possible that a breaking wave (which would however also indicate an extreme event) on top of the buoy could have lead to large accelerations (Brijder, 2020). Processing these sudden and large accelerations to a surface elevation time series could have resulted in the large wave as shown in figure 1.6. In addition, the 30 meters wave could be an artefact as a result of the applied processing methods. As it is, at this moment, unclear whether the exceptional wave is a measurement error, a processing artefact or a 'true' rogue wave, this research tries to find out if the last explanation could be substantiated.
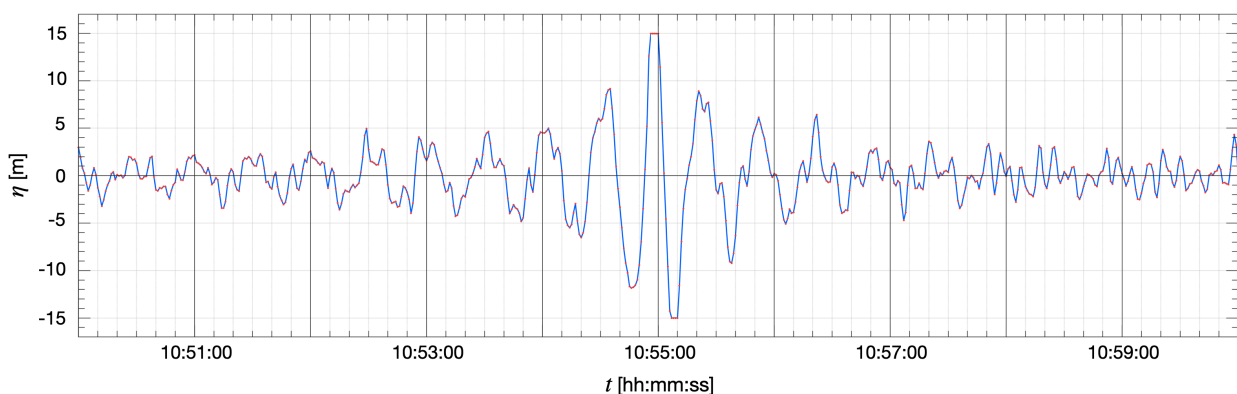

Figure 1.6: Possible rogue wave event measured in the North Sea area by buoy HKWA located 52°34'N 3°43'E at 10:55 11th of February 2020.

According to recent literature, rogue waves can occur more frequently with respect to linear theory in the vicinity of steep bottom topography (Gramstad et al., 2013; Trulsen et al., 2012; Adcock and Taylor, 2014). Using the seabed map presented in figure 1.7, one can observe that depth transitions are present in the Dutch North Sea. The depth transitions are large morphological features, so-called "sand ridges", that have an average height and width in the order of 10 meters and 3 kilometers respectively. Furthermore, it can be observed that the average water depth h is approximately 30 meters. In addition to the bathymetry, figure 1.7 also shows the locations of future wind farm locations with the exception of wind farm Waddensea North. In order to comply with the energy agreement for sustainable energy, the Dutch government decided to invest in offshore wind energy. Current wind farms, OWEZ, PAWP, 'Luchterduinen' and 'Gemini' supply up to 957 MW. Wind farm locations part of the 2023 roadmap include Borssele, Hollandse Kust (HK) South ('Zuid') and HK North ('Noord'). These wind farms will provide an additional 3500 MW to the current energy supply. In the long term, following the roadmap until 2030, wind farms are scheduled at HK West, IJmuiden Ver and North of the Waddensea. These three locations are designed to supply an additional 6100 MW (Rijksoverheid, 2020; Noordzeeloket, 2020). Besides these planned wind farm locations, figure 1.7 also shows some nameless lots North and South of HK West that might be used in the future. It can be observed that significant sand ridges are present at the wind farm locations indicated with bold lines. Figure 1.7 also shows the location of the wave buoy that measured the potential rogue wave signal which is shown in figure 1.6. Remarkable is that the buoy is located near a sand dune. Considering the observations made in recent literature, it is hypothesised that rogue waves occur more frequently at these offshore wind farm locations with strongly varying bathymetry.
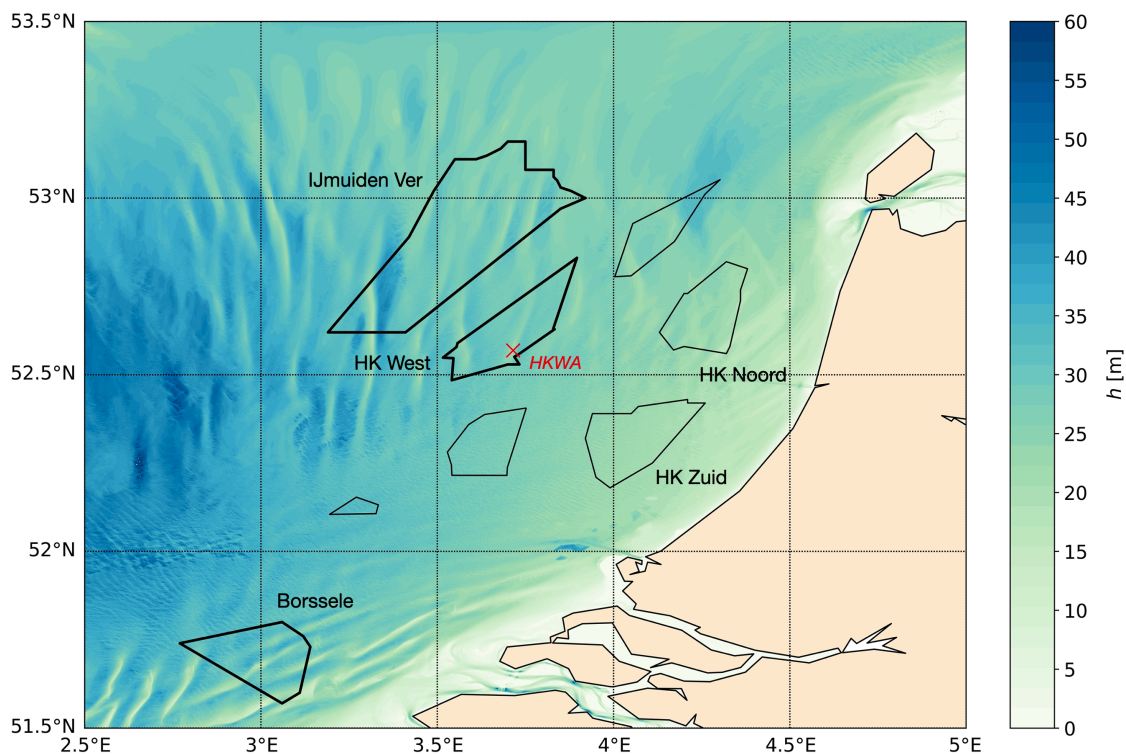
Figure 1.7: Bathymetry of the Dutch West coast and future offshore wind farm locations (EMODnet, 2020). h Is the water depth in meters, HK denotes 'Hollandse Kust' and the wave buoy HKWA is indicated with a red cross.

Besides the question if rogue waves occur more frequently at these offshore wind farm locations, it must be questioned why it is important to know how often/if rogue waves occur at future wind farm locations? Stansell (2004) and Guedes Soares et al. (2003) stressed that although the occurrence of rogue waves is rare, these waves pose a severe threat to offshore structures. One extremely large wave causes more damage than several "normal" large waves. So, when rogue waves have a relatively high probability of occurrence due to the local bathymetry, wind turbine design might become more expensive than expected. For this reason, the mechanism(s) behind rogue wave formation and consequently their probability of occurrence must be understood.

1.3 Scope

Over the past few years, several physical mechanisms leading to the occurrence of rogue waves have been derived. According to Dysthe et al. (2008) and Kharif and Pelinovsky (2003) there are basically three categories that are all based on the focusing of energy; spatial focusing, temporal-spatial focusing and nonlinear focusing. The first category, spatial focusing, includes the effects of waves propagating over a certain bottom topography and wave-current interaction. Temporal-spatial or dispersive focusing is the focusing of waves in a group with steadily decreasing frequency. At some point in time, the wave group has decreased to its minimum in size and a maximum crest is expected. The last category, nonlinear focusing, is the effect of the Benjamin-Feir (BF) instability. The result of this instability is the break up of a regular wavetrain into periodic groups. As the periodic groups slowly but continuously focus further, at some moment in time a very large wave occurs. In this thesis, only the physical mechanism of the first category; spatial focusing, and more specifically, interaction with bottom topography is considered. This mechanism, as explained in the problem description, is a potential candidate for the event shown in figure 1.6.

In order to investigate this mechanism, highly idealised experiments valid up to second order in steepness with relatively small dimensionless water depths and Gaussian wave spectra are performed. Current literature has thoroughly investigated the effects of bottom topography in a relatively deep regime. This thesis will contribute to this knowledge as, on the contrary to the traditional deep water rogue wave studies, a relatively shallow environment ($kh < 0.5$, where k is the typical wavenumber and h the water depth) is examined. The experiments are performed at the Hydraulic Engineering laboratory of the Delft University of Technology. In addition to commonly used wave gauges to measure the surface elevation, a 2D Laser scanner is used to assess its potential in the laboratory. Last, this thesis also contributes to second-order sub-harmonic wave generation at the TU Delft facility, which is considered important for the investigation of the rogue wave mechanism.

1.4 Objective and research questions

The objective of this thesis is to find out if a higher probability of occurrence of rogue waves atop a depth transition, as has been found in recent studies for deeper water, is also valid for a relatively shallow environment, and more specifically, the Dutch North Sea. The main research question is therefore:

Can rogue waves arise as a result of the local bottom topography at the location of future offshore wind farms along the Dutch coast?

In order to answer the main research question, the following sub-questions are formulated:

1. Is there existing evidence of rogue wave occurrence in the North Sea?

2. What are the simplifications and limitations of the physical model that is scaled to a potential rogue wave event in the North Sea?

3. Can an existing model based on narrow-banded second-order theory explain laboratory observations?

    (a) For typical North Sea wave periods

    (b) For long wave periods

1.5 Research approach

This thesis consists of a literature review and an experimental study. The literature study describes the basics of wave statistics and the rogue wave criteria. In addition, rogue wave studies that used data from the North Sea are discussed which is of importance to the first research sub-question. Hereafter, literature on rogue waves in the vicinity of depth transitions is discussed. This section clearly shows the knowledge gap in the relatively shallow water region. Last, an existing theoretical framework (or also called statistical model) valid up to second-order in steepness considering narrow banded wave spectra and relatively deep water conditions is evaluated. This section in combination with the results of the experiments is used to answer the third sub-question.

The experimental study consists of highly idealised irregular wave tests using Gaussian wave spectra valid up to second order in steepness with relatively small dimensionless water depths. The tests are performed at the Hydraulic Engineering laboratory facility of the Delft University of Technology. Because it is predicted by the statistical model that bound sub- and super-harmonic waves play an important role in the rogue wave mechanism, the second-order wave generation (important for correct generation of the bound components) at the laboratory is assessed and corrected before the rogue wave tests were performed. The experimental program is scaled in accordance with the long wave field measured some minutes prior to the potential rogue wave shown in figure 1.6. To obtain a broad understanding of the wave-bathymetry interaction, the water depths, spectral width, slope of the bathymetry and steepness are varied. As the obtained wave data is "raw" the surface elevations and velocities are first processed and analysed before the data is compared with the theoretical framework. The main research question will be answered using the results of the physical experiment, predictions of the evaluated model, relevant literature and by keeping the simplifications and limitations of the experiments in mind.

1.6 Thesis outline

In chapter 2 the literature review is presented. In this chapter an existing theoretical framework which has already been tested for deepish water will be discussed. In chapter 3 the experimental set-up is elaborated. In this chapter the scaling of the experiment will be explained and the lay-out, instrumentation and the experimental program will be shown. Chapter 4 elaborates on the second-order wave generation, which is considered important for assessing the rogue wave mechanism, at the laboratory facility of the TU Delft. In chapter 5 the method to process the obtained "raw" data from the flume will be presented. In chapter 6 the processed data is analysed in order to verify if the desired (input) waves match the waves in the flume. In chapter 7 the results of the experiment will be shown and compared with the theoretical framework. Chapter 8 presents the conclusions discussion and recommendations.
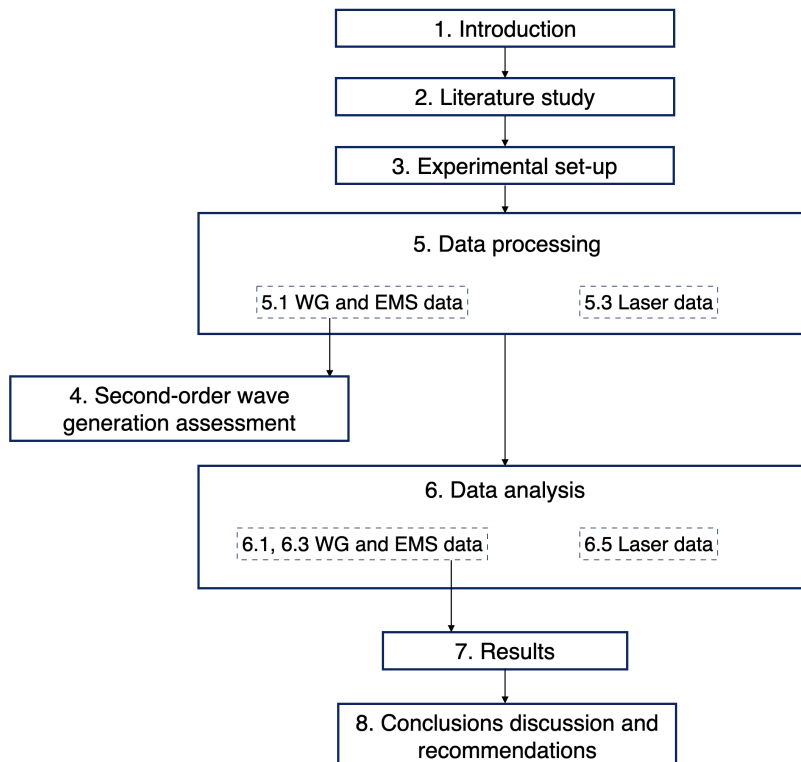

Figure 1.8: Schematic thesis outline

2

Literature review

In this chapter the basic principles of wave description and wave statistics will be repeated. Hereafter criteria to identify rogue waves are discussed. Following, relevant literature of rogue waves in the North Sea and the vicinity of depth transitions is summarised. Next, a theoretical framework derived in a study to be published will be elaborated and its relevance will be discussed.

2.1 Wave description

The generally used model for describing the (1D) sea surface elevation is the random phase/amplitude model. This model assumes that the sea surface elevation η can be described as the sum of an infinite amount of harmonic waves with an amplitude a and phase ϕ randomly chosen from a Rayleigh and uniform distribution respectively. This is described by equation 2.1, where the underbar denotes random variables and f frequency. This equation is illustrated in figure 2.1. For the description of a wave field in 3D, one can imagine that this sum also includes different directions of propagation. (Holthuijsen, 2007)

$$\underline{\eta}(t) = \sum_{i=1}^{N} \underline{a}_i cos(2\pi f_i t + \underline{\phi}_i) \tag{2.1}$$
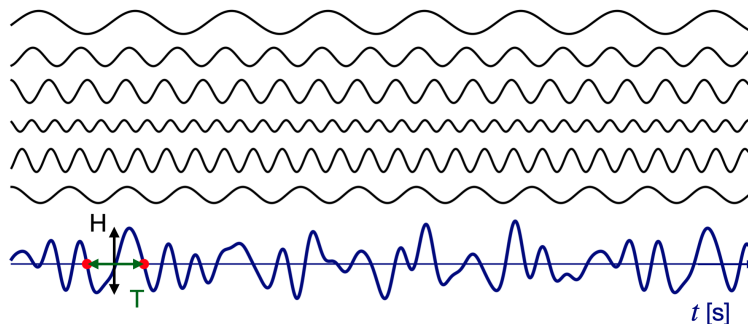
Figure 2.1: Surface level elevation (blue) as a function of the sum of harmonics (black) according to the random phase/amplitude model. The downward zero-crossing wave period T and wave height H are shown in green and black respectively.

Figure 2.1 also shows that the definition of a wave in a wave record is not that straightforward. Generally, the wave height is determined by two downward zero-crossings, which means that the wave height is the difference between the lowest trough and highest crest between two downward crossings of the mean surface elevation. This is illustrated by the red dots in the figure. Similarly, the wave height for upward zero-crossings can be found where the wave height is the difference between the highest crest and lowest trough for two upward crossings of the mean surface elevation. The wave period is the time between two downward or upward zero-crossings. For a Gaussian distributed surface elevation, the wave heights and periods for both methods are statistically the same. (Goda, 2000; Holthuijsen, 2007)

To arrive at the amplitude spectrum, random phases from a uniform distribution and random amplitudes from a Rayleigh distribution are drawn for a series of frequencies. By plotting the expected value of the amplitude against the series of frequencies the amplitude spectrum is obtained. In this spectrum, it can thus simply be seen what the expected amplitude is for each frequency. Therefore, in case of a "regular" sea (a very small range

of frequencies causing wave group formation) the spectrum is narrow and for an irregular sea, which has been stirred by winds coming from multiple directions, the spectrum is wide, see figure 2.2. The amplitude spectrum itself however is not commonly used as the amplitude cannot directly be linked to statistical properties. For this reason, the amplitude is rewritten into the variance, which is by definition the average of the squared surface elevation relative to its mean and therefore the square root of the standard deviation. Equation 2.2 shows the variance for a discrete variance spectrum $E(f)$. The overbar means time averaging.

$$\overline{\underline{\eta}^2} = E\{\underline{\eta}^2\} = \sum_{i=1}^{N} E\{\frac{1}{2}\underline{a}_i^2\} \quad \text{for} \quad E\{\underline{\eta}^2\} = 0 \tag{2.2}$$

For a continuous spectrum, all frequencies included, the total variance can be described by equations 2.3 and 2.4.

$$E(f) = \lim_{\Delta f \to 0} \frac{1}{\Delta f} E\{\frac{1}{2}\underline{a}_i^2\} \tag{2.3}$$

$$\overline{\underline{\eta}^2} = \int_0^\infty E(f) df \tag{2.4}$$
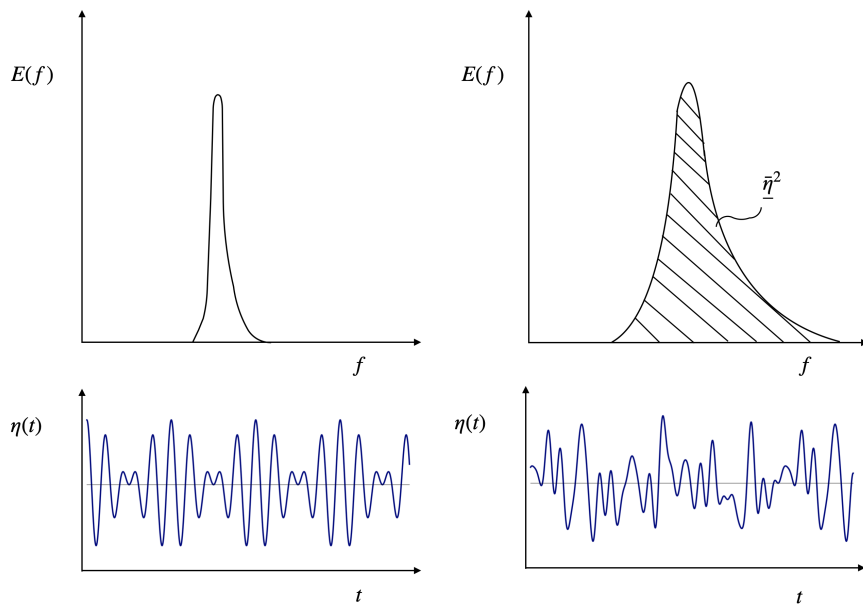
Figure 2.2: Variance density spectrum $E(f)$ and surface elevation $\eta(t)$. The left figures show a narrow spectrum and thus a "regular" groupy sea. The right figures show a broad spectrum and consequently an irregular sea surface in which wave groups are more difficult to identify.

2.1.1 *Wave statistics*

The significant wave height H_s has been introduced in chapter 1 as a relevant parameter which is equal to the mean of the highest one-third of the waves ($H_{1/3}$) in a wave record of approximately 20 minutes. The significant wave height can also be defined using two different methods; visually H_v and statistically H_{m0}, which is about the same height as $H_{1/3}$ for deep water waves. This last definition is commonly used in scientific research and will be further elaborated.

Using the assumption that the surface elevation η is a stationary Gaussian process described by a narrow spectrum (see equation 2.5 for the probability density function of the surface elevation), the probability density function of the wave height ($H = 2\eta_c$ with η_c the wave crest height) can be described by the Rayleigh distribution, see equation 2.6. Derivation of the statistical or also called spectral significant wave height using the Rayleigh

distribution therefore results in $H_{m_0} \approx 4\sqrt{m_0}$. m_0 Is equal to the squared root of the standard deviation and equal to the total variance as shown in equation 2.4 (Holthuijsen, 2007; Kharif and Pelinovsky, 2003).

$$p(\eta) = \frac{1}{\sqrt{2\pi m_0}} \exp(-\frac{\eta^2}{2m_0}) \tag{2.5}$$

$$p(H) = \frac{H}{4m_0} \exp -\frac{H^2}{8m_0} \tag{2.6}$$

Using the Rayleigh distribution, the probability of a wave whose wave height, H is larger than a certain wave height, H_0 can be estimated following see equation 2.7. (Onorato et al., 2013; Holthuijsen, 2007; Kharif and Pelinovsky, 2003)

$$P(H > H_0) = \int_{H0}^{\infty} \frac{H}{4m_0} \exp(-\frac{H^2}{8m_0}) dH = \exp(-\frac{H_0^2}{8m_0}) \approx \exp(-2\frac{H_0^2}{H_s^2}) \tag{2.7}$$

The probability of a wave to be larger than twice the significant wave height according to equation 2.7 is 1/2981. It follows that for a storm with an average wave period of 12 seconds it is probable that once every 10 hours a wave larger than $2H_s$ will occur. Logically, the probability of exceedance also depends on the storm duration and similarly, the number of waves. Equation 2.8 below shows the probability of H exceeding H_0 including the number of waves N in duration D (Holthuijsen, 2007). It follows from equation 2.8 that for $N = 2981$ and $H_0 = 2H_s$ the probability of H exceeding twice the significant wave height is 63%.

$$P(H > H_0)_D \approx 1 - (1 - \exp(-2\frac{H_0^2}{H_s^2}))^N \tag{2.8}$$

In addition to the short-term wave statistics briefly summarised above, statistical methods have also been developed for the long-term (considering the surface elevation over tens of years or more) to determine design conditions or to find changes in the wave climate. As the timescale of the long term statistics is, logically, much longer, the stationary assumption is not valid anymore and a different approach is necessary. These methods include; the initial-distribution approach, the peak-over-threshold approach and the annual-maximum approach. In all methods a statistical distribution is fitted through the data in order to extrapolate and find for example the significant wave height with a return period of 200 years. Common distributions include the Exponential, Weibull, Gumbel, Generalised Pareto, Generalised Extreme value and the Log-Normal distribution. As in the long term statistical methods only parameters such as the significant wave height, period and mean wave direction are considered and thus not a time series of the surface elevation, which is relevant for rogue waves, these methods will not be further elaborated. (Holthuijsen, 2007)

What is interesting, however, is the combination of the short- and long-term wave statistics (Mackay and Johanning, 2018; Forristall, 2008). Using a combination of both an estimation of the individual maximum wave height over a long period can be made. As mentioned in the previous paragraph, a limitation of short term wave statistics is that the stationary assumption has been made. This is however not true when one considers a long period. Following, it has been found that the Rayleigh distribution (accepted for short wave statistics) generally slightly over-predicts the occurrence probability of the highest waves (equations 2.7 2.8) (Forristall, 1978). For this reason, alternative distributions have been derived in order to describe individual wave heights over a long period more accurately. Two examples are the Forristall distribution and the Battjes method which both use the Weibull distribution with different parameters (Holthuijsen, 2007; Forristall, 1978). In this thesis, the experimental results will be compared to the Rayleigh distribution as the waves in the flume are described by a stationary process.

2.2 Identifying rogue waves

As mentioned in the introduction, three definitions of rogue waves can be distinguished. First, the thrilling definition which uses stories, photographs and videos of huge waves. Second, the use of rogue wave criteria and

last, the definition that rogues are statistically abnormal waves considering the commonly used linear model. In this section, the last two definitions which are relevant to scientific research are elaborated.

The commonly used rogue wave criteria that define a wave as rogue are $H/H_s > 2$ or $\eta_c/H_s > 1.25$ where H is the height of the rogue wave, η_c is the crest height of the rogue wave and H_s is the significant wave height. These criteria describe the unexpectedly large wave height of the considered wave with respect to other waves in the record. The ratio of H/H_s is often also called the abnormality index (AI). An AI larger than 2 logically means that the considered wave can be classified as a rogue wave (Trulsen, 2018; Kharif et al., 2009; Adcock and Taylor, 2014). Waves that satisfy both criteria are often called 'double rogue waves'. (Krogstad et al., 2008)

Considering the statistical definition, it is shown in section 2.1.1 that the probability of occurrence of a rogue wave in a storm of 2981 waves (10 hours with a 12 second wave period) is 63% and thus quite significant. As clearly the occurrence, based on Gaussian statistics and therefore the Rayleigh distribution, of rogue waves is not that rare, the criteria seem rather unsatisfactory. What does interests researchers however is the sudden appearance of these waves (deviation from the expected evolution/isolated waves) and when there are more extreme waves than would be expected by the linear, Gaussian model (Adcock and Taylor, 2014; Holthuijsen, 2007).

To measure the last, the kurtosis of the probability density distribution is a useful parameter (Mori and Janssen, 2006). The kurtosis ("tailedness") is a measure for the tail of a probability density distribution and therefore defines the contribution of large waves in a wave record. For a Gaussian sea, the kurtosis is equal to three. So if a sea has a higher value of the kurtosis, the Gaussian model will underpredict the probability of an extreme event (Schober and Calini, 2016). Another parameter that summarizes statistical properties of the surface elevation is the skewness. Skewness is an indicator of horizontal asymmetry in the wave record and thus a measure for non-linearity and therefore second-order effects (Fernandez et al., 2016). For waves with shallow and flat troughs and high and sharp crests the probability density function will be negatively (relative to the mean) *skewed*. Also, the tail for the positive surface elevation is larger (higher crests) and the tail for the negative surface elevation (shallower troughs) is smaller. The skewness and kurtosis can be described by the third- and fourth-order statistical moments of the probability density function of the surface elevation by equation 2.9 and 2.10 respectively. The overbar denotes the time-averaged value. (Schober and Calini, 2016)

$$s = \sum_{j=1}^{N} \frac{(\eta_j - \bar{\eta})^3}{N\sigma^3} \tag{2.9}$$

$$\kappa = \sum_{j=1}^{N} \frac{(\eta_j - \bar{\eta})^4}{N\sigma^4} \tag{2.10}$$

Mori and Janssen (2006) derived the probability of occurrence of a rogue wave (defined as $H > 2H_s$) including the kurtosis, and is shown in equation 2.11 considering deep water conditions. $\beta = e^{-8}$ is a constant and corresponds with the exponent in equation 2.7 and 2.8 for $H_0 = 2H_s$. In addition, for a large N the part in brackets in equation 2.8, $V = (1 - Q)^N$, with $Q = \exp(-2\frac{H_0^2}{H_s^2})$ can be estimated as $V \approx \exp(-NQ)$. κ is the kurtosis.

$$P_{rogue} = 1 - \exp(-\beta N(1 + 8(\kappa - 3))) \tag{2.11}$$

For $N = 1000$, $\kappa = 3$ and $\kappa = 3.5$ a probability of occurrence of 28% and 81% is found respectively. This shows that for a wave field with a large kurtosis the probability of occurrence of a rogue wave is several times larger. For this reason, an excess kurtosis in a wave record can be regarded as a rogue wave identifier as it describes the deviation from the linear model and therefore the presence of statistically abnormal waves.

2.2.1 *Forecasting rogue waves*

It must be noted that kurtosis cannot be used directly to forecast the occurrence of rogue waves. This is because the parameters only change when a rogue wave (or statistical deviation from the linear model) is actually present

in the data set (Stansell, 2004; Kharif et al., 2009; Christou and Ewans, 2014; Teutsch et al., 2020). Forecasting rogue waves in time and space is thus still impossible. Using experiments, however, locations or conditions that enhance the probability of occurrence of rogue waves (by measuring excess kurtosis) can be identified.

2.3 Rogue waves in the North Sea

In this section relevant research including rogue waves and the North Sea will be discussed. Figure 2.3 shows several measurement locations of which the data is used in (recent) research. The offshore platforms and oilfields; North Alwyn, Frigg, Draupner, Ekofisk and Gorm of which the data is used in several studies over the past few decades and radar stations and wave buoys of which the data is used in a recent study can be observed. In this section, the question whether rogue waves occur (using the rogue wave criteria) in the North Sea will be answered surprisingly quickly.
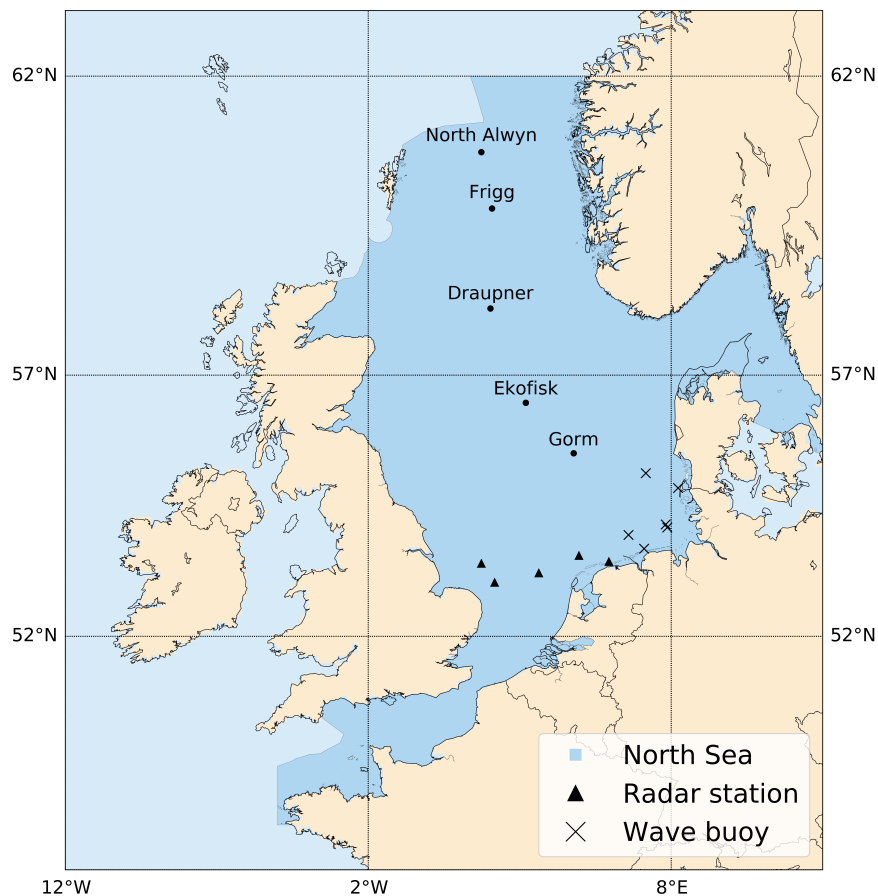

Figure 2.3: Measurement locations in the North Sea used in the discussed rogue wave studies. The offshore oil fields are indicated with their name and a black dot, radar stations with a triangle and wave buoys with a cross.

As was also mentioned in section 1.1, the "Draupner wave" or "New-year wave" can be regarded as the most famous rogue wave throughout history. This is because this wave has led to the interest of many scientists in the occurrence and physics of rogue waves. This famous wave was actually measured in the North Sea by the Statoil platform Draupner E (58°11' N, 2°2' E) (Haver, 2004; Adcock et al., 2011). Consequently, several researchers have studied the Draupner wave records (Haver and Andersen, 2000; Guedes Soares et al., 2003; Adcock et al., 2011; Cavaleri et al., 2017). The wave had a wave height of approximately 26 meters and a crest height of no less than 18.5 meters in a sea with a significant wave height of 12 meters (Haver, 2004), see figure 1.5. The Draupner wave can therefore be characterised as a double rogue wave. Even though the Draupner wave already seems large and rare, it is certainly not the only rogue wave that has been measured in the North Sea.

Another well-known rogue wave is the "Andrea wave". This wave was measured on the Ekofisk oilfield by a

Datawell waverider buoy (56°30' N, 3°12' E) during a storm from 8 to 9 November 2007. The Andrea wave could actually be considered more extreme than the Draupner wave as the abnormality indices for these waves equals 2.3 and 2.24 respectively (Krogstad et al., 2008; Karin Magnusson and Donelan, 2013). At the approximate same location but many years earlier, in 1984, an unrecorded and unnamed wave damaged a control room of one of the Ekofisk platforms. The exceptionally high crest height was estimated to be 20 meters above mean sea level (Skourup et al., 1997).

Besides the two famed waves, several other rogue waves have been identified by researchers on North Sea grounds. The used sea surface elevation data for their analysis has been collected from several offshore platforms, wave buoys and radar stations located all over the North Sea. Stansell (2004), for example, analysed 794 hours of surface elevation measurements from the North Alwyn Platform (60°48' N, 1°44' E) during 14 storms. Out of the 354 thousand individual waves he found 104 rogue waves. The most extreme wave had an AI of 3.19, which is even larger than the AI of the Draupner and Andrea wave. The wave record of this wave can be seen in figure 2.4.
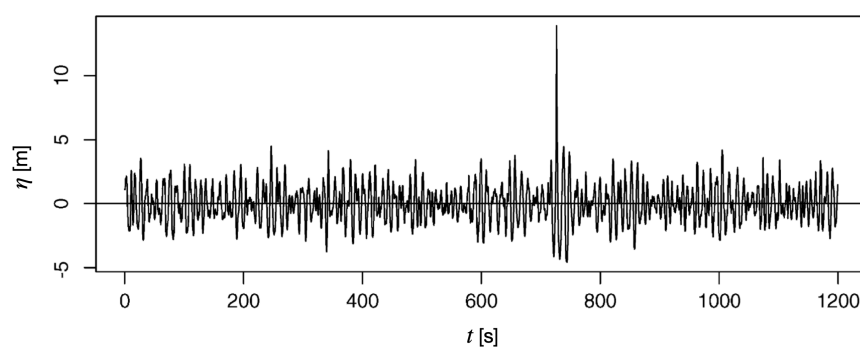

Figure 2.4: Surface level elevation measured at the North Alwyn oil and gas platform (Stansell, 2004)

The surface elevation measurements collected by the Thorm EMI infra-red laser altimeters on the three corners of the North Alwyn oil and gas platform have also been used in other studies (Guedes Soares et al., 2003; Slunyaev et al., 2005; Christou and Ewans, 2014). Guedes Soares et al. (2003) found that 23 out of the 421 20-minute surface elevation time series registered during a storm from 16 to 22 of November 1997 by the North Alwyn fixed steel jacket platform, contained waves that satisfied one of the rogue wave criteria. For 8 of the 421 time series 'double rogue waves' were identified. As in these time series 'only' a little less than 55 thousand individual waves were measured, it was concluded that waves satisfying the rogue wave criteria are, on contrary to their name, not so rare in the North Sea.

Surprisingly, before the Draupner event, in 1984 the "Gorm" rogue wave was measured at the Gorm gas- and oilfield (55°34'N, 4°47'E) (Dysthe et al., 2010). The Draupner wave is therefore actually not the first-ever recorded rogue wave as some sources might claim. The Gorm wave had a *crest* height of 11 meters in a wave field with a significant wave height of 5 meters. Knowing that one of the rogue wave criteria is that the crest height must be larger than 1.25 times the significant wave height, this wave with $\eta_c/H_s = 2.2$ is very extreme. Because the total wave height is not that significant (only 11 meters compared to the 26 meter Draupner wave), this wave did not receive as much fame as some other waves. Besides this extreme wave, many wave records recorded from a bridge connecting two Gorm platforms have been analysed. For example, Skourup et al. (1997) researched twelve years of wave records collected between November 1981 and February 1993.

Another data-set measured in the North Sea originates from wave radar measurements on the Frigg platform (59°53' N, 2°5' E). This set consists of 1.6 million waves and has been investigated by Olagnon and Iseghem (2000). In this research, it was investigated whether the seamans' tales could be verified with in-situ data. It has been found, for example, that a so-called "hole in the sea" preceding a rogue wave event can be reconstructed and thus corresponds with the mariners' observations. In addition, it was researched whether the extreme waves could be classified as "ab-normal". It was concluded for the Frigg data that the extreme waves did not belong to a different (non-Gaussian) statistical distribution. It was noted however that for this data-set (and generally all field data sets), containing a small number of extreme waves, it is difficult to find differences between rogue and "normal" extreme waves.

On contrary to the frequently used 'old' data sets obtained from instruments on offshore platforms or wave buoys near oilfields, a recent study by Teutsch et al. (2020) used a large 'new' data set. A total of five stations with radar measuring equipment between the Netherlands and Great Britain and six wave buoys in the German Bight were used to collect the new data set. Six years of measurements (2011-2016) resulted in a total of 329 million individual waves from a little less than 800 thousand 30-minute samples. Teutsch et al. (2020) concluded that the wave heights roughly followed the (expected, see section 2.1.1) Forristall distribution with some deviations in the upper tail for the radar stations in particular. The wave buoys (except for one), did not detect rogue waves more frequently than expected following the Forristall distribution. This is suggested to be due to the buoys their inability to measure maximum amplitudes (slide away from short crest waves) and possible underestimation of the crest heights (due to overestimation of the mean water level due to their own Lagrangian movement). However, despite the limitations of the wave buoys one location, a buoy near Norderney, did show a larger probability of occurrence of rogue waves than would be expected from the Forristall distribution. Teutsch et al. (2020) suggested that measurement errors due to for example wave breaking and/or tidal currents or "strongly structured bathymetry with strong gradients" could have played a role in this increase. This last suggestion is of importance to this research as this location includes a relatively shallow environment ánd a bathymetry with depth transitions. This will be further discussed in chapter 8. Teutsch et al. (2020) also investigated several sea state parameters such as wave steepness and asymmetry, but no significant differences between records with and without rogue waves were found. In addition, because the deviation in the tail of the wave height distribution is based on a limited number of cases, the study concludes, in accordance with the conclusion drawn by Christou and Ewans (2014) that rogue waves are simply "rare realisations from typical distributions, caused by dispersive focusing".

2.4 Overview research on depth transitions and rogue waves

Over the past few years, several physical mechanisms leading to the occurrence of rogue waves have been derived. According to Dysthe et al. (2008); Kharif and Pelinovsky (2003) there are basically three categories that are based on the focusing of energy; spatial focusing, temporal-spatial focusing and nonlinear focusing. The first category, spatial focusing, includes the effects of waves propagating over a certain bottom topography and wave-current interaction. Temporal-spatial or dispersive focusing is the focusing of waves in a group with steadily decreasing frequency. At some point in time the wave group has decreased to its minimum in size and a maximum crest is expected. The last category, nonlinear focusing, is the effect of the Benjamin-Feir (BF) instability. The result of this instability is the break up of a regular wavetrain into periodic groups. As the periodic groups slowly but continuously focus further, at some moment in time a very large wave occurs.

All physical mechanisms have been studied extensively numerically and experimentally over the past few years (Sergeeva et al., 2011). In this thesis, the physical mechanism of the first category; spatial focusing, and more specifically, interaction with bottom topography is the main theme. Therefore, in this section relevant literature specifically about rogue wave occurrence in the vicinity of depth transitions will be reviewed.

Waves propagating over a sloping bottom have been studied physically and through numerical models. Physical experimental research has shown that a maximum of kurtosis and skewness can be observed for waves propagating from a relatively deep to a shallower regime (Trulsen et al., 2012; Kashima et al., 2014; Ma et al., 2014; Bolles et al., 2019; Zhang et al., 2019; Trulsen et al., 2020; Moore et al., 2020; Li et al., 2021a, 2020b). After the depth transition, it has been observed that the value for the kurtosis decreases to 3 in accordance with Gaussian statistics and the skewness decreases to a new level, not necessarily zero as in the shallower regime the waves are left with a more asymmetric shape (Zhang et al., 2019). In addition to physical experimental research, also (numerical) models have shown an increase in the probability of occurrence of rogue waves in the vicinity of depth transitions (Sergeeva et al., 2011; Janssen and Herbers, 2009; Gramstad et al., 2013; Viotti and Dias, 2014; Kashima et al., 2014; Ducrozet and Gouin, 2017; Majda et al., 2019; Zheng et al., 2020; Li et al., 2021b) Numerical and physical experiments have also been performed for waves travelling from relatively shallow to a deeper regime. In these experiments no increase in kurtosis or skewness has been observed (Trulsen et al., 2012; Sergeeva et al., 2011; Gramstad et al., 2013).

On contrary to the studies mentioned above, a numerical study by Zeng and Trulsen (2012) using a nonlinear Schrödinger model did not find an increase in kurtosis and skewness for waves propagating over a depth transition in finite depth. In this study mild slopes (between 1:33 and 1:22) with the shallower and deeper non dimensional

depths kh = 1.2 to 4.0 and kh = 10 respectively were considered. Similar results have been found by Gramstad et al. (2013). Using Boussinesq models, no maxima of the skewness and kurtosis were observed for gentle slopes (1:150) and a small depth difference. Zheng et al. (2020), using fully nonlinear numerical simulations, also supports this observation and concludes that the largest peaks in statistics can be observed for infinitely steep slopes, also known as a step. This is in accordance with results from Viotti and Dias (2014) (also using fully nonlinear simulations) where enhanced non-Gaussian statistics were observed for stronger depth transitions. Sergeeva et al. (2011) however, concluded that the slope does not affect the statistical parameters. In this numerical study the Korteweg-de Vries equations were solved and the most gentle slope considered was approximately equal to 1:100.

Besides the influence of slope, the effects of other parameters have also been investigated. Sergeeva et al. (2011) found that a higher steepness (larger Ursell number) leads to higher maxima of the kurtosis and skewness. The influence of the spectral width on the probability of occurrence of rogue waves has been researched by Ma et al. (2014). No clear relation between the spectral width (peak enhancement factor of the JONSWAP spectrum) and the probability of rogue waves was found. It was however concluded that the increase of wave groupiness, due to shoaling on a submerged bar, can be related to the appearance of rogue waves. Gramstad et al. (2013) concluded that the maxima of the kurtosis and skewness are not sensitive to bottom topography after the slope. Last, Ducrozet and Gouin (2017) investigated the influence of directional seas. In order to give an accurate estimation of the probability of occurrence of rogue waves, it was stressed that directional effects must be taken into account. It is therefore important to keep this limitation of unidirectional experiments in mind when comparing it with "real" seas.

In addition to the investigation of the influence of several parameters, researchers have also tried to explain the increase of kurtosis (peaks). Two hypotheses for the formation of these peaks have been proposed (Li et al., 2020b). In the first explanation a system of waves is brought out of equilibrium due to propagation over a depth transition. A new equilibrium is rapidly reached via nonlinear processes (third and higher-order in steepness) causing a peak in kurtosis (Viotti and Dias, 2014; Trulsen, 2018). The second hypothesis holds the second-order in steepness terms responsible for the occurrence of the peaks (Gramstad et al., 2013; Zheng et al., 2020; Zhang et al., 2019; Li et al., 2020b, 2021b). The latter will be further elaborated in section 2.5.
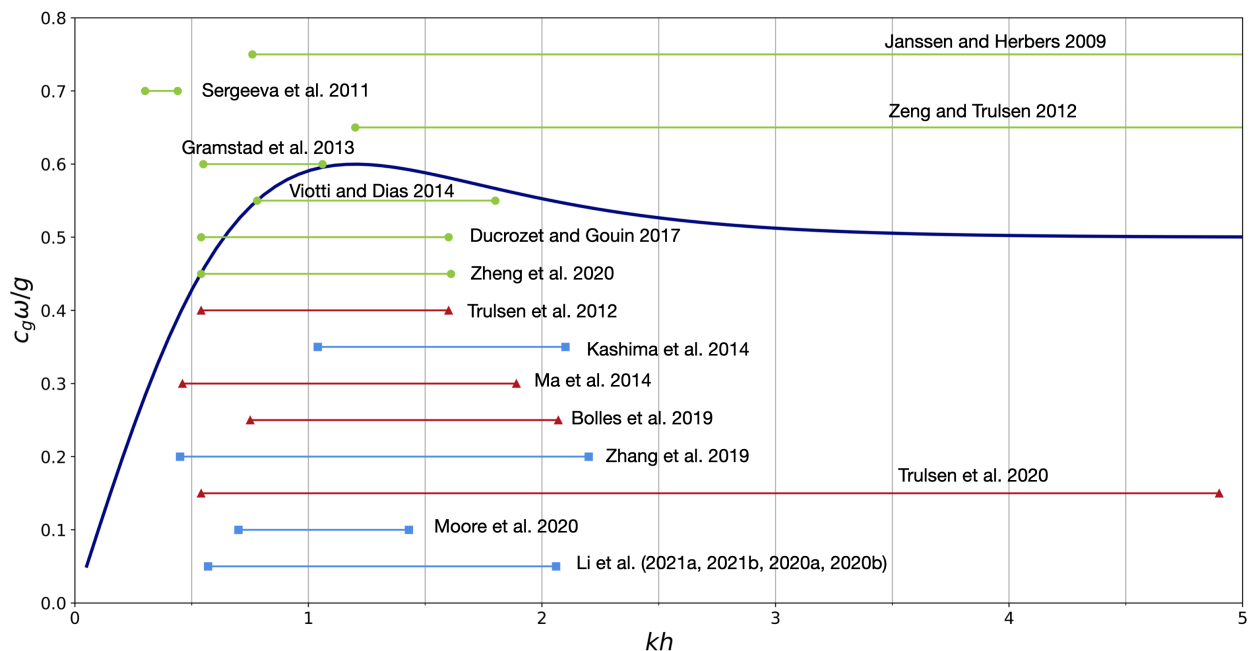

Figure 2.5: *Experimental literature overview with their ranges of dimensionless depths kh. The green line with circles indicate numerical experiments. Red lines with triangles are physical experimental studies. The blue lines with squares are a combination of research using numerical and physical experiments. This figure is an extended and simplified version of the overview given in Trulsen et al. (2020) and Li et al. (2021a).*

Figure 2.5 summarises all research including rogue waves and depth transitions with physical and numerical experiments with respect to the dimensionless depth kh. For each research, the shallowest dimensionless depth is indicated with a marker (circle, triangle, square) on the left side of the line and the deepest dimensionless depth is marked on the right side of the line. It can be observed that Janssen and Herbers (2009) and Zeng and Trulsen (2012) used even deeper dimensionless depths than $kh = 5$. The research performed by Li et al. is summarised in one line and comprises a total of four papers. Li et al. (2021b) provides a theory (specifically about wave packets) and describes numerical experiments. Li et al. (2021a) is an extension of the previous paper and adds the results of physical experiments (wave packets). Li et al. (2020b) is a combination of physical and numerical experiments using physical and numerical irregular wave experiments. Li et al. (2020a) elaborates on the methods used in the previous paper. Using figure 2.5, it can clearly be observed that for a dimensionless depth smaller than 0.5 only one numerical study and no physical experiments have been performed.

2.5 Theoretical framework

In this section, the derivation of a theoretical framework for irregular waves developed by Li et al. (2021b, 2020b,a) will be discussed. This framework explains the mechanism behind the hypotheses that deviation from Gaussian statistics (a peak in kurtosis) is related to second-order terms (in steepness). The theory builds upon previous research by Massel (1983) that investigated the influence of underwater obstacles on incident waves using its self-developed nonlinear theory valid up to second-order. The method was developed in order to assess the efficiency of submerged breakwaters in coastal areas. Massel (1983) concluded that the submerged step induces reflection and generates higher harmonics above the top of the obstacle which are transmitted as free waves in both directions. These free waves have, on contrary to the bound waves, a dispersive nature. The framework discussed in this section builds upon this phenomenon. Figure 2.6 shows the two-dimensional situation considered in this theory. It can be seen that waves propagating from a deeper region, h_d over a step at $x = 0$ to a shallower region, h_s are modelled. It is assumed that $h_d > h_s$ and the dimensionless water depths can vary between relatively deep, $kh \gg 1$, intermediate, $kh \approx 1$ and relatively shallow, $kh \ll 1$.
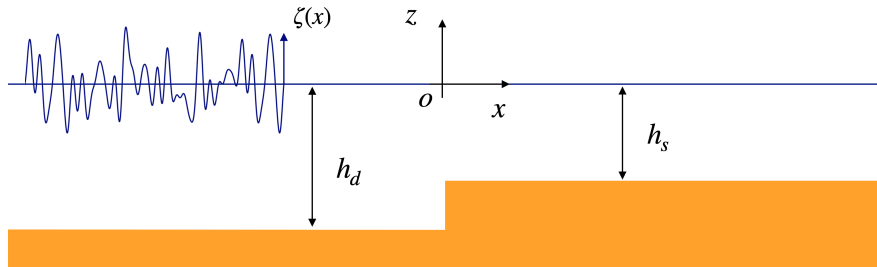

Figure 2.6: (Irregular) waves propagating over a step; bathymetry and coordinate system adopted in the theory

To understand the proposed mechanism causing peaks of kurtosis in the vicinity of depth transitions and in order to understand the limitations of the presented theory, the derivation of the framework will shortly be discussed. Additional relevant equations for the statistical model are presented in appendix A.

Two-dimensional potential-flow theory neglecting effects of viscosity, density differences and surface tension is considered. This theory describes the velocity potential function $\Phi = \Phi(x, z, t)$, of which the spatial derivatives are equal to the velocities of the water particles $u_x = \frac{\partial \Phi}{\partial x}$ and $u_z = \frac{\partial \Phi}{\partial z}$ and thus also considers irrotational flow. The continuity (mass balance) equation can now be rewritten into the Laplace equation using the velocity potential function.

$$\frac{\partial^2 \Phi}{\partial x^2} + \frac{\partial^2 \Phi}{\partial z^2} = 0 \quad \text{for} \quad -h(x) \leq z \leq \zeta(x, t) \tag{2.12}$$

The problem as shown in figure 2.6, is described as a boundary value problem with Laplace, equation 2.12, as the governing equation. The corresponding 6 boundary conditions are the kinematic boundary condition at the free surface (1): the fluid cannot leave the free surface, and at the bottom (2): the fluid cannot go through

the bottom. The bottom and free surface are therefore considered to be impervious. The dynamic boundary condition at the free surface (3): the pressure must be continuous across the body of fluid. Continuity of the potential (4) and the horizontal velocities (5) above the step: continuity of the two are required as otherwise a nonphysical solution would be obtained. Last, a no-flow boundary condition on the step wall (6): the fluid cannot go through the step. The mathematical expression of the boundary conditions are shown in ascending order below. g Is the gravitational acceleration and ζ is the surface level elevation.

$$\frac{D}{Dt}(z - \zeta) = 0 \quad \text{for} \quad z = \zeta(x, t) \tag{2.13}$$

$$\frac{\partial \Phi}{\partial z} = 0 \quad \text{for} \quad z = -h(x) \tag{2.14}$$

$$g\zeta + \frac{\partial \Phi}{\partial t} + \frac{1}{2}(\frac{\partial \Phi}{\partial x} + \frac{\partial \Phi}{\partial z})^2 \quad \text{for} \quad z = \zeta(x, t) \tag{2.15}$$

$$[\Phi]_{x\to 0^-} = [\Phi]_{x\to 0^+} \quad \text{for} \quad -h(x) \leq z \leq \zeta(x, t) \tag{2.16}$$

$$\left[\frac{\partial \Phi}{\partial x}\right]_{x\to 0^-} = \left[\frac{\partial \Phi}{\partial x}\right]_{x\to 0^+} \quad \text{for} \quad -h_s \leq z \leq \zeta(x, t) \tag{2.17}$$

$$\left[\frac{\partial \Phi}{\partial x}\right]_{x\to 0^-} = 0 \quad \text{for} \quad -h_d \leq z \leq -h_s \tag{2.18}$$

To solve the boundary value problem and thus the Laplace equation with its constraints (the boundary conditions) the Stokes expansion is used. This theory approximates nonlinear solutions by adding additional harmonic waves to the 'basic' or 'first' harmonic in terms of the velocity potential. The theory of Stokes is known not to perform well in very shallow water ($H \approx h$ and $N_{Ursell} > 26$, with h the water depth, H the wave height and N_{Ursell} a measure for the steepness divided by the relative depth). Using the theory of Stokes the first harmonic (linear wave) is written with the wave steepness, $\epsilon = k_0 A$, explicitly presented $\eta(x, t) = \epsilon \eta_1(x, t)$. The second-order Stokes wave is obtained by adding a second-order correction in steepness (ϵ^2) to the linear signal. The result can be observed in equation 2.19.

$$\Phi = \epsilon \Phi^{(1)} + \epsilon^2 \Phi^{(2)} + O(\epsilon^3) \quad \text{and} \quad \zeta = \epsilon \zeta^{(1)} + \epsilon^2 \zeta^{(2)} + \mathcal{O}(\epsilon^3) \tag{2.19}$$

Now an additional assumption is made; the narrow-band approximation. In case of an irregular sea (which will be modelled in the experiment, see chapter 3) this means that the surface consists of waves with almost the same frequency which interact with each other and consequently produce well-defined beats, see for example left spectrum and surface elevation of figure 2.2. The surface elevation is therefore considered to be of the form of an amplitude-modulated carrier wave. In other words, the amplitude of the carrier wave (with the average frequencies and wavenumbers of the harmonics) modulates with the envelope of the harmonics. The multiple scales expansion is now introduced to separate the slow (X, T) and the fast (x_0, t_0) scales, with $X = \delta x_0$ and $T = \delta t_0$. δ represents a measure for the bandwidth of the spectrum and the scale separation parameter. Using the combined Stokes and multiple scales expansion the boundary value problem can now be solved and expressions for the velocity potentials and the surface elevation can be found.

Figure 2.7 shows a schematisation of the propagation of an irregular narrow banded wave field propagating over a step. It can be observed that the incoming signal is split into a linear, first-order in steepness component $\zeta^{(1)}$ and second-order, sub- $\zeta^{(20)}$ and super- $\zeta^{(22)}$ harmonic, in steepness components. The subscripts b, f and E denote the bound, free and evanescent wave components respectively. When the wave field travels over the step, a portion of the incoming wave field continues in the positive x-direction and is thus transmitted T, and another portion is reflected and therefore continues in opposite direction R. Noticeable is the formation of free waves which are the counterparts of the bound sub- and super-harmonics due to interaction with the step. These free

waves propagate, on contrary to their bound counterparts, according to the dispersion relation. This means that the free sub-harmonic travels faster than bound sub-harmonic as their length is long with respect to the carrier wave. The opposite is true for the free super-harmonic, as the frequency is twice as high as the linear carrier wave, this wave will propagate less fast compared to its bound counterpart. Also remarkable is the existence of evanescent waves, ζ_E, which are byproduct of solving the boundary conditions at the step and exist due to a mismatch in velocities over depth due to the depth transition. The evanescent waves are considered to be of minor importance as their amplitudes will decay exponentially with their distance from the step. Therefore the evanescent modes are neglected in the calculations. For all surface level elevation components shown in figure 2.7 expressions have been found using the combined Stokes and multiple scales expansion briefly discussed in the previous paragraph. Appendix A provides the expressions for all components.

The mechanism that explains the higher probability of occurrence of rogue waves and thus peaks in kurtosis, is therefore the co-existence of the linear and bound sub- and super-harmonic waves and the second-order free waves induced by the presence of a step/steep depth transition. As the propagation speeds of the second-order free waves differ from the linear and bound second-order waves, peaks are localised (thus causing an increase in kurtosis) at some distance away from the depth transition while the wave field adjusts to its new equilibrium.
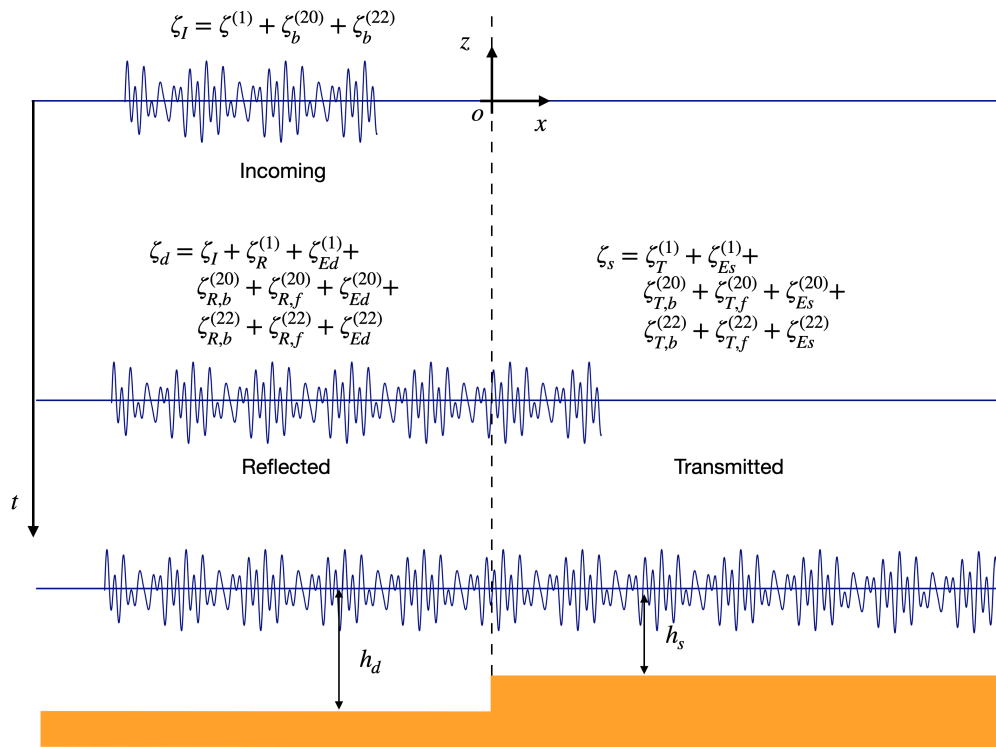

Figure 2.7: Surface level elevation components of an irregular narrow banded sea before and after propagation over the step. From top to bottom, each horizontal line represents the surface elevation with increasing time. $\zeta^{(1)}$, $\zeta^{(20)}$ and $\zeta^{(22)}$ are the linear and second-order sub- and super-harmonic components and the subscripts b, f, E, T and R denote the bound, free, evanescent, transmitted and reflected wave components respectively. The total wave field at the shallow and deep water side are denoted as ζ_s and ζ_d.

Fully non-linear numerical simulations and physical experiments ($0.57 < kh < 1.6$) have been performed to validate the presented theoretical framework (Li et al., 2020b,a). Irregular waves described by a JONSWAP-spectrum, which resembles realistic seas, have been generated. The peak frequency, water depths and significant wave height have been varied. It is concluded that the model predicts the development, location and magnitude of the peaks of the kurtosis and skewness accurately in all cases. Some small deviations between the model, physical experiments and numerics are assumed to be due to the violation of the narrow-bandwidth assumption (JONSWAP has a wide high-frequency tail) and presence of third-order effects. These third-order effects are found to be most pronounced for the deepest case ($1.0 < kh < 1.6$).

Experimental set-up

In this chapter first an introduction to the model facility is given. Hereafter the scale of the experiments is derived using the potential rogue wave event shown in figure 1.6. Following, the flume layout will be determined and the method of data collection is explained. Last, the experimental program is elaborated.

3.1 Model facility

The physical experiment is performed in the wave-flume of the Hydraulic Engineering laboratory facility at the Delft University of Technology. The flume has a total length of 39 meters, a width of 0.79 meters and a height of 1 meter. The total maximum stroke of the wave generator is 2 meters (1 meter amplitude). The wave board is an electrical piston-type generator, which means that the face of the board remains vertical during actuation and moves horizontally (forward and backward). A front view of the wave board is shown in figure 3.3d. The control signals for the wave board are calculated using the software package AUKE/PC which is developed by WL|Delft Hydraulics, nowadays known as Deltares.

The software package AUKE/PC is known to have the ability to include second-order steering in the control signal. As the correct generation of bound waves is of importance for these experiments the second-order control signal has been assessed. This is elaborated in chapter 4.

3.2 Scaling met-ocean conditions

As presented in section 1.3, highly idealised experiments with a variation in dimensionless water depths will be performed to investigate the influence of depth transitions on the probability of occurrence of rogue waves. The peak period of the Gaussian wave spectra and bathymetry in the flume are scaled based on the met-ocean conditions during the potential rogue wave event in the Dutch North Sea shown in figure 1.6. The average period of the waves some minutes prior to the event is estimated at 25 seconds and will therefore be used as the prototype wave period. This wave period is unusually long considering regular North Sea conditions. It can be observed that after the event the wave period is again much shorter ($T \approx 10$ seconds) and in accordance with expected North Sea conditions. It must therefore be noted again that it is still unknown whether the measured surface elevation is 'true' or that it is a data processing artefact or measurement error.

A cross-section of the bathymetry at the location of buoy HKWA 52°34'N 3°43'E is shown in figure 3.1. The cross-section is drawn West to East which is roughly in the same direction of the incoming waves during the rogue wave event. The waves in figure 3.1 thus propagate from left to right. The buoy is located at $x \approx 3.2$ km. It can be seen that the morphological feature or so-called sand ridge has a total length of 2.5 kilometers and height of approximately 8 meters. The depth on the left and right of the sand ridge is approximately -30 meters. With the estimated wave period of 25 seconds, the dimensionless water depth, kh_d, therefore equals 0.45.

The scaling of the met-ocean conditions to the wave flume also depends on the limits of the wave generator. The maximum peak period of the wave generator is said to equal 3 seconds. Because the prototype wave period (T_p) of 25 seconds leads to a small scaling factor (which leads to small flume depths) a high fixed model peak period (T_m) of 2.8 seconds, just within the limits, is chosen. According to equation 3.1, the scaling factor n_f is therefore set at 1/80 (Frostick et al., 2011). Using the deep and shallow water depths of $h = -30$ and $h = -23$ m of the sand ridge respectively, corresponding flume water depths of 0.375 and 0.275 m are derived. This leads to a depth transition, step height, of 0.1 meter. Using figure 3.1 the slope of the sand ridge is estimated at approximately 1:200. With a depth transition of 0.1 meter a scaled slope of 20 meters (0.1*200) would be

required. Since it is physically impossible to fit this slope length in combination with enough space behind the end of the slope to obtain relevant measurements, a smaller slope of 1:20, thus 2 meters length, is determined.
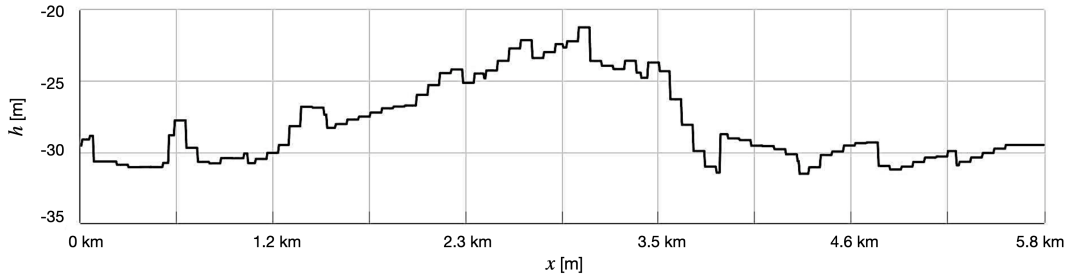

Figure 3.1: Cross-section of the bathymetry at the location of buoy HKWA 52°34'N 3°43'E (x ≈3.2 km) which measured a possible rogue wave event at the 11th of February 2020. h Is the water depth and x the distance from the start of the cross-section (EMODnet, 2020).

$$n_F = \left(\frac{T_m}{T_p}\right)^2 = 0.0125 \tag{3.1}$$

$$h_{m,d} = n_f h_{p,d} = 0.375 \ m \tag{3.2}$$

$$h_{m,s} = n_f h_{p,s} = 0.275 \ m \tag{3.3}$$

The significant wave height will not be scaled based on the possible rogue wave event as this will be determined by the limits of the theoretical framework. The significant wave height calculation is shown in section 3.5. It can be seen in the overall test overview that the second limitation of the wave generator, namely the maximum significant wave height relative to the depth ($3.5 \ H_s < h$) is met and that the water depths do not exceed the size of the flume.

3.3 Flume layout

An overview of the flume layout is shown in figure 3.2. Remarkable in this figure is the total height difference between the wave generator and start of the step. It can be seen in the figure that the total height of the step equals 10 centimeters, which is also determined in section 3.2. However, because the bottom of the flume is not precisely levelled, there is 1.5 centimeter difference in bottom height, and thus water depth. The total height difference is therefore 11.5 centimeters and is indicated by the white arrow in figure 3.2.
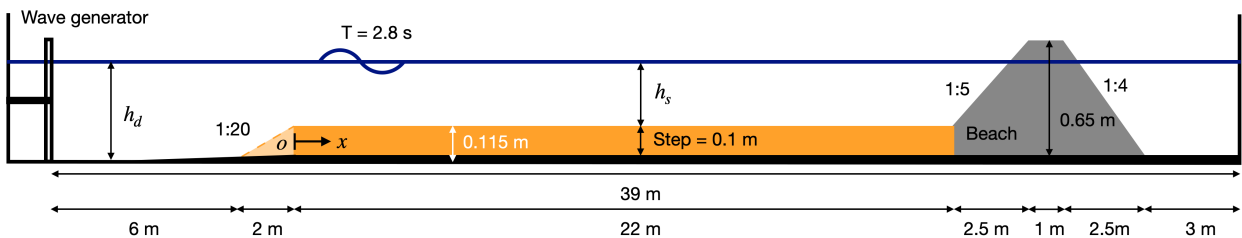

Figure 3.2: layout and dimensions of the flume. The bathymetry is shown in orange and the beach (wave absorber) in grey.

An impression of the flume layout, submerged in 50 centimeters of water, is shown in figure 3.3a. In this picture the gravel wave absorption beach can be identified (further elaborated in section 3.3.1) and the wave gauges and velocity meters (elaborated in section 3.4) can be observed. In addition, a white layer on top of the water surface

can be identified. This layer is "seeding" material that ensures that the laser scanner (elaborated in section 3.4) can take measurements of the water surface. Figures 3.3b and 3.3c show the step and the slope respectively. Note the use of waterproof aluminum tape where the construction meets the flume walls and bottom. This tape is applied in order to ensure that the step and slope are watertight. This prevents unwanted (additional) wall effects and energy losses.

Figure 3.3: *Impression of the flume set-up at the Delft University of Technology Hydraulic Engineering laboratory. (a) Is an overview of the flume. The picture is taken at the end of the flume. (b) Shows the step. (c) Shows the slope. (d) Is a front view of the paddle board.*

3.3.1 *Wave reflection reduction*

Contrary to measuring at sea, the flume is not of infinite length, incoming waves (waves that one wants to measure) will reflect at the end of the flume and propagate in opposite direction towards the paddle board. These reflected waves contaminate the incoming (that one wants to measure) wave field and must therefore be reduced, or ideally, completely eliminated.

To reduce the contamination of the incoming wave field during the experiments a wave absorption system is installed down-wave of the step. This absorption system can be seen in figure 3.2 where it is labelled the "gravel beach". The location of the gravel beach is positioned approximately 3 meters left of the flume end. This position is chosen as the particle velocities are zero at a fully reflective boundary ('vertical wall' at the end of the flume). To obtain maximum wave absorption and therefore maximum drag forces, it is hypothesised that the particle velocity must be at its maximum at the location of the gravel beach. This means that the longest

waves are governing for the location of the wave absorber knowing that maximum particle velocity occur at a quarter (and three-quarter) wavelength. Therefore, for optimal wave reduction one wants the gravel beach to be located at least somewhat before and after (one-fifth to one-third wavelength) the location of maximum particle velocity. It follows therefore that for waves longer than 3 times the width of the gravel beach, optimal drag forces are not achieved and thus the center of the wave absorber should be moved one-quarter wavelength away from the flume end.

The longest waves expected in these experiments are the bound and free sub-harmonic waves which have an expected length of approximately 20 to 25 meters. The effective width (with stones covering more than 50 percent of the depth) is on average 3 meters. This means that for optimal wave reduction, as explained in the previous paragraph, the gravel beach must be moved one quarter wavelength, $25/4 \approx 6$ meters, away from the end of the flume.

Another important aspect that determines the effectiveness of the gravel beach is the slope angle relative to the wave period and stone size. One can imagine that using a relatively steep angle with small stones leads to many reflections as it approaches a wall (fully reflective boundary). Using a relatively mild slope with small stones (sand) one approaches a fully dissipative beach. As the former is not physically possible in the flume due to its limited length in combination with the long bound and free waves, an optimal can be sought between stone size (pores), slope and total dimension of the wave absorber. As a mild slope is not possible, quite large stones with large pores are used which are expected to produce significant drag forces. For this experiment two types of stones, leftover from other experiments, with the approximate same size, 4.6 and 5.5 cm diameter, were used to build the gravel beach. The stone sizes are calculated by taking a representative sample of six stones per type and taking the cube root of the average difference in a measuring cup filled with water with and without the stones.

Figure 3.4: Front view wave absorber

Figure 3.5: Back view wave absorber

The amount of wave absorption by the gravel beach is estimated to be approximately 70% for waves with a frequency between 0.2 and 0.6 Hz. This is further elaborated in section 5.2. Besides the reflection reduction by the gravel beach, the reflections are also absorbed at the paddle by the 'active reflection compensation'. As the paddle is also a vertical wall, undamped reflected waves could again reflect at the paddle which is undesired. Using active reflection compensation the paddle detects unwanted surface elevations or depressions and absorbs this energy with additional backward or forward movements respectively.

3.4 Data collection

The data is collected using three different instruments; wave gauges and a laser to measure the surface elevation and electromagnetic velocity meters to measure the velocities. Instrument properties and laser set-up will shortly be discussed in the following subsections. Figure 3.6 shows the set-up of the wave gauges and velocity meters. It can be observed that for half of the tests six velocity meters (blue and red) were used and for the other experiments two (blue). This was due to limited availability of the instruments. It must be noted that only a small portion of the laser scanner data will be processed and analysed in this thesis which will be used order to asses its potential for further research. This data is therefore not included in the results due to time constraints.
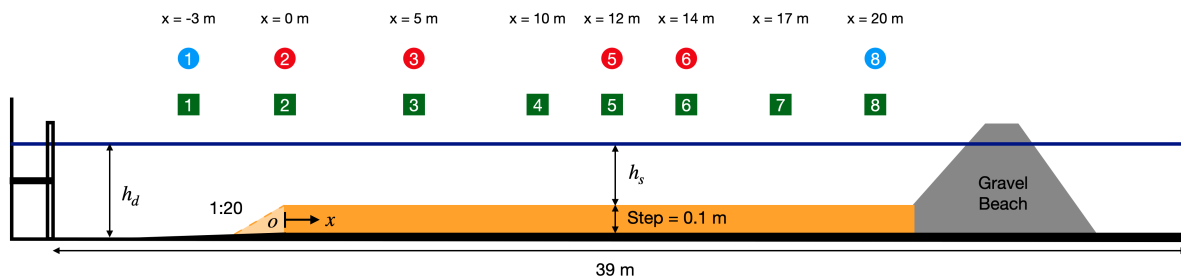

Figure 3.6: Location of wave gauges (green squares) and EMFs (blue and red circles). The blue EMFs were used during all tests. The four additional red EMFs were used for half of the tests.

Wave gauges

The used wave gauges have been developed by Deltares and consist of two parallel stainless steel rods and a platinum reference electrode at the bottom of the rods. The surface elevation in Volt can be read from these instruments using the principle that the electric conduction between the rods are proportional to their immersion. The wave gauges can measure up to 15 Hz and have an accuracy of 0.5% of the measuring range (Deltares, 2021b). This means that for wave heights up to 10 centimeter, an error of only 0.05 centimeter is expected.

During the experiments in the laboratory the wave gauges were calibrated in the morning before testing and in the afternoon after testing using a two-step method. This method includes writing down the sensor output voltages twice, at depth h and at depth h+0.1 meter, for all gauges. The calibration constants [m/V] can thereafter be calculated by dividing the depth difference, 0.1 m, by the difference in output voltage.

Electromagnetic velocity meter

The electromagnetic velocity meters (EMFs) are just as the wave gauges developed at Deltares. The instrument consists of one stainless steel rod with a small 'disk' at the bottom. The velocities are measured using the principle that conductive liquid (water in the flume) affects magnetic fields (induced by an electrical current in the probe). The result is an output voltage that is proportional to the velocities of the liquid in which the probe is located. The EMFs can measure up to 7 Hz. The accuracy of the EMFs is ±0.01 m/s or 1% of the measured value (Deltares, 2021a). The accuracy of the EMFs is therefore less than the accuracy of the wave gauges but is still considered sufficient for this application.

The EMFs are calibrated using an Acoustic Doppler Velocimeter (ADV) in a small flume. The ADV directly measures the particle velocity (thus without the need to find a calibration constant to obtain velocity from a difference in Volt) accurately. The calibration is performed as follows. First, the EMFs are spaced 1 meters apart in a flume. Second, the flume is filled with water and once the water is completely still, the zero value of

each EMF is measured (±1 minute). Third, a constant flow is created in the flume and once the flow and water level is constant (after approximately 20 minutes) the probes of the EMFs are all set at a depth of 7 centimeters below the surface. This value is now also measured (± 2 minutes). Fourth, all EMFs and their mounting material are removed. Now the ADV will be used to measure the velocity at the location of each EMF (also ± 2 minutes per location). The probe of the ADV is put 2 centimeters below the water surface as the ADV measures the particle velocity 5 centimeters underneath the probe (in order to prevent influence of the probe on the flow). This means that the EMFs and ADV measure the velocity at the same depth. This is important, because there might be a (small) difference in flow velocity over depth. Another important remark is that the ADV should be turned off during data acquisition by the EMFs as this disturbs the EMF measurements. Subsequently, the calibration constant can be calculated by dividing the difference in Volt by the velocity measured by the ADV $[m/s/V]$.

Laser

In addition to the wave gauges and EMFs also a 2D light imaging detection and ranging (LiDAR) sensor, more specifically, the SICK LMS511-20100 PRO laser scanner, is used. Using laser pulses (infrared light) this device measures the distance between itself and its surroundings. A possible Hydraulic engineering application of the scanner therefore includes for example detection of the number of cars on a road. Every time the distance between the laser scanner and the road is at least 1 meter shorter, one can count one car. Recently, laser scanners have also been applied in the field of hydraulic engineering to, for example, detect run-up levels on a dike slope (Cete, 2019). Besides this application, the laser scanner has also been used to measure the surface elevation in a laboratory flume. To further investigate the potential of this application, the laser scanner is used in addition to the wave gauges to measure the surface elevation.

The total horizontal aperture angle of the scanner is 190°, which means that when one mounts the scanner to the laboratory ceiling, a slice of the whole experimental facility is measured including part of the ceiling. The measurement accuracy of the high resolution laser scanner is estimated to equal approximately 12 millimeters. This accuracy, considering the wave heights in these experiments, is therefore more than twice as small as the wave gauges. To align the sensor, which requires high precision, an alignment bar is used that lights up when infrared light of the laser is detected. The set-up of the laser is shown in figure 3.7. It can be seen that the sensor is located at a maximum of 6.34 meters above the water surface and that it has a slant angle of $\phi=10°$ relative to the ceiling. The laser is located at $x = 7.66$ m, with $x = 0$ the location of the step. The angular resolution, α was set at 0.667° for the first three tests and at 0.1667° for all other tests in order to obtain more points along the flume. The scan frequency for the first three test was set at 50 Hz and for all other tests at 25 Hz.
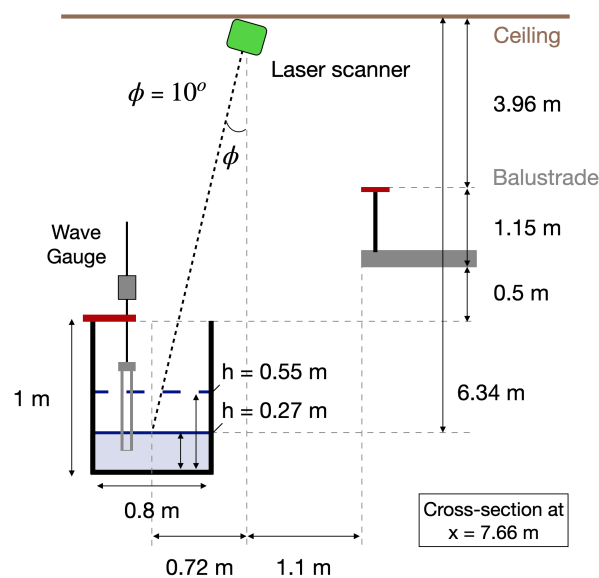

Figure 3.7: Set-up of the SICK LMS511-20100 PRO laser scanner, shown in green, at the TU Delft Hydraulic Engineering laboratory facility at x = 7.66 m, with x = 0 the location of the step.

Because the fresh water in the flume is clear, three liters of dry seeding (mixed over a length of ±20 meters) is added to the water to ensure that the laser pulses reflect at the surface. The seeding used during the experiments were hollow glass spheres of $d_{50} = 19$ μm. This SPHERICEL $^®$ 60P18 has a density of 600 kg/m^3 and is therefore lighter than water. This means that after the seeding is mixed, it slowly starts to move towards the surface. During experiments with relatively large waves (test 1 for example, see table 3.1) the seeding remained mixed. However, during tests with low waves (tests 3 till 8) the seeding has almost completely risen upwards and acts as a floating blanket on top of the water surface. The seeding (white layer on top of the water surface) can be observed in figure 3.3a. During the experiments it was noticed that the amount of seeding, on average 83 NTU (measure for the turbidity and thus concentration), seemed to decrease based on visual observations and decreasing values of the Received Signal Strength Indicator (RSSI). It is important that the RSSI remains at a high value as lower values lead to less accurate or even no measurements of the water surface. After analysing the seeding over time and space, see appendix B, it is concluded that the RSSI values decreased over time due to clumping of the seeding material. To obtain good measurements and thus a high RSSI, one must 'break' the clumps every morning and maybe even between tests using, for example, a scoop-net. This ensures that the seeding is suspended evenly over the water column and the laser can take measurements at all locations along the flume.

3.5 Experimental program

All experiments are irregular wave tests with a peak period of 2.8 seconds, as determined in the section 3.2, and have a duration of ±2.5 hours and thus comprising of approximately 3200 waves. The input for the wave paddle software is a Gaussian, and thus idealised, spectrum and is shown in equation 3.4 and 3.5. c_g is the group velocity, k_{0d} the wavenumber in the deep water region, δ the bandwidth of the spectrum and thus the measure of groupiness, H_s the significant wave height and f_p the peak frequency. The input spectrum is therefore dependent on the deep water depth h_d (to calculate the group velocity), the bandwidth δ and H_s.

$$\sigma_{Gauss} = \sqrt{2} c_g \frac{k_{0d}\delta}{2\pi} \tag{3.4}$$

$$S_{Gauss}(f) = \frac{H_s{}^2}{4} \frac{1}{\sigma_{Gauss}\sqrt{2\pi}} e^{-\frac{(f-f_p)^2}{2\sigma_{Gauss}^2}} \tag{3.5}$$

Table 3.1 presents an overview of the tests that have been performed. It can be seen that the 'basis' tests in the table are numbered 1 until 8 with descending deep (and shallow, $h_s = h_d$ - 0.115 m) water depths. All tests have been performed with a step and all tests colored in dark blue have also been performed with a 1:20 slope. This means that the tests with a spectral bandwidth increase ($\delta \uparrow$) and steepness increase ($kA \uparrow$) have not been performed with a slope. It follows that a total of 27 tests are performed.

The bandwidth for each test is determined using predictions of the theoretical framework. Elaboration of the framework is shown in section 2.5. The bandwidth, according to theory, has influence on the location of the peaks. The larger the bandwidth the smaller the distance between the depth transition and the peak location. Also, it is expected that the smaller the water depth the larger the distance between the peak location and depth transition. Therefore, for tests with smaller water depths it is thus chosen to increase the bandwidth to keep the peak location (measureable) in the flume. To assess if the increase in bandwidth has additional effects on the results, tests 1, 2 and 4 are also performed with an increased spectral bandwidth.

The significant wave height is set at the upper limit of Stokes second-order theory, which is equal to $N_{Ursell} < 26$ (Holthuijsen, 2007). The upper limit is chosen to prevent possible wave generation issues arising from very small amplitude waves. The smallest significant wave height using the upper limit is only 0.83 centimeters. Using a smaller Ursell number results in even smaller waves. Equation 3.6 presents the equation used for the calculation of the significant wave heights. It can be seen that the shallow water depth h_s and wavelength L_s (derived from the dispersion relationship) are used. Using the deep water parameters would result in exceedance of the Stokes second-order limit in the shallow water region.

$$H_s = \frac{26 h_s^3}{L_s^2} \tag{3.6}$$

No.	h_d [cm]	H_s [cm]	δ [-]	$k_{0d} h_d$ [-]	$k_{0s} h_s$ [-]	ϵ_d [-]	$s_{0,p}$ [-]
1	55	6.9	0.15	0.56	0.49	0.04	0.0056
2	50	5.36	0.15	0.53	0.46	0.03	0.0044
3	45	4.02	0.15	0.50	0.43	0.02	0.0033
4	40	2.89	0.15	0.47	0.39	0.02	0.0024
5	37.5	2.42	0.25	0.45	0.37	0.01	0.0020
6	35	1.94	0.25	0.44	0.35	0.01	0.0016
7	30	1.19	0.35	0.40	0.31	0.01	0.0010
8	27	0.83	0.36	0.38	0.29	0.01	0.0007
1a $\delta \uparrow$	55	6.9	0.25	0.56	0.49	0.04	0.0056
2a $\delta \uparrow$	50	5.36	0.25	0.53	0.46	0.03	0.0044
4a $\delta \uparrow$	40	2.89	0.25	0.47	0.39	0.02	0.0024
1b $kA \uparrow$	55	11.3	0.15	0.56	0.49	0.06	0.0092
3a $kA \uparrow$	45	7.4	0.15	0.50	0.43	0.04	0.0060
6a $kA \uparrow$	35	4.4	0.25	0.44	0.35	0.03	0.0036
3b $kA \downarrow$	45	2.01	0.15	0.50	0.43	0.01	0.0016
6b $kA \downarrow$	35	0.97	0.25	0.44	0.35	0.01	0.0008

Table 3.1: Experimental program with step (all tests) and with 1:20 slope (all dark colored tests looking at the first column). The peak wave period T_p equals 2.8 seconds for all tests. The shallow water depth $h_s = h_d$ - 0.115 meter. The wave steepness is shown in terms of $\epsilon_d = k_{0d} H_s / 2$ and $s_{0,p} = H_s / L_{0,p}$ with $L_{0,p}$ the deep water wave length.

<div align="right">

4

</div>

Second-order wave generation

In this chapter first the relevance of second-order wave generation for this thesis and other research is given. Following an introduction to second-order generation is presented. Hereafter the second-order generation software at the TU Delft laboratory is assessed. Next a solution to the current insufficient sub-harmonic correction is provided. This section is concluded with some recommendations.

4.1 Relevance

In this thesis a theory, explained in more detail in section 2.5, is tested that explains the mechanism behind the higher probability of occurrence of rogue waves in the vicinity of a depth transition. The mechanism consists of the co-existence between the linear and bound sub- and super-harmonic waves and second-order free waves that are induced by the presence of the depth transition. As the bound waves play a significant role, it must be ensured that the second-order wave generation performs well. This prevents contamination of the wave field and distortion of the bound waves.

Besides the research performed in this thesis, second-order wave generation can also be of importance for other experimental research. For example, it has been found by Orszaghova et al. (2014) that generating focused wave groups using first-order wave generation (thus without the second-order correction) results in erroneously enhanced run-up levels and overtopping volumes. Subsequently, tested breakwater or dike designs might become too conservative. Why this is the case, is explained in the next section.

4.2 Introduction to second-order wave generation

To understand the need for a second-order correction, at first first-order wave generation is introduced in a simplified manner. To generate waves in a laboratory flume a wave board is used. The wave board used in the laboratory facility in this research is of piston-type, that is a vertical 'wall' moving uniformly back and forward. The horizontal movement of this wave board is translated into vertical movement of the water surface. Following, as the wave board moves uniformly over depth, disturbances, also known as evanescent modes, occur as the particle velocity is not uniform over depth (Orszaghova et al., 2014). One can imagine that velocities directly under a wave are much higher than at for example 10 meters depth. These evanescent modes however decay exponentially and are not the motivation for applying a second-order correction.

Using a first-order wavemaker signal the generation of (weakly) non-linear waves results in 'spurious' or also called 'error' or 'parasitic' waves (van Leeuwen and Klopman, 1996; Schäffer, 1996). The (weakly) non-linear signal consists of linear and higher-order components. Generating these waves with a first-order wavemaker signal results in the linear wave field, correct bound non-linear components (sub- and super-harmonics) and their paired free spurious waves (sub- and super-harmonics). These unintended spurious free waves travel at their own speed and will therefore contaminate the wave field in front of the group. To eliminate these unwanted waves a second-order correction must be applied (van Leeuwen and Klopman, 1996; Schäffer, 1996). As at the paddle the free spurious waves cancel the bound components (Orszaghova et al., 2014), the second-order correction counteracts the spurious waves in advance and ensures that only the desired bound components are left.

Bound sub-harmonic waves resulting from a wave group are visually known as a 'set-down' and are thus equal to a depression in the water surface. The spurious free counterparts exist as a 'set-up' and thus equal an elevation of the water surface. This explains the enhanced run-up levels and overtopping volumes as spurious waves cause additional increase of the water surface and consequently higher wave crests.

4.3   Assessment wave generation Hydraulic Engineering laboratory at TU Delft

In this thesis experiments are performed in the wave flume located at the Hydraulic Engineering laboratory of the Technical University Delft. As mentioned in section 4.1, proper generation of the bound components is required and therefore the wave generation at this facility is assessed.

The control signals of the wave board are calculated using the software package AUKE/PC which is developed by WL|Delft Hydraulics, nowadays known as Deltares. The wave board is of piston-type, has a maximum stroke of 2 meters, thus 1 meter in amplitude, and has width and height of approximately 0.8 m and 1 meter respectively. A front view of the paddle board is shown in figure 3.3d.

4.3.1 *Experimental set-up*

Since the (correct) bound and spurious waves can visually be identified, the wave generation at the laboratory is assessed by measuring a wave group travelling through the flume. The wave group is generated using a paddle which is controlled by a steering signal. This steering signal is calculated by AUKE/PC using a wave group time series (see Appendix F) and has the options to include first- and second-order steering and active reflection compensation (ARC). As explained in 4.2, spurious free sub-harmonic waves can be observed as a set-up on the water surface. Correct generation of the bound components can be observed as a set-down travelling with the speed of the group. It is thus expected that when one wave group is generated with first-order generation a set-up propagating at its own speed must be visible and with second-order generation no set-up should be visible. Following, spurious super-harmonics should also be visible with first-order generation and should be cancelled out with second-order generation.

To measure the wave group propagating through the flume, eight wave gauges are spaced at an equal distance along the flume. The flume is further completely empty and thus no significant wave damping takes place. At the end of the flume full reflection of the generated wave group is expected. Figure 4.1 gives an impression of the set-up.

Figure 4.1: Impression of the set-up for the assessment of the second-order generation at TU Delft

4.3.2 *Wave group results measured in flume*

A total of three cases with decreasing dimensionless water depth are tested. In this section relevant results of 2 cases (case 1 and case 3) are shown. An additional case and additional figures can be found in appendix F. The data processing techniques that have been used are presented in chapter 5 and will not be repeated here. The wave gauges have been calibrated at the start of each experiment day.

Table 4.1 shows an overview of the wave group parameters used in each case. It can be seen that these three cases represent wave groups in transitional water. Case 1 will be shown and discussed, because for this case the difference between the group and shallow water speed is significant and thus visually good interpretable. Case 3 is also shown as this case represents the dimensionless water depths that are used in the rogue wave experiments.

Case	kh [-]	T_{peak} [s]	kA [-]
1	1.44	1.25	0.28
2	0.91	1.75	0.1
3	0.53	2.8	0.044

Table 4.1: Parameter overview per case for the second-order generation assessment

The set of results presented below do *not* include ARC. The super- and sub-harmonic waves are filtered from the total surface elevation and are increased with a factor 5 and 7 respectively with respect to the total surface elevation for visualisation. The y-axis of the figures represent the distance away from the wave paddle. The last wave gauge is thus the top line with 'wiggles'. At the end of the flume, where total reflection takes place, a horizontal black line is drawn. It can clearly be seen that the waves reflect and start travelling back to the wave paddle (bottom of the figure). The propagation speed of the wave groups is shown with a dashed blue line. The speed of the (spurious) free sub-harmonics is indicated as the shallow water speed (the sub-harmonic waves are of such long length that the theory of shallow water depth holds) and is shown with a brown line. The speed of the (spurious) free super-harmonics is indicated as the super-harmonic speed which is calculated using twice the peak frequency. This is also shown with a brown line.

Results case 1
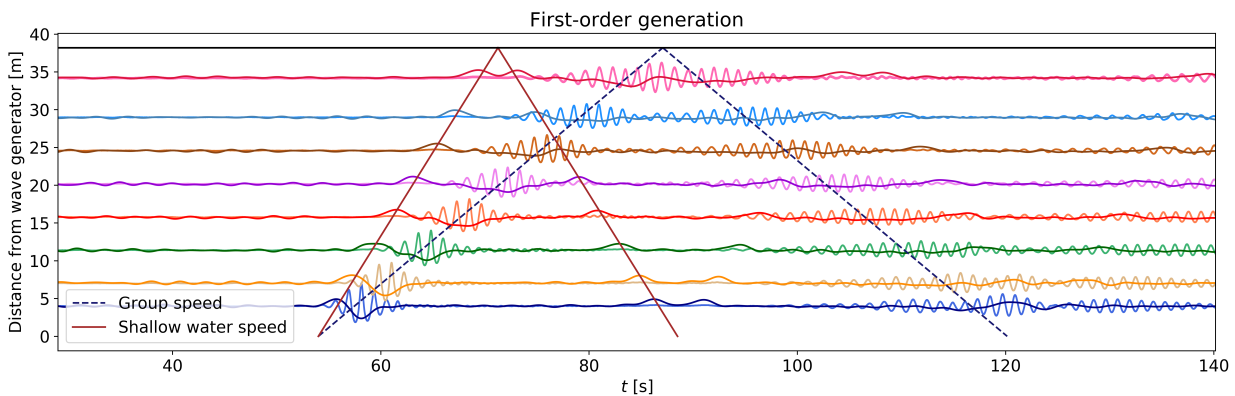
Figure 4.2: Case 1: First-order wave generation. The total surface elevation (lighter lines) and sub-harmonic waves (darker lines) propagating through the flume are shown.
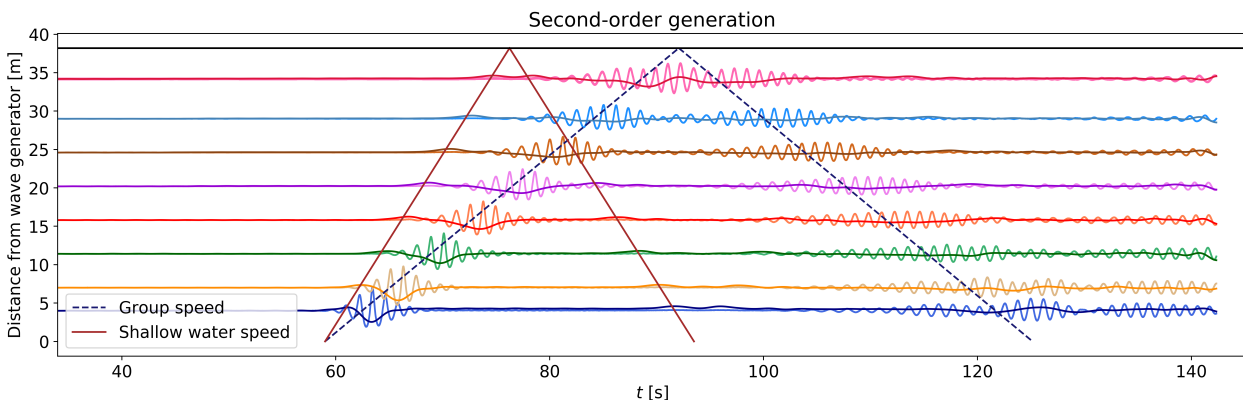
Figure 4.3: Case 1: Second-order wave generation. The total surface elevation (lighter lines) and sub-harmonic waves (darker lines) propagating through the flume are shown.

Figure 4.2 and 4.3 clearly show a difference between the first- and second-order generation regarding the sub-harmonic components. As expected, the spurious sub-harmonic set-up is cancelled out (almost) completely. Furthermore the spurious sub-harmonic indeed travels with the shallow water speed and the bound wave propagates with the speed of the group.
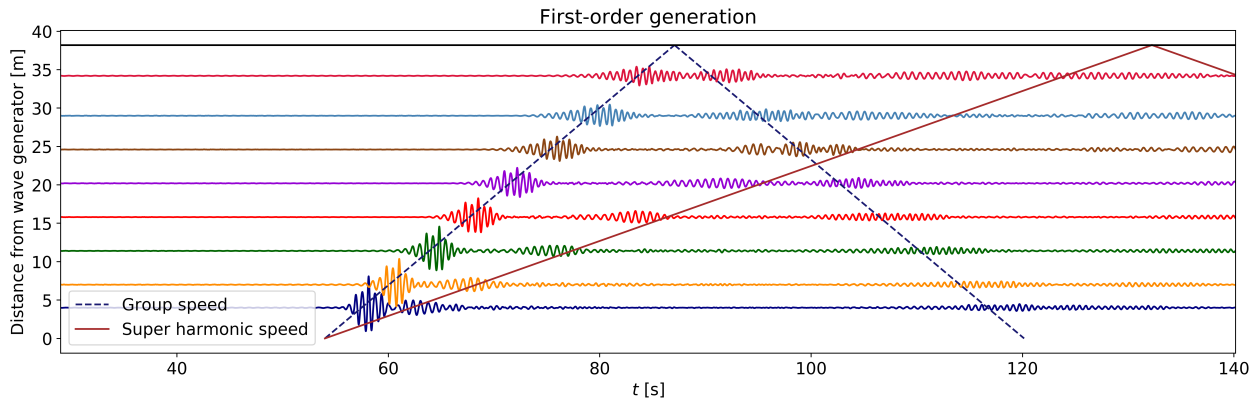

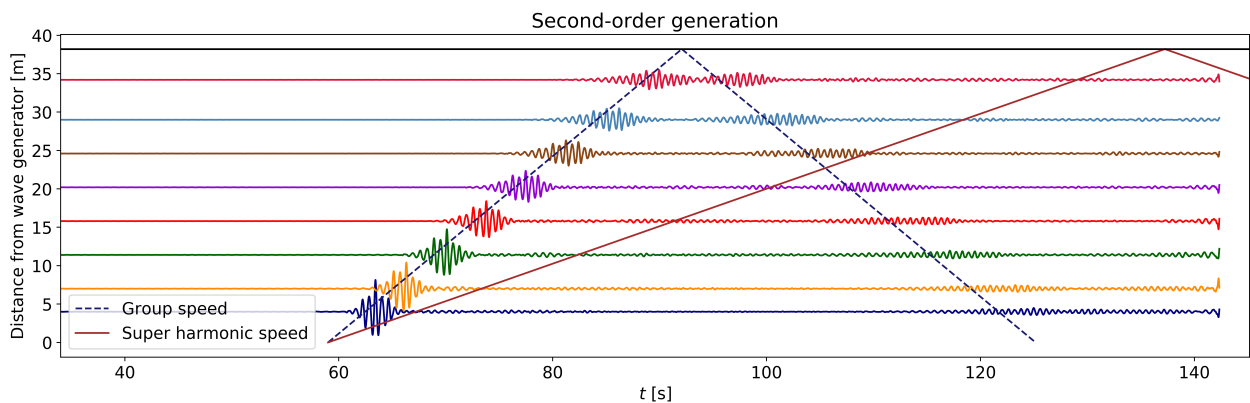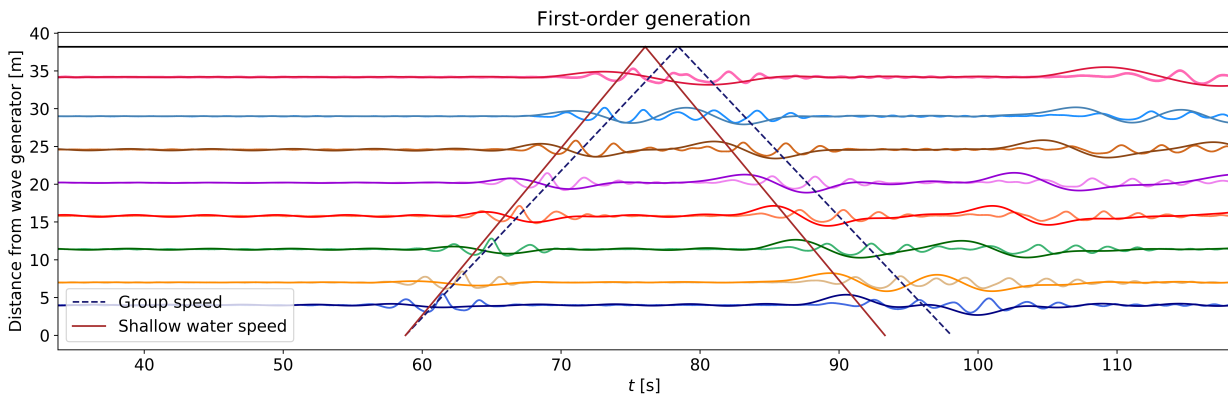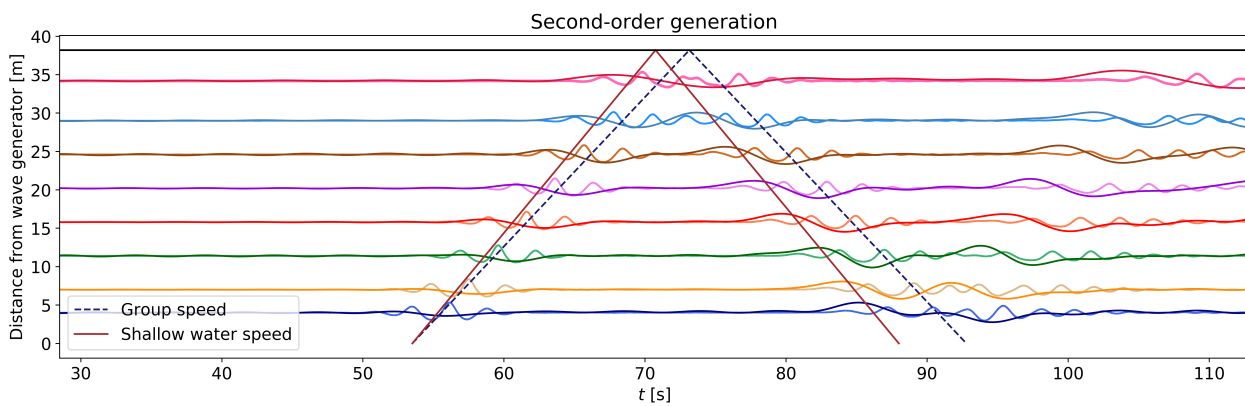Figure 4.4: Case 1: First-order wave generation. Super-harmonic components propagating through the flume are shown.

Figure 4.5: Case 1: Second-order wave generation. Super-harmonic components propagating through the flume are shown.

Figure 4.4 and 4.5 show the super-harmonic components derived from the total signal. Again, just as expected, using first-order generation additional spurious waves are generated and using the second-order correction these spurious waves are cancelled out.

Results case 3

Because the dimensionless water depth for this case is quite low ($kh = 0.53$), the difference between the group and shallow water speed is much less than it was for case 1. Therefore it takes more time for the spurious wave to separate from the group. This can be observed, and must be taken into account when viewing the following figures.

Figure 4.6: Case 3: First-order wave generation. The total surface elevation (lighter lines) and sub-harmonic waves (darker lines) propagating through the flume are shown.

Figure 4.7: Case 3: Second-order wave generation. The total surface elevation (lighter lines) and sub-harmonic waves (darker lines) propagating through the flume are shown.

Figure 4.6 shows the expected result, a spurious wave that travels (somewhat) faster than the group in the form of a set-up can be identified. Figure 4.7 however shows a remarkable result. There seems to be no to little difference between the first- and second-order result as also in the figure with the second-order correction a spurious wave (of the approximate same size as for first-order generation) is visible.

Results of the super-harmonic components were, on contrary to the sub-harmonic components, as expected (no spurious waves for second-order generation) for case 3 and are therefore not included in this chapter but can be looked up in appendix F.

Conclusion

Using the figures presented in this section it can be concluded that the second-order wave generation seems to work sufficiently for cases with a dimensionless depth equal and larger than $kh = 1.44$. For cases with a smaller dimensionless depth, however, the second-order correction does not provide the expected results. Because there seems to be no difference between first- and second-order correction it is assumed that the second-order correction is not 'large' enough.

It must be noted that the results shown in this section do *not* include ARC. Although the conclusions drawn for case 3 with ARC remain the same, the inclusion of ARC in case 1 results in a remarkable spurious set-down for second-order generation. Corresponding figures can be looked up in appendix F. Apparently the results of second-order generation can differ with and without ARC. Because ARC will be used during the rogue wave tests, attention is given to this discrepancy.

4.4 Proposed solution to sub-harmonic correction

Considering the results presented in figure 4.7 it is concluded that the second-order correction for the sub-harmonic components is not sufficient for case 3 (see table 4.1 for details) as there is no to little difference between the size of the spurious waves using first- and second-order steering. To asses the paddle signals calculated by the software AUKE/PC, relevant theory of second-order generation derived by van Leeuwen and Klopman (1996) is reviewed. According to the manual of the paddle software AUKE/PC, this theory is applied for the calculation of the second-order correction.

It must be noted that due to limited time and the assumption that only the sub-harmonic component needs to be adjusted, paddle signals are not constructed from scratch. Therefore not all wave generation theory is repeated and some of the formulas presented in van Leeuwen and Klopman (1996) are written in a different form.

Theory

The following equations are a repetition of relevant equations from van Leeuwen and Klopman (1996). The wavenumber k and wave length L are determined using the dispersion relation. h Is the water depth, c_g the group velocity, T the wave group peak period and ω the angular wave frequency.

$$n = \frac{1}{2} + \frac{kh}{\sinh 2(kh)} \tag{4.1}$$

$$c_g = \frac{1}{2}\left(1 + \frac{2kh}{\sinh(2kh)}\right)\frac{L}{T} \tag{4.2}$$

The term $h + l$ in equation 4.3 represents the type of wave board used in the flume. h Represents the water depth and $h + l$ the rotation arm of the paddle board. For a purely rotational wave board $l \to 0$ and for a purely translating wave board, which is the type of wave board at the considered flume, $l \to \infty$. This means that the term $\frac{2\cosh^2 kh}{k(h+l)}$ in this case equals zero.

$$B = \frac{2\omega}{k(\sinh 2kh + 2kh)}\left(\sinh 2kh - \frac{2\cosh^2 kh}{k(h + l)}\right) \tag{4.3}$$

In equation 4.4 X_{11} represents the first order paddle position. As the first order paddle position can be calculated using AUKE/PC, this equation is rewritten in order to find the complex amplitude of the first order waves A. f_{GAIN} Is an empirical factor which is equal to 0.8 for the wave board at TU Delft. Van Leeuwen and Klopman (1996) used this equation to calculate X_{11} with the knowledge that the magnitude ($|A|$) of A equals the envelope of the wave group time series (which is derived from a first-order spectrum). Remarkable however is that using the last approach the first-order paddle signals (AUKE/PC and theory) differ a factor (slightly dependent on the peak period) of approximately 3. It is assumed that this is an empirical factor corresponding to the wave board at this laboratory and is at this moment unknown. Therefore A is calculated using the calculated AUKE/PC first-order paddle movement.

$$A = X_{11}\frac{2\omega B}{gi}f_{GAIN} \tag{4.4}$$

In equation 4.5, X_{10} Is the second-order sub-harmonic paddle movement and R is a constant dependent on the type of wave board. For a non-rotational wave board (purely translating or piston-type) R equals 1. $|A|$ is the envelope of the surface elevation in time and the overbar denotes time averaging. f_{ARC} is an additional factor to include ARC which is estimated to be equal to $\sqrt{2}$. It will be concluded however that this estimated factor does not lead to the desired results and should therefore be investigated further. For tests with ARC it is recommended in the mean time to not include ARC in the calculation, which means that the first- and second-order paddle movement is calculated without ARC (ARC off) and the new sub-harmonic paddle movement is calculated using these signals and with $f_{ARC} = 1$, but is included during generation of the waves using the standard program

"Wavegenerator Control". Including ARC during generation can thus be put *ON* and *OFF* independently of the method to calculate the paddle movement.

$$X_{10} = \frac{f_{ARC}}{f_{GAIN}} R \frac{gc_g(2n - \frac{1}{2})}{h(gh - c_g^2)} \int_0^t (|A|^2 - |\bar{A}|^2) dt \tag{4.5}$$

The Matlab scripts of the presented theory can be found via `https://data.4tu.nl/Delft_University_of_Technology` and by typing "Doeleman" in the search box. The "Readme.txt" file provides information about each script file.

Paddle signal analysis

The two upper plots of figure 4.8 are the first- and second-order paddle signals that have been calculated using the AUKE/PC software. It can clearly be seen that there is a small (sub-harmonic) difference between the signals. The bottom plot shows the sub-harmonic signals filtered from the AUKE/PC signals (first- minus second-order with a low-frequency filter) in red and yellow and the 'new' sub-harmonic signal calculated using the theory presented above in blue and green. A check has been done to ensure that the theoretical and applied sub-harmonic paddle movement (by filtering the total adjusted signal) match. It can be seen that the signals only differ slightly at the beginning and end of the signal. This is, because a taper function has been applied to the total signal to ensure smooth movement of the wave board.

Figure 4.8 also includes the paddle movement (η_{pad}) with and without ARC. ARC ensures that the paddle moves back- and forward in case of a higher and lower water level respectively than would be expected in order to absorb a reflected wave. One can imagine that in case of second-order paddle movement the steering signal should be larger as the ARC would otherwise detect it as a reflected wave. Furthermore, a large difference in the sub-harmonic amplitude can be observed in figure 4.8. This supports the suggestion in section 4.3.2 that the second-order correction was not large enough.
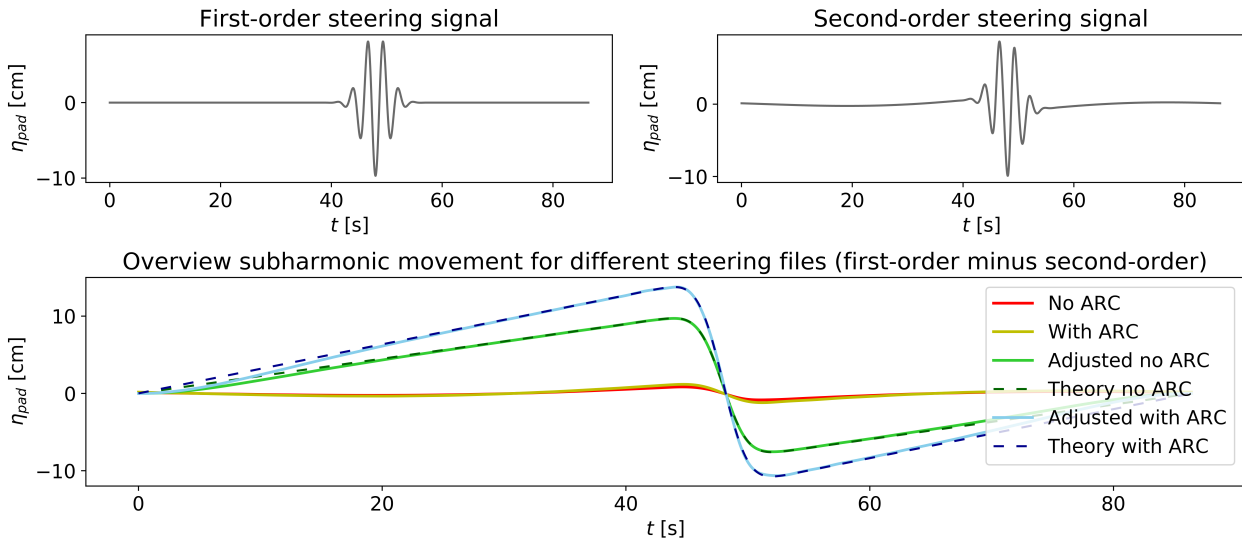
Figure 4.8: Case 3: Comparison sub-harmonic paddle movements. η_{pad} represents the paddle movement.

4.4.1 *Flume results*

Figure 4.9 shows the results of the adjusted paddle signal. The adjusted paddle signal is the second-order paddle signal calculated by AUKE/PC with the AUKE/PC sub-harmonic replaced with the newly calculated sub-harmonic movement using theory presented in section 4.4. It can be seen that the spurious wave is now eliminated. Also for the other two cases, the newly calculated sub-harmonic ensured the elimination of spurious waves, see appendix F.
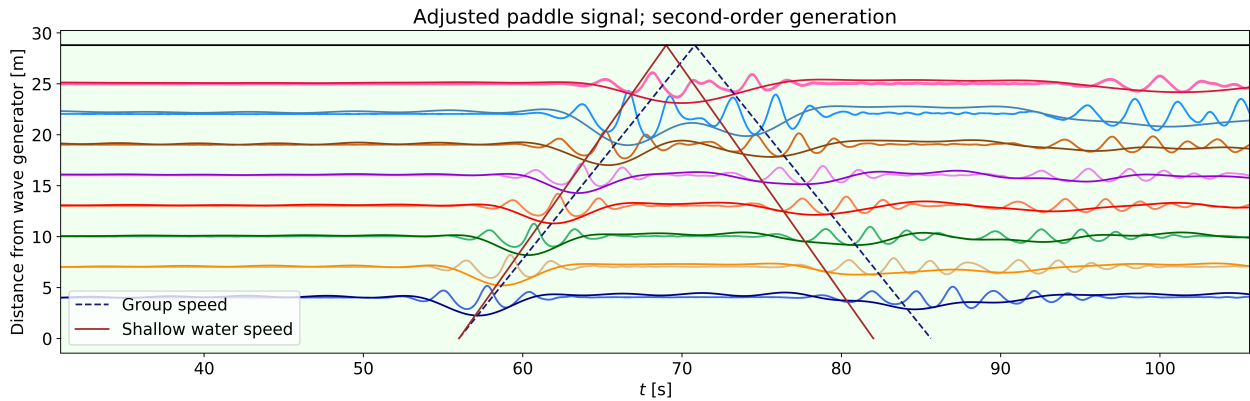
Figure 4.9: Case 3: Adjusted second-order wave generation. The total surface elevation (lighter lines) and sub-harmonic waves (darker lines) are shown.

The flume results obtained with ARC, however are not as expected. As noted at the end of section 4.3.2, for case 1 a spurious 'set-down' was observed. Using the adjusted paddle signals a spurious set-down is now observed at all cases. It is assumed that the calculated paddle movement is too large (over compensating). Therefore, a test has been performed with the adjusted paddle signal without ARC in the calculation but with ARC during the test. ARC during generation can thus be switched *ON* and *OFF* independently from inclusion in the calculation. The results for case 2 and case 3, see figure 4.10 look as desired. Using this method on case 1 however, did *not* lead to the desired results: still a set-down is visible, see appendix F. This is further elaborated in section 4.4.3.
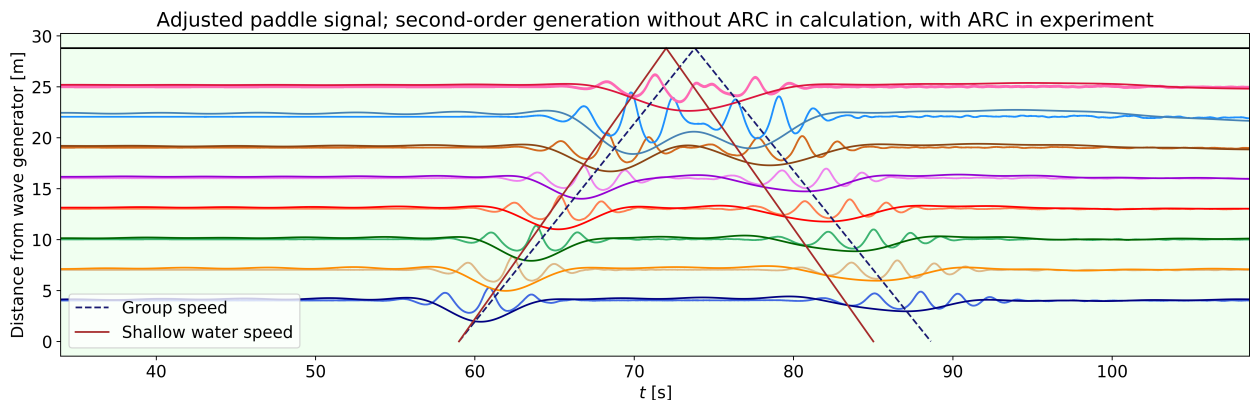
Figure 4.10: Case 3: Adjusted second-order wave generation without ARC in the calculation, with ARC during generation. The total surface elevation (lighter lines) and sub-harmonic waves (darker lines) propagating through the flume are shown.

Spectral analysis

To ensure that the adjusted paddle signal also represents the input wave group (time series which is used to calculate the paddle signals) as well as the AUKE/PC wave group, a spectral analysis is performed. Again, the adjusted paddle signal is the second-order paddle signal calculated by AUKE/PC with the AUKE/PC sub-harmonic replaced with the newly calculated sub-harmonic movement using theory presented in section 4.4. The top and right plots in figure 4.11 represent the analysed wave groups. The parameters in the plot titles are determined using their 'grassy' spectra. The left bottom plot shows the spectra of the wave groups using a 'block length' of 7 (average is taken over 7 discrete frequencies) for clarity.
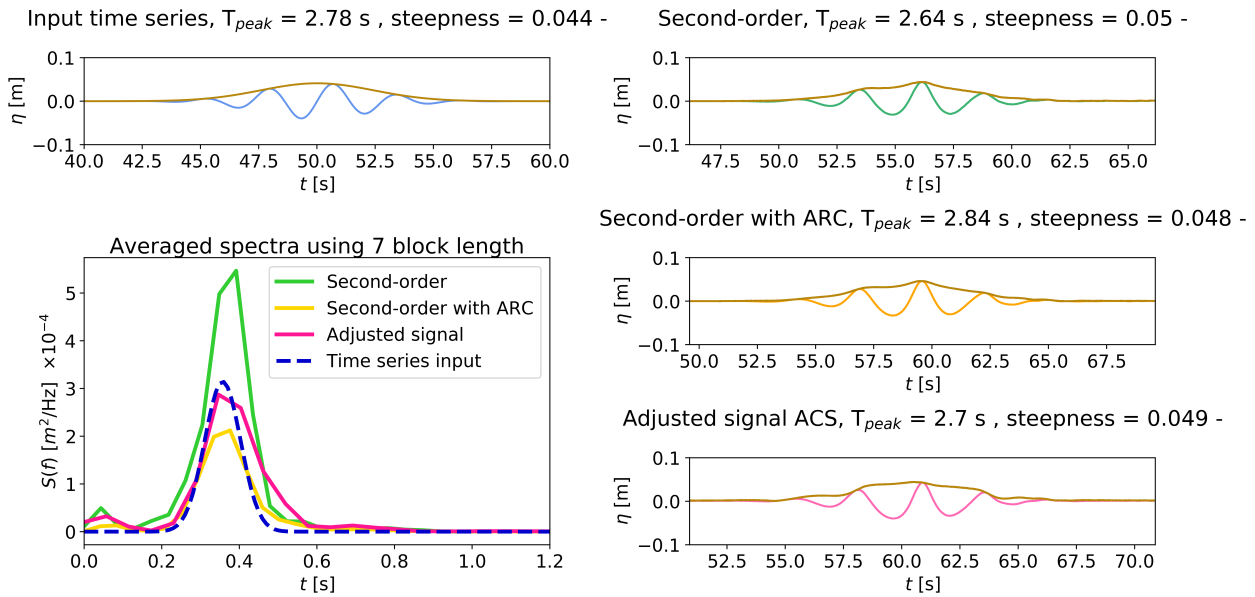
Figure 4.11: Case 3: Spectral analysis of the input and measured wave groups in the flume. The right plots show the measured wave groups (including their envelope shown in gold) in the flume using the paddle signals as specified in their title. The paddle signals are calculated using the top left time series. The averaged spectra of the wave groups are shown in the bottom left plot.

It can be seen that the wave group measured in the flume using the adjusted paddle signal without ARC in the calculation but with ARC *ON* while generating, actually gives the best results compared with the input (desired) time series.

4.4.2 Irregular waves

Because the experiments in this thesis require irregular wave tests with ARC, the adjusted paddle signal is also assessed for irregular waves. The complex amplitude A is now calculated in frequency space and transformed back to the time domain as the constant B is dependent on frequency.

Figure 4.12 shows the grassy spectra as the result of the following paddle signals: AUKE/PC with ARC (upper left), AUKE/PC without ARC in calculation but with ARC in generation (ACS, upper right) and the adjusted paddle signal without ARC in calculation but with ARC in generation (ACS, lower left). The input Gaussian spectrum is plot on top of the spectra with a blue dashed line. In figure 4.12 also the averaged spectra are shown in the lower right plot for easier visual comparison. Remarkable is that in terms of spectral significant wave height the AUKE/PC with ARC shows the best result, see the calculated H_{m0} corresponding to each plot in their title. It must be noted that the spectra in figure 4.12 are not filtered on incoming waves. This means that reflections are also included (the wave absorber detailed in section 3.3.1 was installed before these tests). Remarkable in figure 4.12 is the distinct beating/bumps of the spectral density. This pattern of 5 bumps per 0.2 Hz is thought be due to reflections, see section 6.4 for an elaboration.

Concluding, adjusted irregular paddle signals seem to give good enough results considering the spectral analysis, comparison with 'original' AUKE/PC results and time constraints in the flume. It is important, however, that the H_{m0} for the irregular wave tests are checked as these might turn out larger than expected.
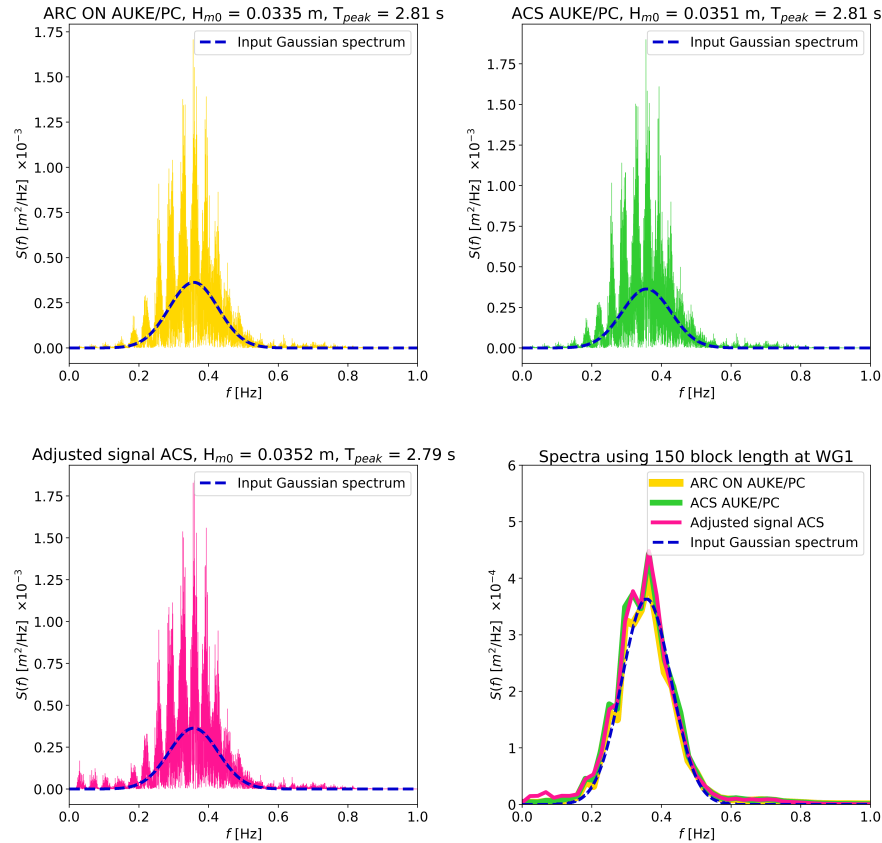
Figure 4.12: Irregular wave spectra measured at 5 meter distance using different paddle signals. The input Gaussian spectrum has a H_{m0} of 0.0321 m and T_{peak} of 2.8 seconds. 'ACS' means that ARC is used during wave generation but is not included in the calculation of the paddle signal.

4.4.3 Conclusion and recommendations

It has been shown that the adjusted paddle signals without ARC show good results: spurious waves are eliminated. This paddle signal is created as follows. First, the first-order and second-order paddle movement are calculated using AUKE/PC. Hereafter, the second-order movement is calculated by subtracting the second-order with the first-order signal. Next, the sub- and super-harmonics are separated at $f = 0.1$ Hz. Following, the correct sub-harmonic steering is calculated using equation 4.5. Last, total paddle movement is obtained by adding the super- and correct sub-harmonic steering to the first-order signal (or by replacing the correct sub-harmonic movement with the second-order AUKE/PC sub-harmonic movement).

Including ARC in both the calculation and generation results for all three cases in a spurious set-down. Using the method "ACS" described in section 4.4.2, which includes ARC in the generation but not in the calculation, gives acceptable results for cases 2 and 3, $kh < 0.91$. For case 1 on the other hand $kh = 1.44$ this method still results in a set-down. The set-down is smaller than with inclusion of ARC in the calculation and generation but is still significant. Also, it must be noted that a small deviation in H_{m0} can be observed using the ACS method for all cases (figure 4.12). Including ARC, it is concluded that for wave fields with $kh < 0.91$ the proposed method with ACS should be used, as this provides significant improvement. For $kh > 0.91$, it is advised to use the "standard" AUKE/PC calculation as the adjusted signal also results in a set-down and is therefore not necessarily better. The used Matlab scripts can be found via `https://data.4tu.nl/Delft_University_of_Technology` and by typing "Doeleman" in the search box. The "Readme.txt" file provides information about each script file.

As the solution for $kh > 0.91$ including ARC results in a set-down, it is recommended to investigate the difference between the calculation of the paddle signals with and without ARC. Hereafter the total sub-harmonic movement should probably be decreased as the spurious set-down is thought to be the consequence of overcompensation. Finally, the new paddle signal must be tested in the flume to ensure correct second-order wave generation.

<div align="right">

5

</div>

Data processing

In this section the data processing methods are discussed. The instruments used for the experiments, described in section 3.4, collect 'raw' data. This data needs to be processed before it can be used for further analysis. This chapter is split into three sections: processing the wave gauge plus EMF data, a reflection analysis using the wave gauge and EMF data and a processing method for the laser data. All data processing is performed using Python.

5.1 Processing wave gauge and EMF data
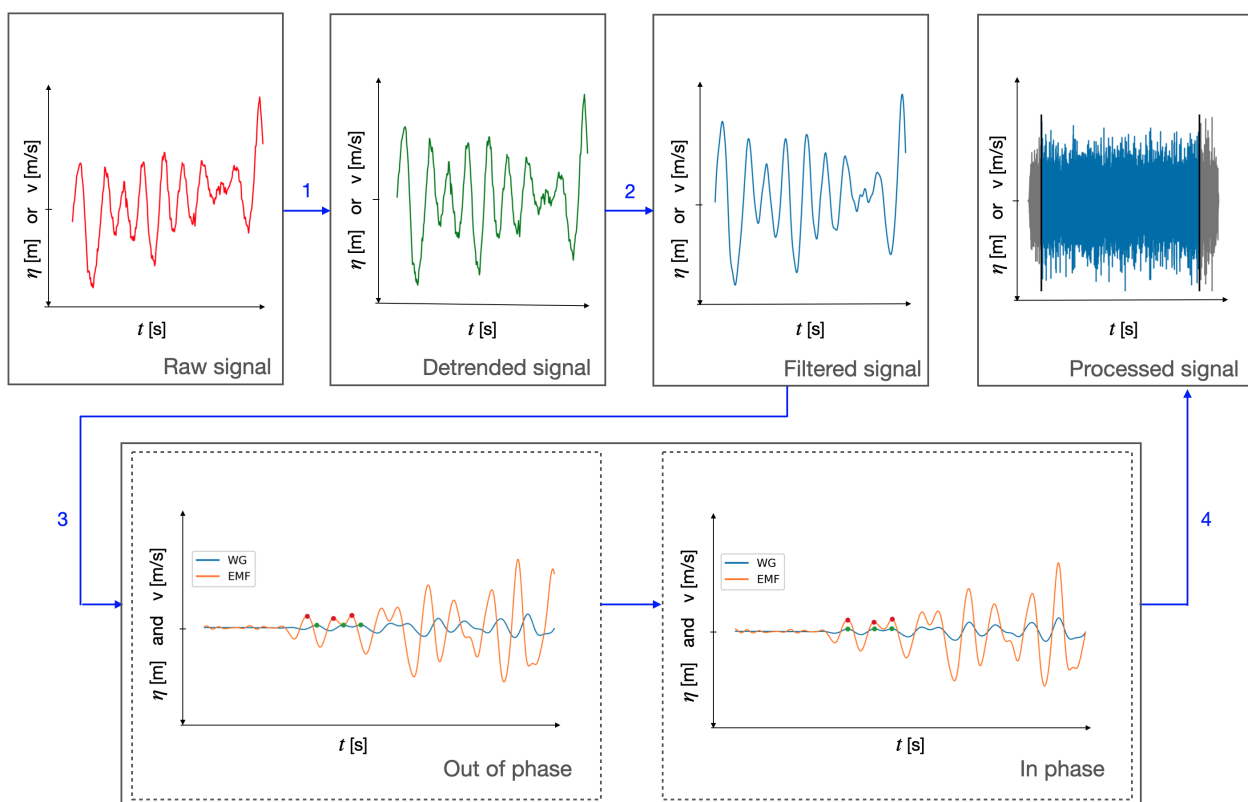
Figure 5.1: *Four-step processing method for wave gauges and EMFs. With η representing the surface elevation and v velocity.*

Figure 5.1 shows the flowchart used to process the collected wave gauge and EMF data. The first step consists of 'detrending' the data. Due to for example temperature changes during the more than 2 hour long experiments a linear trend can be present in the data. This can be seen in the first (left upper) plot. The second step consists of eliminating the high frequency noise, which is not part of the wave motion, using a low-pass filter with a cutoff of 2 *Hz*. The result can be observed in the third top plot. The third step is the phase calibration of the associated wave gauges and EMFs. This calibration is required, because the probes can have a slight phase difference if, for instance, one of the probes is placed some millimeters in front of the other. This phase difference is assessed by identification of the first three peaks (green and red dots in figure 5.1) in the wave record. The first waves of the wave record are not contaminated with reflected waves and therefore the velocity and surface

elevation must be in phase. The difference in time between the wave gauge and EMF peaks are averaged and is used to 'roll' the EMF data. Result is a shift of the EMF data over time. The values that 'roll' beyond the total duration are re-introduced at the start. The final, fourth, step is the selection of a stationary record. This is necessary to ensure that the experiment is completely stationary; time between the start of the measurements and wave machine is eliminated, reflections are continuously present and the paddle movements are completely build-up. Because the paddle signals are adjusted a taper-function, which gradually builds-up and breaks-down the paddle excursion, is applied to ensure that no harmful accelerations are present. By eliminating some time at the beginning and end of the experiment the effect of rolling the EMF signal is also eliminated. It is chosen to select a stationary signal of exactly 2 hours. This means that 10 minutes at the start and 15 minutes at the end of the measurements are removed.

5.2 Reflection analysis

As the flume is not of infinite length, reflections take place at the end of the flume. The total wave field therefore consists of incoming waves (waves that one wants to measure) and reflected waves (waves reflect at the end of the flume and travel in opposite direction, contaminating the wave field). To reduce the amount of reflections during the experiments a gravel wave absorber is installed. For details see section 3.3.1. It must be questioned however *how much* of the reflections are absorbed (or still present) in the flume? To answer this question the 'vertical array' or also called 'co-located gauge' method is used. This method is based on linear wave theory and requires a wave gauge and (horizontal) velocity meter to be placed in a vertical array (Hughes, 1993b,a). For this thesis, this method is preferred over the spatially-separated methods as the number of available wave gauges is limited and the spacing between the gauges should have been changed numerous times, costing time and increasing the possibility of errors.

The vertical array method is a frequency domain reflection analysis technique using linear wave theory that links the surface elevation and the horizontal particle velocity at each frequency component *i* using a 'velocity transfer function'. Following, incident and reflected wave amplitudes and phases can be calculated for each frequency. Using an inverse Fourier transfer, the (split) surface elevation can again be obtained. This method is elaborated in appendix C and can thus be used to filter the total wave field on incoming waves. Besides obtaining the incident and reflected surface elevation, also the respective wave spectra can be derived. Using these wave spectra the dimensionless frequency dependent reflection coefficient can be calculated according to equation 5.1. $S(f)$ Is the discrete energy density spectrum for the incoming (I) and reflected (R) waves. The reflection coefficient consequently also equals the reflected divided by the incoming discrete spectral amplitudes ($a(f)$). As it is questioned whether the linear method includes the separation of bound (incoming) and free (reflected) sub-harmonic waves an adjusted Guza method, see appendix C, is also used for the low frequency region (<0.2 Hz).

$$K_r = \sqrt{\frac{S_R(f)}{S_I(f)}} = \frac{a_R(f)}{a_I(f)} \tag{5.1}$$

Figure 5.3 shows the results of the reflection analysis for tests 2 and 6 at WG1 (x=-3 meter, between paddle and depth transition) with a water depth of 0.5 and 0.35 meter, spectral bandwidth of 0.15 and 0.25 and spectral amplitude of 5.36 and 1.94 centimeter respectively (see the experimental program presented in table 3.1). For visualisation and acceptable reflection coefficient results the wave spectra are calculated with a 'block' length of 5. This block length means that an average of the spectral density is taken over 5 discrete frequency components. The location of WG1 is chosen, because at this location the sub-harmonics can be separated in bound incoming and free reflected waves. As according to the investigated rogue wave mechanism free sub-harmonic components arise due to interactions with the depth transition, at all other wave gauge locations the incoming wave field will consist of bound ánd free sub-harmonic waves.

It can be seen in figure 5.3 that the vertical array and adjusted Guza method almost give the same results. Remarkable is the high amount of reflections in the sub-harmonic region (<0.2 Hz). This observation is thought to be due to less effectiveness of the wave absorber for low-frequency waves. Figure 5.3 also shows that the amount of reflections increases between the tests with a decreasing water depth. This is assumed to be due to decreasing effectiveness of the gravel beach for smaller amplitude waves. As the results of test 2 and test 6 are

representative for the tests 1-4 and 5-8, the amount of reflection in the high spectral density area is estimated at ±30%. The reflection percentage in the low-frequency region is estimated at ±60%. An overview of the reflection percentage of all tests is given in appendix C.
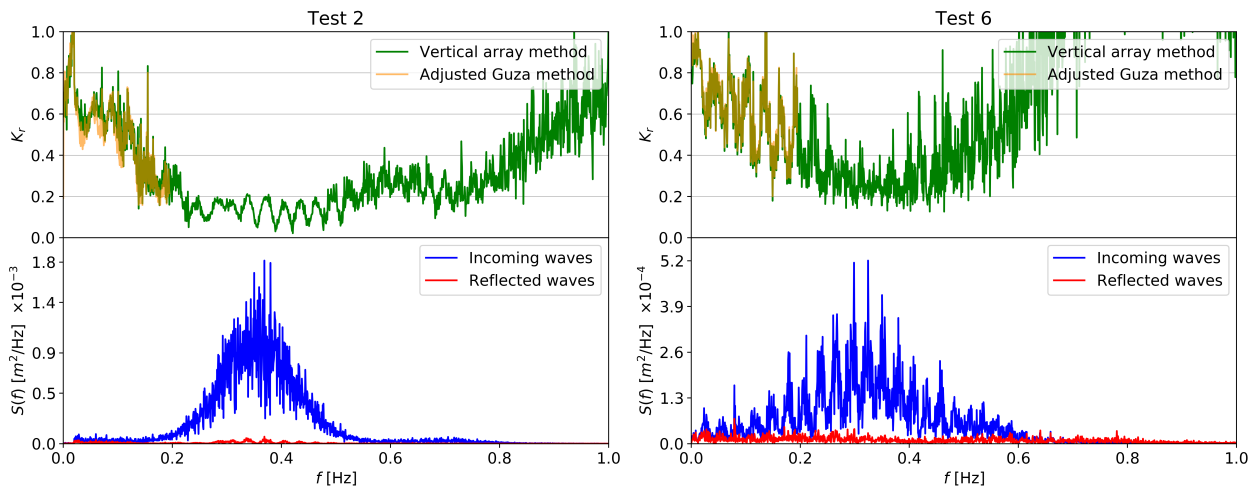

Figure 5.2: *Reflection analysis test 2 (left plots) and test 6 (right plots) at WG1. Upper plots represent the frequency dependent reflection coefficient. The lower plots show the wave spectra of the incoming (blue) and reflected (red) waves.*

Ideally, using a reflection analysis method all real reflections are eliminated from the total wave field and the real incoming wave field is left. However, taking the following four consideration into account it is chosen not to eliminate the reflections, and therefore the total wave field is used for further analysis. First, it is questioned whether the linear vertical array method correctly separates the bound high-frequency waves (>0.8 Hz). Second, due to limited instrument availability, velocity meters are not present next to every each wave gauge. An attempt has been made to develop a reflection propagation method to be able to filter the total wave field at every location, the results however are found to be insufficient. See appendix C for an elaboration. Third, as free sub-harmonic waves arise due to interactions with the bottom topography and the adjusted Guza method only detects bound waves and consequently labels all other waves as reflections, the correctness of the separation method must be questioned for filtering the sub-harmonic components at WG2 till WG8. The error of the Guza method is however expected to be small as the group velocity approaches the shallow water speed. This means that the speed of the bound and free waves are similar and free waves are not incorrectly labelled as reflections. Fourth, the amount of reflections (±30%) in the high spectral density region is considered not that significant. It must be noted, however, that the amount of reflections in the sub-harmonic region are significant. Nevertheless, as described in the second and third consideration, it is not possible to correctly separate the incoming wave field. Possible effects that arise because the total wave field is not filtered on reflections is addressed when necessary in the following chapters.

5.3 Laser scanner

In this section a simplified processing technique is discussed to roughly analyse the potential of the laser scanner data in comparison with the wave gauge data. The output of the laser consists of three files; *.data, *.properties and *.script. Using the SOPAS Engineering Tool the *.data can be exported to a *.CSV. It must be noted that for tests of approximately 2.5 hours, angular resolution, α of 0.1667° and scan frequency of 25 Hz the *.CSV files will have a very large size (>10 GB). Because SOPAS ET has a limitation on the size of the export CSV, the data per test must be separated in two to three separate CSV files. Once the CSV file is obtained, it can be opened in Excel (Microsoft) or Numbers (iOS). The CSV data processed in this thesis include; the start angle, the angular resolution, (total) distances and the Received Signal Strength Indicator (RSSI).

Knowing the slant angle ($\phi = 10°$), see figure 3.7, angular resolution and using the knowledge of trigonometry, the measured total distances can be converted to X and Y, which are the sampling distances along the flume and distances over the vertical (in this case the surface elevation) respectively. Since one is only interested in

measurements in the flume, a start angle α_i and final angle α_{i+m} is determined. This can be seen in equation 5.2. Following, using equation 5.3 and 5.4 the X and Y distances can be calculated.

$$\alpha_{i+n} = \alpha_i + \alpha * n \qquad n = 0, 1, 2..., m \tag{5.2}$$

$$X_{i+n} = D \sin \alpha_{i+n} \qquad n = 0, 1, 2..., m \tag{5.3}$$

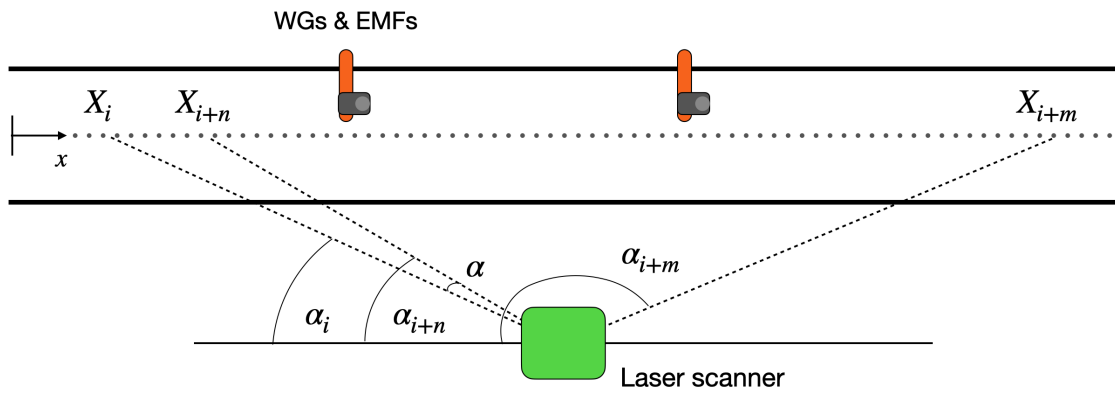$$Y_{i+n} = D \cos \phi \cos \alpha_{i+n} \qquad n = 0, 1, 2..., m \tag{5.4}$$

Figure 5.3: Schematic for processing the distances measured by the laser scanner using the angular resolution α.

To obtain a time series of the surface elevation, a location x_{i+n} along the flume is chosen. Since the spacing between two successive measuring points is only ±2 or ±7 centimeters (for α = 0.1667° or 0.667° and D = 6.3 m), this means waves can be analysed with high resolution across the scanned flume length in comparison with wave gauges. After the selection of a location X, the signal is averaged over time to eliminate noise. The new signal is set at 5 Hz, thus averaging over 5 or 10 measurements dependent on the scan frequency. Hereafter, just as for the WG and EMF data, the new signal is detrended and hereafter filtered to eliminate remaining high frequency noise that is not part of the wave motion.

Data analysis

In order to correctly interpret results, the processed data must be checked/analysed. In this chapter, first the spectra of the tests are assessed using the wave gauge and EMF data. Hereafter the applied paddle signals are investigated. Next, possible influences on the results (comparison theoretical framework with experiments) are discussed. Hereafter, the energy density 'beating' which can clearly be observed in the 'grassy' spectra is discussed. Last, the surface elevation measurements of the laser and wave gauges are compared in order to asses the potential use of the laser scanner for similar experiments.

6.1 Spectral analysis

In this section the spectra of the different tests are assessed using the processed wave gauge (WG) and velocity meter (EMF) data. This is done to ensure that the input Gaussian spectrum corresponds to the actual generated waves which are measured in the flume. This is important, because a significant part of the results will consist of a comparison between experiments and the statistical model which requires spectral parameters as an input.

Figures 6.1 and 6.2 show the measured spectra at the first wave gauge (WG1 which is located at x = -3 m and 5 meters away from the wave paddle) of tests 2 (h_d = 0.5 m, δ = 0.15) representative for tests 1-4, and test 6 (h_d = 0.35 m, δ = 0.25) representative for tests 5-8. See the experimental program presented in table 3.1 for more details per test. As WG1 is located between the paddle and the step it is assumed that the measured spectrum at this location should equal the input Gaussian spectrum. To easily asses if this is the case, the Gaussian (input and thus desired) spectrum is plot on top of the measured spectrum with a blue dashed line. The measured spectrum is plot without averaging (the grassy grey spectrum, ±130.000 discrete frequencies) and with averaging over a block length of 50 (±2.600 discrete frequencies) in red for easy comparison with the Gaussian spectrum. Using the grassy spectrum the spectral significant wave height, H_{m0}, is calculated. The difference between the input and measured spectrum is expressed as the percentage difference between the input and spectral significant wave height ($1 - Hm0_{Gaus}/Hm0$). This measure is put in the title of each plot. Appendix D gives a summary of the spectral deviations for each test with the step at WG1
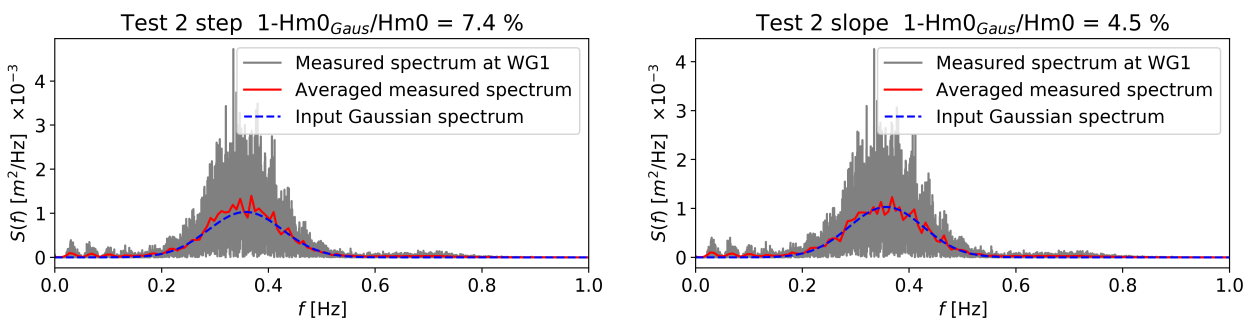

Figure 6.1: Test 2. Spectra measured at WG1 with a step (left) and slope (right). In gray the grassy spectrum is shown and in red the averaged spectrum with a block length of 50. The blue dashed line is the input Gaussian spectrum for reference. The spectra are representative for tests 1-4.

The input and measured spectra of test 2 are almost similar. Only a slight (expected) deviation is present due to the presence of bound sub-harmonic waves and influence of the adjusted second-order paddle signal (see section 4.4.2). An additional explanation for the small difference (±6%) in significant wave height is the presence of reflections in the flume due to its finite length and presence of the step or slope. This last suggestion explains the fact that the deviation in significant wave height is less for the tests with the slope (±2% in the figures 6.1

and 6.2) as a slope is a less reflective structure than a step (with the exemption of test 4 where the amount of reflections with the slope is found to be significantly larger than with the step). Concluding, considering test two, the difference between the input and measured spectra is so small that the deviation is considered negligible.
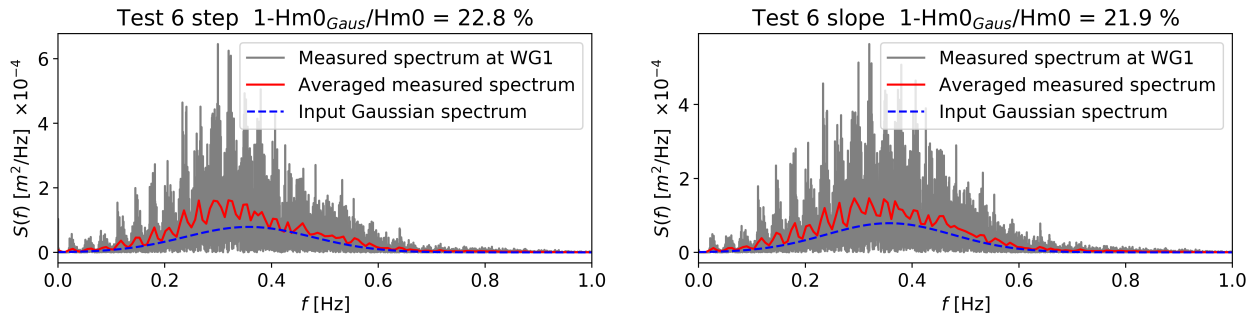

Figure 6.2: *Test 6. Spectra measured at WG1 with a step (left) and slope (right). In gray the grassy spectrum is shown and in red the averaged spectrum with a block length of 50. The blue dashed line is the input Gaussian spectrum for reference. The spectra are representative for tests 5-8.*

Remarkable however is that the input and measured spectra in test 6 (representative for tests 5-8), figure 6.2, shows such a significant difference in significant wave height that this deviation cannot be ignored and must be investigated further.

The difference between tests 1-4 and 5-8, besides the decrease in water depth, is the increase in spectral bandwidth. As in addition reflections might be a cause for the spectral deviation, it is hypothesized that waves from a broad spectrum are less well absorbed by the gravel beach. To asses the influence of the spectral bandwidth, tests 1, 2 and 4 have also been performed with an increase in bandwidth. The results of the spectra for test 2 with a bandwidth of $\delta = 0.15$ [-] and 2a $\delta = 0.25$ [-] are shown in figure 6.3. As expected, the same test with a larger spectral bandwidth shows a larger spectral deviation, which means that the spectral deviation is linked to the spectral bandwidth.
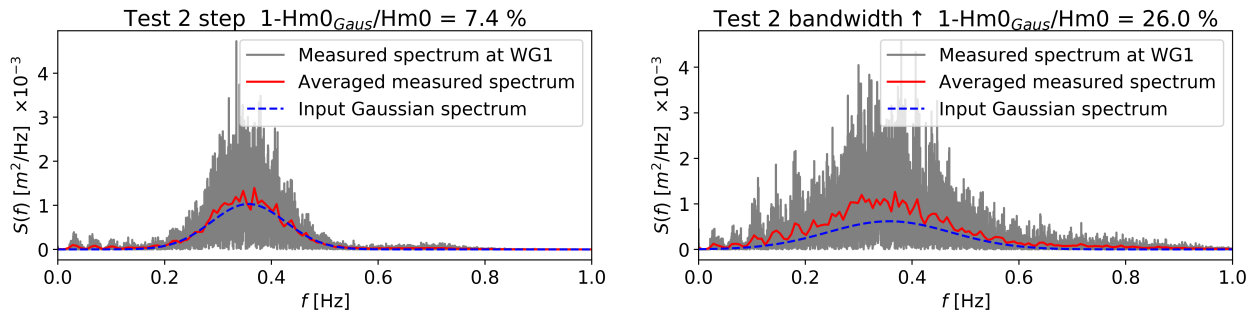
Figure 6.3: *Test 2. Spectra measured at WG1 with a bandwidth of $\delta = 0.15$ [-] (left) and with an increase in bandwidth $\delta = 0.25$ [-] (right). In gray the grassy spectrum is shown and in red the averaged spectrum with a block length of 50. The blue dashed line is the input Gaussian spectrum for reference.*

To assess whether the cause for the spectral deviation is indeed the hypothesized increase in reflections for broader spectra, a reflection analysis is performed for test 2 with a bandwidth of $\delta = 0.15$ [-] and 2a $\delta = 0.25$ [-]. The results are shown in figure 6.4. Remarkable is that little difference is present between the two frequency dependent reflection coefficients. Therefore, it is concluded that the deviation in significant wave height is not due to the presence of (additional) reflections.
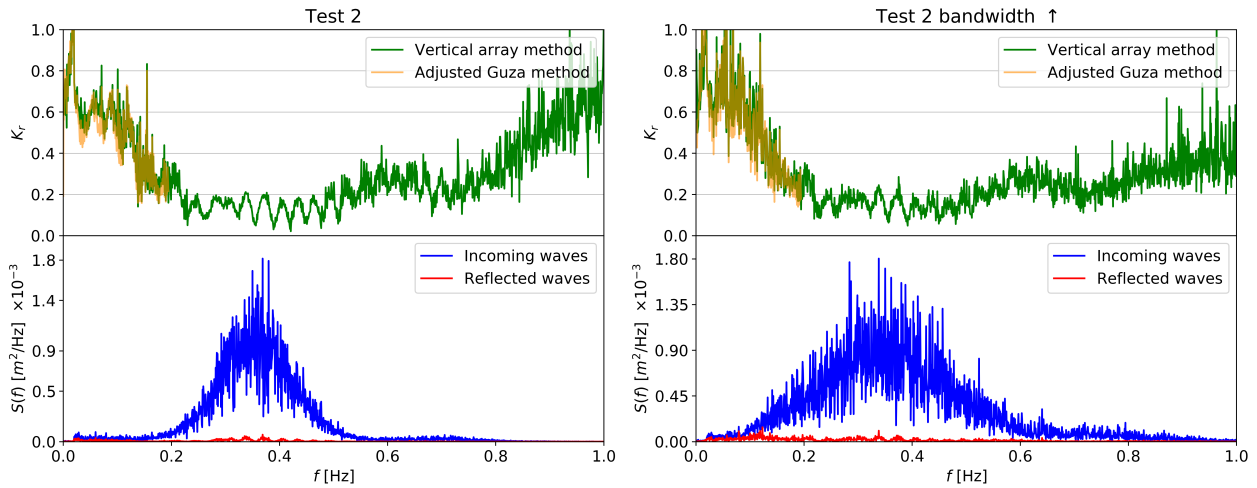
Figure 6.4: *Reflection analysis of test 2 with a bandwidth of 0.15 (left) and 0.25 (right) at WG5. The upper plots represent the frequency dependent reflection coefficient. The lower plots show the wave spectra of the incoming (blue) and reflected (red) waves with respect for frequency, f.*

Another possible explanation of the difference between the measured and input spectra is that the wave paddle "simply" did not generate the input spectrum. This suggestion is further investigated in section 6.2.

It must be noted that the spectra presented in figures 6.1, 6.2 and 6.3, show a remarkable 'beating' or presence of energy 'bumbs'. These bumbs seem to have a constant pattern of 5 beatings per 0.2 Hz. This observation is further elaborated in section 6.4.

6.2 Wave paddle analysis

To assess whether the spectral difference could be due to incorrect or deviating paddle movements, first the probability density distributions (PDFs) of the surface elevation (η) at WG1 and of the used paddle excursion are calculated. This is done to check if the paddle signal matches the Gaussian, normally distributed input spectrum (kurtosis, $\kappa = 3$ and skewness, $s = 0$) and if/how much the waves measured in the flume deviate from this distribution. The paddle excursion ($\eta_{pad,m}$) is obtained from a measuring magnet attached to the wave paddle. This magnet is calibrated using a two-point method, maximal excursion forward and backward divided by the difference in Volt, at the end of the experiments. The standard deviation of the kurtosis of the paddle signal is calculated using a bootstrapping method which takes 1000 samples of a length of 1500 measurement points. Appendix D gives a summary of the measured paddle distribution including all tests with a step.
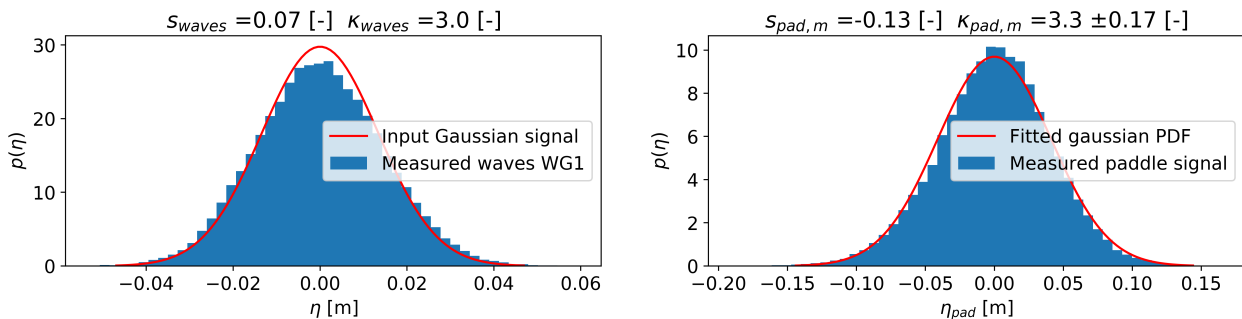
Figure 6.5: *Test 2. Probability density function of the surface elevation (η) at WG1 (left) and the measured paddle signal $\eta_{pad,m}$ (right) in blue. In the left plot the distribution of the input Gaussian spectrum is plotted in red. In the right plot a normal distribution is fitted using the paddle excursion parameters and also plotted on top in red.*
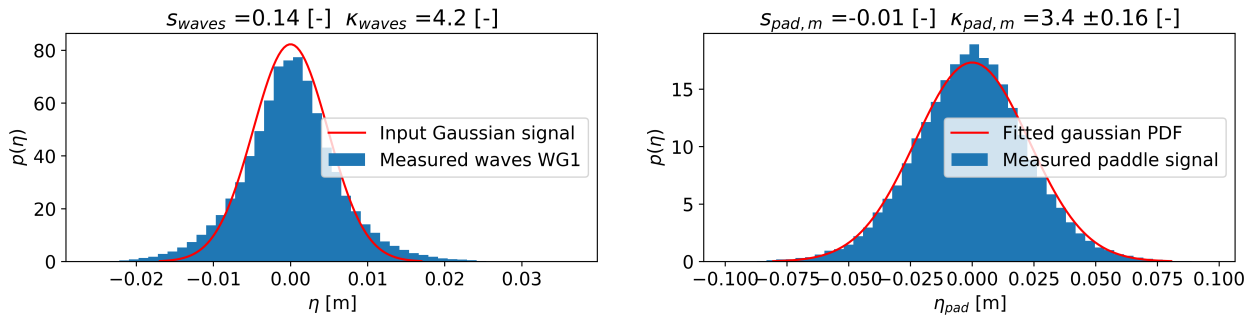
Figure 6.6: Test 6. Probability density function of the surface elevation (η) at WG1 (left) and the measured paddle signal $\eta_{pad,m}$ (right) in blue. In the left plot the distribution of the input Gaussian spectrum is plotted in red. In the right plot a normal distribution is fitted using the paddle excursion parameters and also plotted on top in red.

Figures 6.5 and 6.6 show that the paddle signals for both tests deviate somewhat from a normal PDF (kurtosis of approximately 3.4 while for a normal distribution kurtosis equals 3). This is therefore not completely in accordance with the Gaussian input spectrum. Surprisingly however, the measured results in the flume during test 2, see figure 6.5 do match with a normal distribution and is thus in accordance with the input Gaussian signal. On the contrary, figure 6.6 shows that the measured surface elevation for test 6 at WG1 does not match the normal distribution as it has an even higher value of kurtosis (larger tails, thus higher probability of- and higher maxima) than the kurtosis of the paddle. However, although the paddle signal is found to be non-Gaussian for both tests, because the kurtosis is of the same order and the wave spectrum is as desired during test 2, it is reasoned that the paddle signal distribution is not the cause of the spectral difference. The deviation in significant wave height should therefore be due to another unknown mechanism or process that takes place in the flume that has not been considered yet.

Because during the execution of the experiments it was noticed that for the tests with a larger bandwidth (δ >0.15 [-]) the waves and the paddle movements seemed rather large. A suspicion was raised that there might be some other paddle signal deviation that causes the mismatch for broader spectra. Because of this suspicion it was reasoned that although the paddle signal might have the same distribution as the desired spectrum, if the paddle movement is too large, it would also result in too large waves. Consequently this might result in a non-normal surface elevation distribution in the flume. To assess this suspicion first it is checked if the amplitudes of the paddle movement in the file $\eta_{pad,f}$ (calculated with AUKE/PC and hereafter the sub-harmonic adjusted) is comparable with the actual, measured paddle movement $\eta_{pad,m}$. Figure 6.7 shows the frequency dependent amplitude analysis of both paddle signals for test 2 and 6. It can be observed that there is some deviation between the measured (real) and input paddle movement. Because this deviation is small and assumed to be due to the ARC, it is concluded that the measured and input spectrum match.
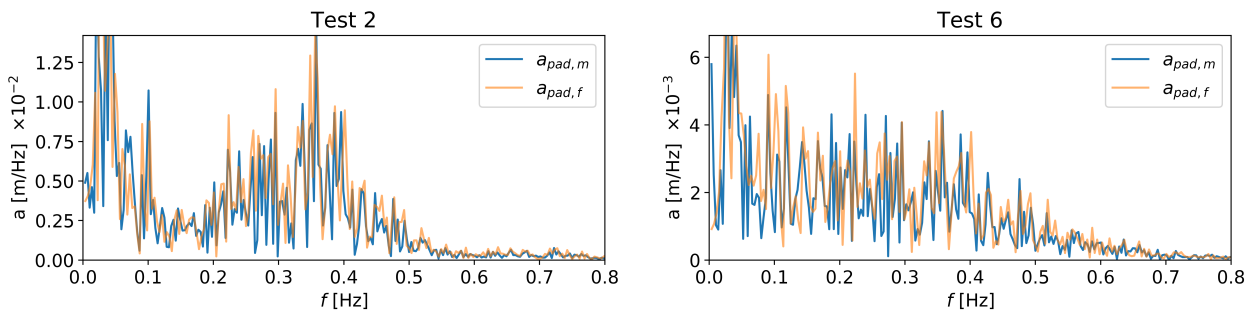

Figure 6.7: Amplitude spectrum averaged with a block length of 25 discrete frequencies of test 2 (left) and test 6 (right). In light orange the amplitude of the calculated input paddle movement $\eta_{pad,f}$ is shown. In blue the measured paddle movement $\eta_{pad,m}$ is shown.

Because the input and measured paddle movement match, the possible paddle deviation is sought in the calculation of the paddle movement. According to (simplified) linear wave generation theory, see equation 6.1, the

stoke of the paddle ($a_{pad,m}$) is related to the generated wave amplitude (a_{wave}) with the presented function consisting of k the wavenumber, h the water depth and f the discrete frequency Flick and Guza (1980). It is reasoned that the theoretical function should match for test 2 (representative for the tests with negligible spectral deviation) and should deviate for test 6 (representative for the tests with significant spectral deviation) as the waves for test 6 are too large.

$$\frac{a_{wave}}{a_{pad,m}} = \frac{2\sinh kh}{kh} \frac{kh\sinh kh - \cosh kh - 1}{\sinh kh \cosh kh + kh} \tag{6.1}$$

Figure 6.8 shows the results of the wave and paddle amplitude ratio in comparison with simplified linear wave generation theory. It can be seen that both test 2 and 6 roughly follow the theoretical ratio. All other tests show similar results and thus also match with the theoretical ratio. As the paddle movement (file) for test 6 matches the (too large) waves measured in the flume, an error is made in the calculation of the paddle movement. Concluding, this analysis substantiates the hypothesis that the calculated paddle amplitudes for the broad spectra are too large. The final question to be answered is why the paddle amplitude ís too large?
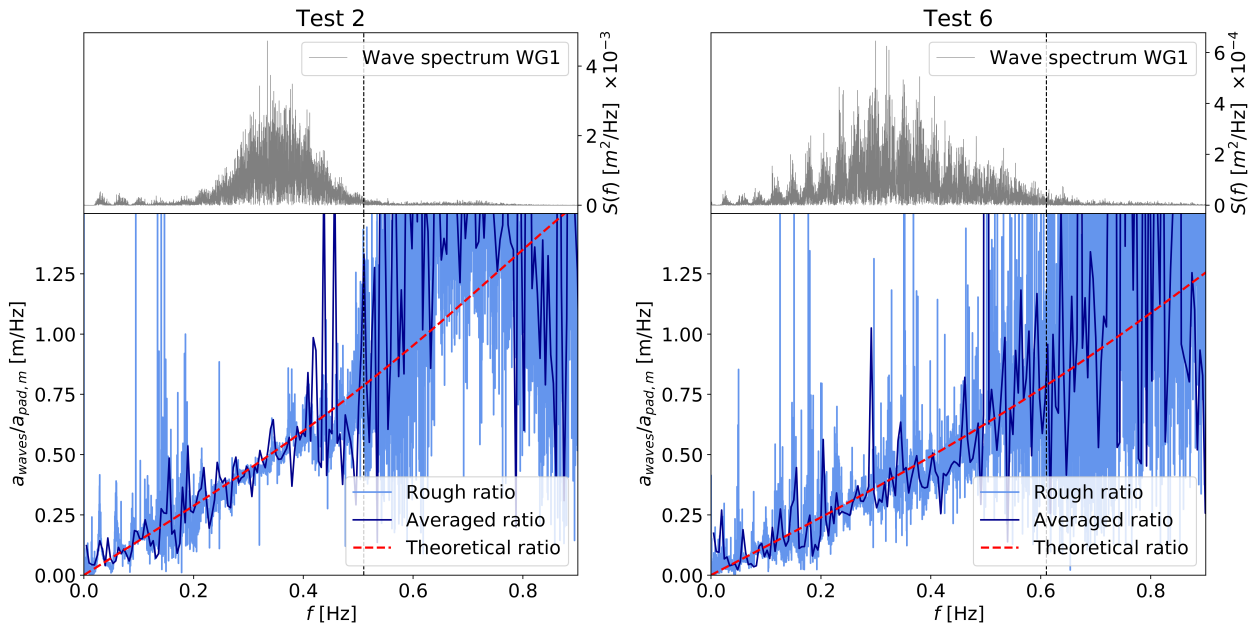
Figure 6.8: Amplitude analysis of test 2 (left) and test 6 (right). The top plots show the grassy spectrum to indicate the frequency regions with high spectral densities. The ratio of the measured paddle movement and wave amplitudes in comparison with simplified linear wave generation theory is shown in the bottom plots. In light blue the rough (grassy) ratio is shown. In dark blue the averaged ratio over 35 discrete frequencies is plotted. The theoretical ratio is shown in red.

Analysing the spectra of all tests again, including the steepness increase and decrease variants, it is noticed that test 6 with a steepness decrease does not have a significant spectral deviation although the spectral bandwidth is the same as the basis test ($\delta = 0.25$ [-]). After close inspection of the input spectra of test 6 and test 6b with steepness decrease, it is noticed that the first value of the spectral density (f=0) equal 0.000001 and 0.000000 m²/Hz respectively. As all other tests with a large spectral deviation also start at a value larger than zero (due to the large bandwidth), it is hypothesised that the corresponding paddle movement can not be calculated correctly by AUKE/PC if the input spectra has energy (even if it is very small) at $f \approx 0$ Hz. This hypothesis is validated by comparing the AUKE/PC paddle signals of test 6 and test 6 with the spectral density values at $f \approx 0$ to 0.000000 m²/Hz, now referred to as test 6-0. Just as expected, the spectral density of the paddle movement of test 6-0 is overall lower than test 6, see figure 6.9. It can therefore be concluded that AUKE/PC cannot calculate correct paddle movements for input spectra with spectral densities in the very low frequency region. It

is recommended that a cutoff is implemented in the software to prevent large deviations between the input and generated spectra for (similar) future research.
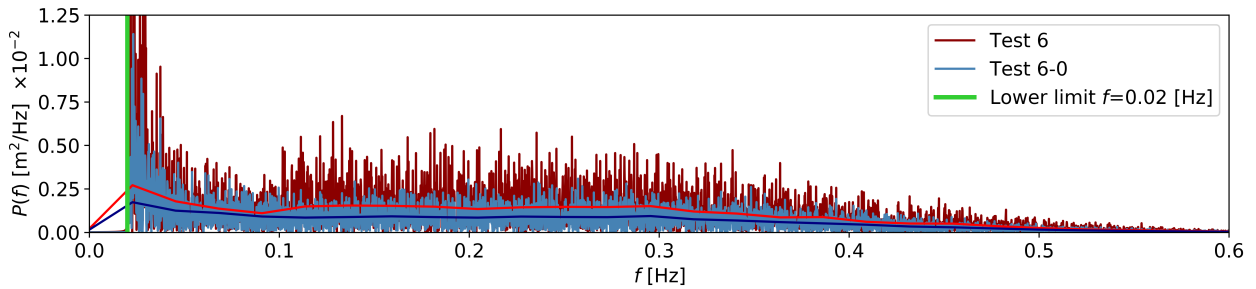

Figure 6.9: Paddle spectra $P(f)$ derived from the calculated paddle movement by AUKE/PC ($\eta_{pad,f}$) without second-order sub-harmonic correction. Test 6 is shown in red and test 6-0 is shown in blue. The grassy and averaged spectra of both tests are shows in their respective colors. The vertical green line shows the identified lower frequency limit.

6.3 Stokes second-order limit

Because the significant wave height for approximately half of the tests in flume was larger than desired and the significant wave heights were determined based on the upper limits of Stokes second-order wave theory (Ursell = 26), the waves for these tests are no longer within the limits of Stokes second-order theory. This can be observed in figure 6.10 where H_s equals the measured H_{m0} at WG1. As expected, basis tests 1-4 lie on the limit of Stokes second-order theory and tests 5-8 exceed the limit and are now, as shown in the figure, described by cnoidal wave theory. It can be seen that also the tests with bandwidth and steepness increase exceed the limit. The tests with a steepness decrease are located well within the Stokes second-order limit.
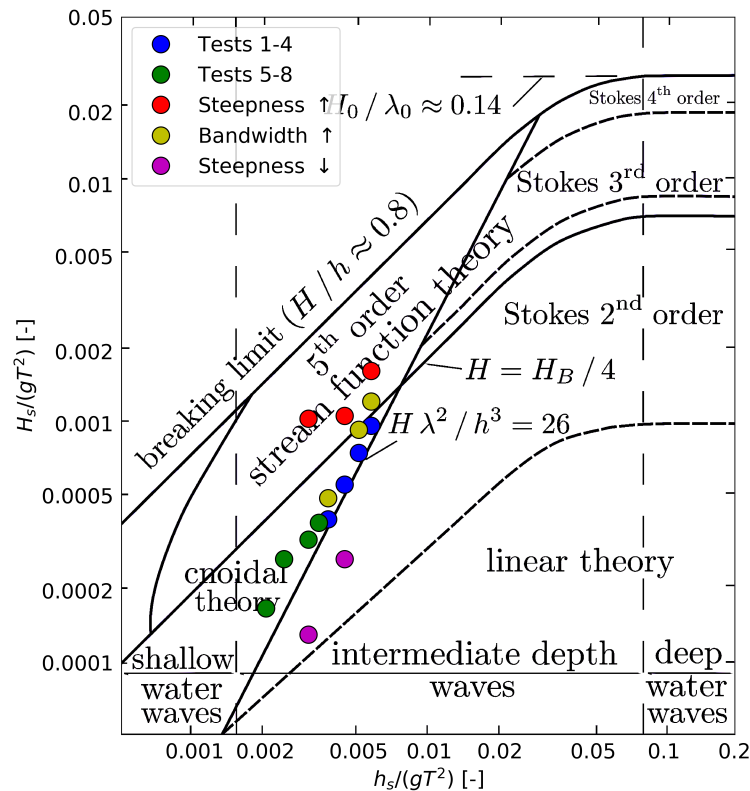
Figure 6.10: Limits of several wave theories. H_s is the calculated H_{m0} of the waves at WG1. In blue the basis test 1-4 and in green the basis tests 5-8 are plotted. In red and purple the tests with an increase and decrease in steepness are plotted respectively. In yellow the tests with an increase in bandwidth are plotted.

Since the considered theoretical framework is said to be valid up to Stokes second-order theory, it must be taken into account that the results of the tests that exceed this limit will probably not or poorly fit the predicted course of the kurtosis in space. This is, because the kurtosis, vertical deviation from a normally distributed sea, can differ for different wave theories. This can clearly be seen in the left plot of figure 6.6.

6.4 Energy density beating

As mentioned in section 6.1 the grassy (and averaged) spectra show a distinct energy beating. Figure 6.11 shows the amplitude spectra of the measured (real) $\eta_{pad,m}$ and calculated $\eta_{pad,f}$ paddle movement. It can be observed that the beating is not present in the calculated paddle movement but ís present in the actual paddle motion. This difference can be explained by the active reflection compensation (ARC), which reacts on reflections in the flume and is therefore not included in the calculated paddle movement file. To ensure that the beating in the wave spectra is indeed caused by reflections, a resonance check is done for the low frequencies (long waves). It is assumed that the outcome of this (simplified) check also applies to the higher frequencies. The resonance check is based on the principle that at a fully reflective boundary (in this case the gravel beach as the slope of the beach approaches a wall for these long waves and the wave paddle) the surface elevation reaches its maximum and velocity goes to zero. The resonant wave length (L_{res}) can therefore be calculated using equation 6.2 with L_{basin} the length between two vertical walls and n the considered mode. The resonant frequency (f_{res}) for long waves can hereafter be calculated using equation 6.3 with h the water depth (in this case averaged between the ratio of deep and shallow water depth) and g the gravitational acceleration. Following the described principle, the ARC should operate at its maximum at these resonant frequencies and should thus correspond with the beating. It can clearly be observed in figure 6.11 that this is the case. It is therefore concluded that the beating in the wave spectra is due to reflections in the flume.

$$L_{res} = \frac{2L_{basin}}{n} \tag{6.2}$$

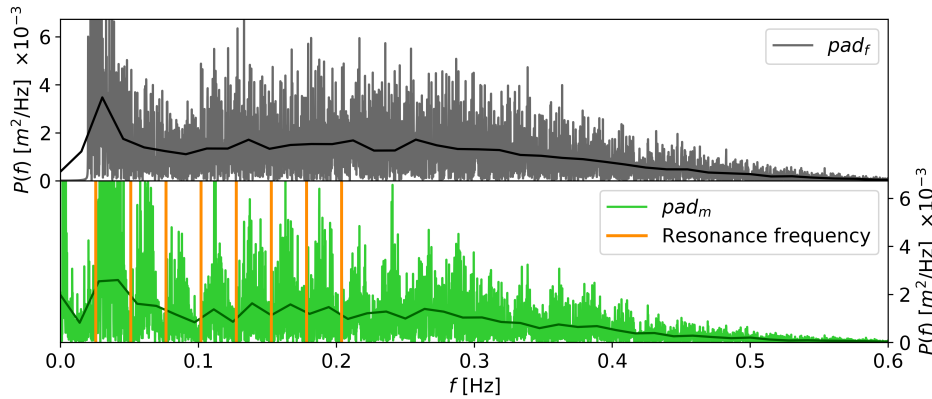$$f_{res} = \frac{\sqrt{gh}}{L_{res}} \tag{6.3}$$

Figure 6.11: Spectra of the measured $\eta_{pad,m}$ and calculated $\eta_{pad,f}$ paddle movement shown in green and grey respectively for test 6. The resonance frequencies are indicated by orange vertical lines.

6.5 Comparison wave gauge and laser scanner measurements

In this section the first 15 minutes of the wave gauge and laser scanner data of one of the tests, specifically test 1a, is analysed. During this test the angular frequency and sampling frequency was set at $\alpha = 0.667$ rad/s and $f_s = 50$ Hz respectively. It is assumed that the conclusions drawn in this section for these laser settings also correspond with the settings $\alpha = 0.1667°$ and $f_s = 25$ Hz used in several other tests. A total range of 20

meters (X = -10 till X = 10 m) is analysed as measurements at a larger distance are thought to be out of the measuring limits of the laser scanner.

First it is assessed whether the Received Signal Strength Indicator (RSSI) values are sufficient. The RSSI is a measure for the power received by the sensor. The unit of the RSSI is arbitrary and has a logarithmic characteristic. Valid measurements are obtained for RSSI values between 1 and 255 (SICK AG, 2017). It has been noticed that for high RSSI values the "noise"/errors in the measurements (which can be seen clearly in the live view function of the SOPAS Engineering Tool) decrease. Figure 6.12 shows the RSSI values of the first 5 seconds of the laser measurements. It can be seen that the RSSI values are sufficient (>0 and <255) for valid distance measurements. In addition it can be seen that the scatter is quite small, which is due to the averaging over time. Last, figure 6.12 shows a distinct trend for X > 0. This trend is thought to be due to the applied (simplified) processing method and needs to be addressed for precise results. It is noted again that in this thesis the laser data is only roughly assessed on its potential for similar or further research and therefore this trend is not further investigated.
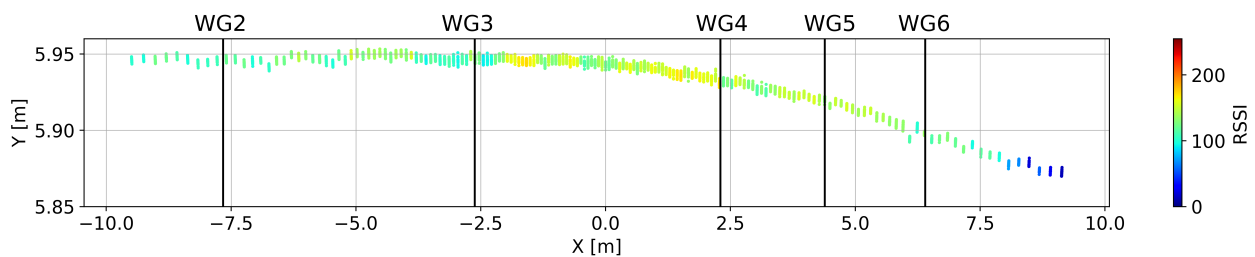
Figure 6.12: The RSSI values of the processed laser scanner measurements across the flume length X, with X = 0 the location of the laser and X ≈ -7.6 the start of the step. The first 5 seconds of test 1a (without wave generation yet) is shown.

The laser scanner surface elevation measurements will be compared to the measurements taken at WG2 (also the location of the start of the step), WG3, WG4, WG5 and WG6. The locations of the considered wave gauges and RSSI values can be observed in figure 6.12. Because the laser scanner and wave gauges were not turned on at the same time, the laser scanner data is "rolled" over time. The amount of measuring points (lag) over which the laser scanner data is rolled is determined by the lag that lead to the highest dimensionless correlation coefficient, ρ. This constant is a measure of how well the signals match. It is thus assumed that the best match results in the correct lag. Figure 6.13 shows the results of the surface elevation η measured by the wave gauges and laser scanner combined.
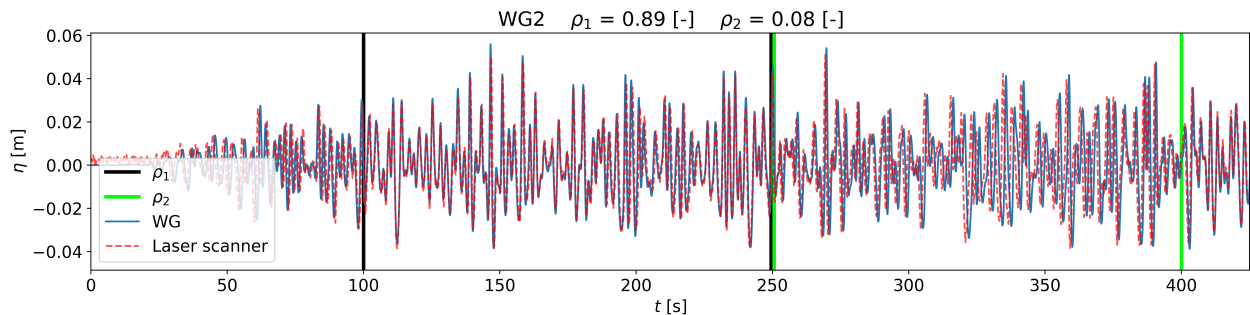

Figure 6.13: Comparison measured surface elevation using the wave gauges (blue solid line) and laser scanner (red dashed line) during the first 7 minutes of test 1a at WG2.

Remarkable is that between t = 100 and t = 250 seconds, the laser scanner and wave gauge data match almost perfectly (ρ_1 = 0.89 [-]) but between t = 250 and t = 400 seconds there seems to be a phase lag which leads to a very low similarity between the signals (ρ_2 = 0.08 [-]). This observation is also made at the other wave gauge locations and this pattern is observed to continue throughout the wave record. The values for the dimensionless correlation coefficients are summarised in table 6.1. From this table it can also be derived that the wave gauges

on the trend line (WG4, WG5 and WG6) show somewhat lower correlation coefficients for t between 100 and 250 seconds. From this analysis it is concluded that the laser scanner shows promising results if the presented issues (trend for $X > 0$ and mixed correlation dependent on t) can be solved with another/improved data processing method.

Correlation coefficient	WG2	WG3	WG4	WG5	WG6
ρ_1 [-] 100 < t < 250 s	0.89	0.87	0.76	0.79	0.78
ρ_2 [-] 100 < t < 250 s	0.08	-0.05	0.04	-0.04	-0.12

Table 6.1: Overview of the dimensionless correlation coefficient between the wave gauges and laser scanner data for 100 < t < 250 and 250 < t < 400 seconds.

In this chapter the results of the experiments are compared to the theoretical framework which is introduced in section 2.5. First the development of the kurtosis in space is assessed. Second, the crest exceedance probability distributions of the test that resembles the North Sea conditions the most is discussed. In addition to the comparison with the model, characteristics of the measured rogue waves are shown to assess possible increased damages to structures or vessels.

7.1 Development of the kurtosis in space

The kurtosis κ is the fourth order moment of the surface elevation η and should be equal to three for a normally distributed sea surface. As explained in section 2.2, the kurtosis is also known as the "tailedness" of a probability density distribution and therefore defines the contribution of large waves in a record. A sea with excess kurtosis ($\kappa > 3$) has therefore more and higher waves and thus a larger probability of occurrence of rogue waves (with rogue waves defined as $H_{max}/H_s > 2$ and/or $\eta_c/H_s > 1.25$). Visualising the development of the kurtosis in space (along the length of the flume) is therefore a proper method to assess if the investigated depth transition leads to (more) rogue waves. The theoretical framework or in short model, has been compared with numerical and experimental results for $k_d h_d > 0.57$ and is said to provide an accurate prediction of the development of the kurtosis in space (Li et al., 2020b), see section 2.5.

The results of the relatively shallow water experiments ($k_d h_d < 0.55$) will be split into four subsections. First the tests within the limits of the model are shown. These consist of test 1-4 and test 3b and 6b. Second tests 5-8 within the region of cnoidal wave theory and the tests with an increase in spectral bandwidth (tests 1a, 2a and 4a) are discussed. Third, the results of tests 3a and 6a with an increased steepness governed by 5th order stream function theory are shown. Last, the difference and/or similarities between tests with a step and slope are assessed. All model predictions are obtained using the spectral significant wave height (H_{m0}) derived from the considered wave record at WG1 ($x = -3$ m). The 95% confidence interval of the kurtosis of each wave record is obtained using a bootstrapping method of 1000 samples with a length of approximately 200 waves (10,000 data points). The comparison of the experimental and model results will be based on the following three characteristics. (1) The shape of the development of the kurtosis in space. After some further reading it will become clear that the model predicts a typical shape of the kurtosis in space. (2) The location of the peak kurtosis. At this peak location the probability of occurrence of rogue waves is largest and therefore of interest. (3) The predicted and experimentally derived values of the kurtosis along the flume length. It is assessed for example where, how much and if these values differ. In this chapter only the results of a small selection of tests are shown. The results of all tests can be found in appendix E.

7.1.1 *Results tests within model limits*

Figure 7.1 shows the result of test 2. The results of this test are representative for all tests within the model limits (second-order in steepness and the narrow-bandwidth approximation). These tests include tests 1, 2, 3, 4, 3b and 6b. Figure 7.1 shows that the experimental results follow the distinct predicted model pattern of the kurtosis in space (1). The peak location, however seems to be located somewhat closer to the step than predicted by the model, with the exception of test 3b and 6b (2). It is found for all other tests that this location is 55 till 95% closer to the step using the ratio x_e/x_m with the subscript e denoting the experimental results and m the model prediction. Using figure 7.1 it can be seen that the peak location can be estimated between $x_e/L_{e,s} \approx 1$ till 1.4. With $x_m/L_{m,s} \approx 1.8$ the ratio is found to be 55 till 78%. It must be noted that due to the limited number of wave gauges between $0 < x < 10$ m it is difficult to correctly estimate the experimental peak locations. Consequently an accurate comparison between the peak locations in terms of numbers is nearly impossible and will not be quantified any further. The values of the kurtosis along the flume length are significantly smaller for

$x > 5$ meter for tests 1, 2, 3, 4 and somewhat smaller at all flume locations for tests 3b and 6b (3). Elaborating on the last two tests, 3b and 6b, the theoretical prediction is found to lie within the 95% confidence bounds at almost all locations along the flume. The model prediction therefore matches both these tests quite well.
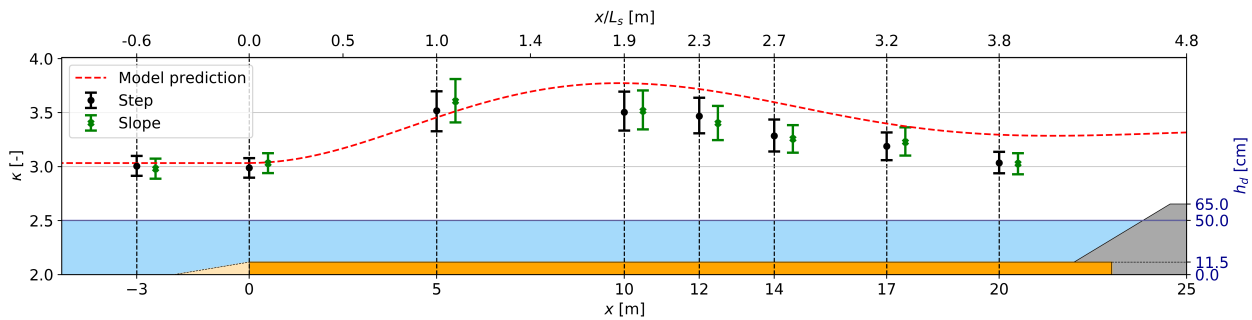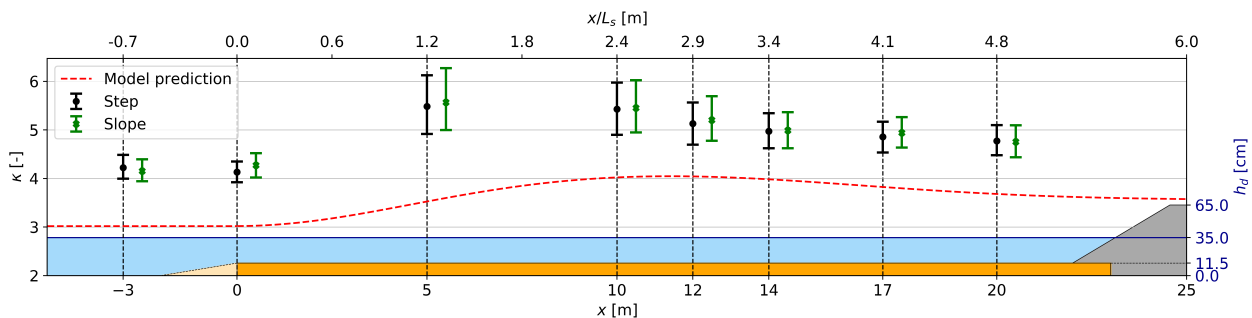

Figure 7.1: Test 2. Development of the kurtosis κ in space. Start of the step at $x = 0$. The 95% confidence bounds of the kurtosis obtained from the experiment are shown in black (step) and green (slope). The model prediction is shown with a red dashed line.

7.1.2 Results tests 5-8 and bandwidth increase

In this section the results of the kurtosis in space of tests 5, 6, 7, 8, 1a, 2a and 4a are discussed. As concluded in chapter 6, the generated waves are governed by cnoidal (tests 5, 6, 7, 8, 2a and 4a) and 5th order stream function theory (test 1a). Figure 7.2 shows the results of test 6 which is representative for all tests discussed in this section. Noticeable is that the distinct shape predicted by the model can be identified in the experimental results (1). The location of the peak kurtosis seems again to be located closer to the step than predicted (2). The difference in peak location (40-70% closer to the step x_e/x_m) for these tests is even more significant than estimated in section 7.1.1. It is however noted again that due to the limited number of wave gauges this quantification is very rough. Figure 7.2 shows that the kurtosis at the start of the test is much higher than predicted. The overall increase in kurtosis however seems to be predicted quite well (3).

Figure 7.2: Test 6. Development of the kurtosis κ in space. Start of the step at $x = 0$. The 95% confidence bounds of the kurtosis obtained from the experiment are shown in black (step) and green (slope). The model prediction is shown with a red dashed line.

7.1.3 Results tests steepness increase

In this section tests 1b, 3a and 6a with a steepness increase are discussed. It is shown in figure 6.10 that these tests are governed by the 5th order stream function theory just as test 1a with a bandwidth increase. The results of these tests however are significantly different from test 1a. Figure 7.3 shows the results of test 3a which is also representative for test 1b. Because during test 6a significant wave breaking occurred (even before the depth transition) these results deviate from the results presented in figure 7.3 and are therefore not discussed any further in this report. Figure 7.3 shows that the experimental results of the kurtosis in space again follows the distinct model shape (1). The peak of the kurtosis also seems to be located closer to the step than predicted

$(x_e/x_m \approx 50\%)$, again noting that due to the limited amount of wave gauges this estimation is very rough (2). For $x > 5$ meter the value of the experimental kurtosis is significantly lower than the predicted kurtosis (3).
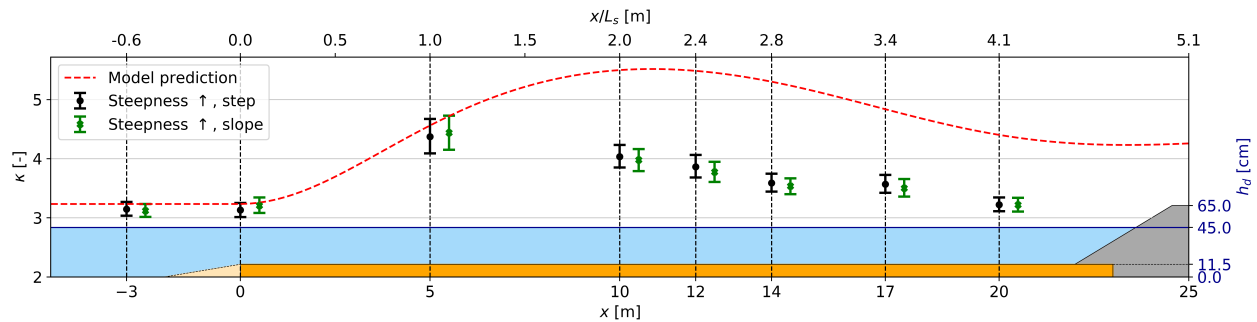

Figure 7.3: Test 3a. Development of the kurtosis κ in space. Start of the step at $x = 0$. The 95% confidence bounds of the kurtosis obtained from the experiment are shown in black (step) and green (slope). The model prediction is shown with a red dashed line.

7.1.4 Comparison tests with a step and slope (1:20)

According to literature, experiments have shown that tests with waves propagating over a gentle depth transition show lower to no peaks in kurtosis in comparison with a steep depth transition (Gramstad et al., 2013; Zheng et al., 2020; Viotti and Dias, 2014; Zeng and Trulsen, 2012). Zheng et al. (2020) found a peak kurtosis of 3.61 and 3.33 for tests with a step and 1:20 slope respectively. Considering the difference in excess kurtosis (0.61 and 0.33), a significant deviation of ±50% is found. The dimensionless water depths in this study are $kh_d = 1.06$ and $kh_s = 0.70$.

Looking at figures 7.1, 7.2 and 7.3 one can observe little to no difference between the (peak) kurtosis of the experiments with a step (black) and slope (green). This therefore seems not to be in accordance with recent (relatively deep water) studies discussed in the previous paragraph. As the "actual" slope depends on the wave length, the contribution of the sub- and super-harmonics is assessed. This is important as for relatively long waves, thus the sub-harmonic components, the slope approaches a wall. This would therefore explain that the slope provides the same results as the step (wall). If however the super-harmonics are governing, the slope is gentle and should consequently result in a smaller excess kurtosis with respect to a step.

Separating the sub- and super-harmonic prediction of the kurtosis in the statistical model ($\zeta^{(1)} + \zeta^{(20)}$ and $\zeta^{(1)} + \zeta^{(22)}$), it is found that for both relatively shallow ($kh < 0.5$) and deep ($kh > 0.5$) water conditions the super-harmonics provide the largest contribution to the total excess kurtosis. However, as also the interaction between the components is important to predict the increase in kurtosis, it is questioned if this method is sufficient. To ensure that indeed the super-harmonic components are governing, the kurtosis of the experimental data with a low-pass filter set at 1 Hz is calculated. The result is a relatively small excess kurtosis with respect to the total excess kurtosis. This leads to the conclusion that the contribution of the super-harmonics is indeed governing. Following, using the definition by Iribarren, the slope is relatively gentle considering the super-harmonics ($f > 1$ Hz) (Bosboom and Stive, 2012). Concluding, the results are in contrast to the previously described relatively deep water literature. The results do however support the conclusion drawn by Sergeeva et al. (2011) that found that the length of the transitional zone (thus steepness of the depth transition) does not influence the (excess) kurtosis. The considered slopes in this research are 1:60, 1:120 and 1:240 and kurtosis was found to increase from ±3 to ±6. If one observes figure 2.5, it can be seen that this numerical research also studied the relatively shallow water region $kh < 0.5$. It can therefore be concluded that the influence of slope seems to be different for relatively deep and relatively shallow water conditions. More specifically, the influence of slope seems to be negligible for $kh < 0.5$. However, it must be kept in mind that the study by Sergeeva et al. (2011) did not include an infinite slope (step) for comparison.

7.2 Crest exceedance probability at North Sea location

As discussed in the previous section, (excess) kurtosis is a measure for the probability of occurrence of rogue waves. Also, a stationary Gaussian record of a wind sea is according to short term statistics described by the linear model and the crest and wave height are therefore Rayleigh distributed (Holthuijsen, 2007). To visually assess the increase in probability of occurrence of rogue waves due to the depth transition, the exceedance probability of occurrence of the crest heights, determined by a down zero-crossing analysis, is plotted. Figure 7.4 shows the results of basis test 4 with slope. This test approaches a stationary Gaussian sea and resembles the dimensionless water depth, and thus bathymetry and wave period, of the measured North Sea conditions best. (Test 5, which is the best match considering the scaled bathymetry, is not discussed in this section as the wave field before the step is non-Gaussian due to incorrect paddle movement.)

(a) $x = -3$ m   (b) $x = 5$ m   (c) $x = 10$ m   (d) $x = 17$ m
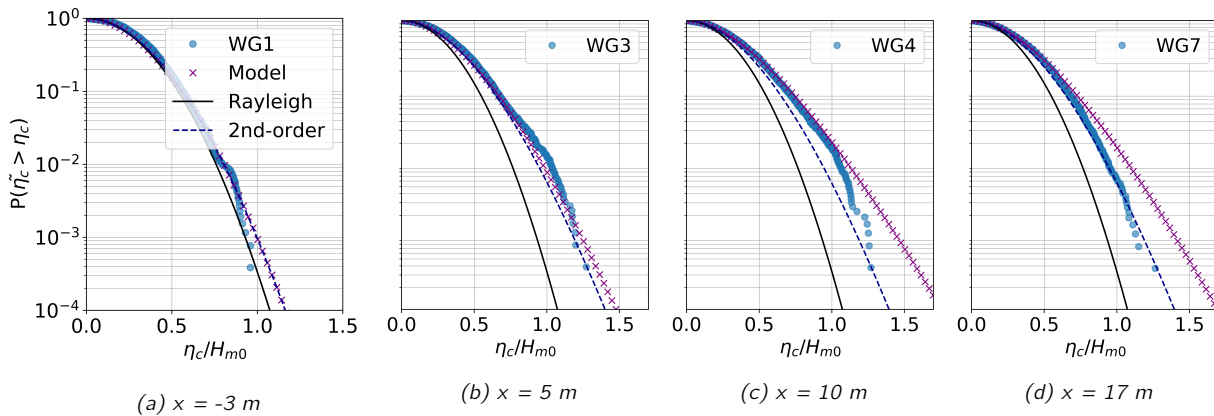
Figure 7.4: Test 4 with slope 1:20. Exceedance probability density distribution of the wave crest η_c at WG1, WG3, WG4 and WG7. The Rayleigh distribution is plotted with a solid black line and the distribution following standard second-order theory is plotted with a blue dashed line. For the left plot, WG1, $x < 0$, $h = h_d$ and for all other plots $x > 0$, $h = h_s$. The model prediction is plotted using purple crosses and the experimental results are shown in blue circles.

Figure 7.4a shows that the crest exceedance probability density distribution (PDF) of the experiments matches the Rayleigh distribution. This result is just as expected, because the first wave gauge is located before the step and the wave field at this location should thus be described by the Rayleigh distribution. Figure 7.4b shows that the experimental results match the model quite well. This is in accordance with the results of the kurtosis in space as the model and experimental results also match at this wave gauge. The results of figures 7.4c and 7.4d in comparison with the model are therefore also as expected, because the model overestimated the kurtosis of the experimental results at these locations. It can clearly be observed in figure 7.4 that the probability of exceedance is larger than the Rayleigh prediction at all locations behind the step. It can also be observed that the distribution following standard second-order theory (including the bound wave components but neglecting the free waves), matches the results down wave of the step quite well. Figure 7.4b shows the largest deviation from Rayleigh and second-order statistics, which is, according to the mechanism, due to the interaction of the wve field with the generated free second-order waves. Figure 7.4d shows that the wave field shifts to its new equilibrium (governed by second-order theory).

In addition, the wave height with a 0.1% exceedance probability ($H_{0.1\%}$) following linear theory can be read from figure 7.4 at $P = 10^{-3}$ (using the estimation that $2\eta = H$) or can be calculated using equation 2.7. It is found that $H_{0.1\%} = 1.86\,H_s$. Analysing the experimental data of test 4 with slope at WG4, a wave height, following a zero-crossing analysis, of $H_{0.1\%} \approx 1.87 H_s$ is found, which is similar to the Rayleigh prediction. Apparently, the crests are significantly larger (abnormal) than predicted by the linear model, but the troughs are smaller (high peaks, shallow troughs). This means that the wave heights of this test roughly follow linear theory, but the crest heights significantly deviate.

7.3 Characteristics of the measured rogue waves

This chapter concludes with a brief time series analysis of the measured rogue waves in the flume. Possible damages on structures, such as wind turbines and vessels, do not only depend on the frequency and height of extreme waves but also on their slamming impacts (or also-called wave impact, dynamic loads and wave shock) and steepness. To quantify and assess these possible damages, a thorough analysis of the field data collected by the RVO measurement campaign would be a good addition. However, as this data is to be released, only a concise analysis of the (increased) steepness for basis test 4 with a slope of 1:20 is performed. This test is most representative for the scaled North Sea conditions as shown in figure 1.6 and is governed by a Gaussian stationary sea.

Figure 7.5 shows a short realisation of the total time series of test 4 with slope 1:20. In this figure one of the two rogue waves ($H_{max}/H_{m0} = 2.02$) that is found in the wave record is shown using a dark blue color. The period of the wave is found to be 2.72 seconds and is therefore slightly less than the peak period. The crest height is found to equal 3.8 centimeters and preceding trough 2.6 centimeters. The total wave height equals therefore 6.4 centimeters. The average steepness of the rogue wave is 0.045 ($kH_{max}/2$) while the steepness using the significant wave height "only" equals 0.022 ($kH_{m0}/2$) with the wave number determined using the rogue and peak period respectively.
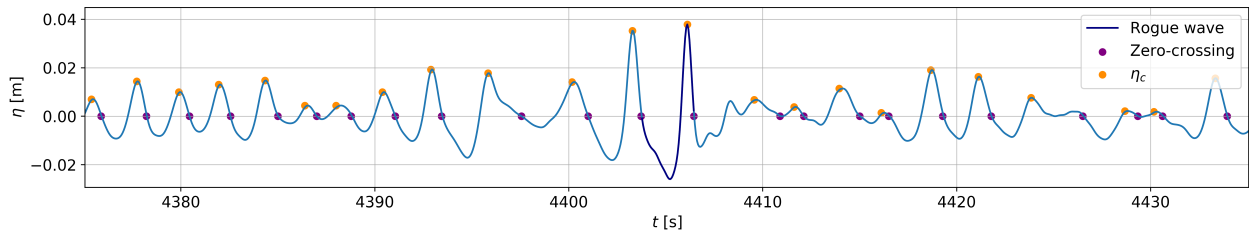
Figure 7.5: Test 4 with slope 1:20. Time series of the surface elevation between t = 4375 and 4435 seconds (±73 minutes). The zero-crossings are shown with blue dots and the crest heights are shown in orange. A dark blue line at the center of the plot represents one of the two rogue waves ($H_{max}/H_{m0} = 2.02$) in this record.

Because the generated waves for the considered basis test 4 are on the limits of Stokes second-order theory, the waves are relatively gentle ($H_{m0}/L_{0,p} = s_{0,p} \approx 0.0026$, $H_{max}/L_{0,p} = s_{0,p,max} \approx 0.0052$) in comparison with "normal" wind sea ($s_{0,p} \approx 0.04$). The increased steepness is therefore remarkable and indicates possible increased damages to structures and vessels but cannot be quantified any further. As also mentioned in the beginning of this section, the analysis of field data is therefore considered to be a good method to derive relevant wave characteristics to assess possible increased damages.

<div style="text-align: right; font-size: 3em;">8</div>

Discussion, conclusions and recommendations

In this chapter the results of the literature review and the experimental study will be used to answer the stated research questions presented in chapter 1. First, each research question is discussed. Hereafter, conclusions are drawn. This chapter concludes with recommendations for further research.

8.1 Discussion

1. Is there existing evidence of rogue wave occurrence in the North Sea?

Providing an unambiguous answer to this sub-question is nearly impossible. This is because three definitions of a rogue (abnormal) wave can be distinguished. First, the thrilling definition, which consist of stories, photographs and videos of huge waves. Second, the use of the rogue wave criteria. These criteria classify a wave as rogue when $H/H_s > 2$ and/or $\eta_c/H_s > 1.25$ and therefore describes their unexpected height in comparison with the total wave record. And last, the definition that rogues are statistically abnormal waves in comparison with the generally applied linear model. Below, all three definitions are discussed in the context of the North Sea.

Considering the first definition, it must be questioned whether this is a proper method to identify abnormal, rogue waves. This is because it is likely that sailors' tales are exaggerated and it is possible that photographs are taken from a certain angle that distorts the size of the wave. Furthermore, the definition lacks quantification, for some people a huge wave could be seen as abnormal, while others could classify it as just a large wave. One "thrilling" story in 1984 involving the North Sea and a wave with an estimated crest height of 20 meters, however, also included damage to one of the control rooms at an offshore platform as physical evidence. Concluding, as the first definition is questioned as a proper method to define a rogue wave and knowing the observed damage to the platform, it is at least certain that an enormous wave occurred in the North Sea.

The second definition, using the rogue wave criteria to define a rogue wave, is commonly applied in literature. It is however shown in section 2.1.1, that if one waits long enough, it is almost certain that a rogue wave $H/H_s > 2$ will occur. It must therefore be questioned if these criteria actually describe abnormal, rogue, waves. In the context of the North Sea, and according to these criteria, several rogue waves have been measured. More specifically, the world famous "Draupner" event, which lead to the interest of scientists in this topic, was measured by the Statoil platform Draupner E located in the North Sea.

Considering the definition of rogue waves as statically abnormal, several authors stress the fact that even the use of enormous data sets results in the analysis of a small number of "rogue" waves. It is therefore difficult to statistically conclude whether the rogue waves are just rare realisations of typical distributions or actually statistically abnormal. Guedes Soares et al. (2003) identified 23 rogue waves (using the rogue wave criteria) in storm records measured at the North Alwyn oil and gas platform containing a total of 55 thousand waves. Consequently they conclude that rogue waves are not that rare. On the contrary, Olagnon and Iseghem (2000) concluded, using a dataset of 1.6 million waves measured at the Frigg platform, that the measured extreme waves did not deviate from the expected distribution. Although it was noted that this is difficult to asses using field data because of the limited number of extremes, no abnormal/rogue waves were identified. A recent study by Teutsch et al. (2020) that used a huge data set of 329 million waves collected by wave buoys and radar stations found that besides the radar stations one wave buoy near a "strongly structured bathymetry with strong gradients" showed deviation from the expected statistical distribution. This indicates that at some locations rogue waves are more likely to occur due to the local metocean conditions. Examples of metocean conditions include local bathymetry and tidal currents. This author also addressed the issue of the limited number of extreme waves to identify whether these waves are actually rogue or just rare realisations of a typical distribution

and thus *not* statistically abnormal. Similar to Olagnon and Iseghem (2000), Teutsch et al. (2020) concluded that "rogue" waves "may simply represent rare realizations from typical distributions".

2. What are the simplifications and limitations of the physical model that is scaled to a potential rogue wave event in the North Sea?

The discussion of this research sub-question is split into two sections; wave conditions and bathymetry.

Wave conditions

In this thesis the long wave field some minutes prior to the potential rogue wave event (figure 1.6) measured during the RVO data campaign by buoy HKWA located 52°34'N 3°43'E is scaled. The physical model is designed for the flume at the Hydraulic Engineering laboratory of the Delft University of Technology and is therefore 2D. This means that only one-directional waves are considered. In real sea waves travel in a range of directions. Ducrozet and Gouin (2017) stressed that for a precise prediction of rogue wave occurrence one must include directional effects. It is therefore important that simplification is noted.

Furthermore, wave conditions in the North Sea are assumed to be described best by a JONSWAP-spectrum. This idealised spectrum describes fetch-limited deep water waves based on measurements in the North Sea. The simplified wave conditions in the flume are described by a Gaussian wave spectrum. Using this spectrum the influence of spectral parameters such as spectral bandwidth can be assessed more easily in comparison with the theoretical framework. JONSWAP-spectra assign more energy density to the frequencies higher than the peak frequency in comparison with the Gaussian spectra where energy density is equal at both sides of the peak frequency. A difference in results using the two spectra is considered negligible for tests with relatively narrow-banded Gaussian spectra. Possible differences in results (between prototype and model) must be considered for test results with broad banded spectra as these spectra show significant difference in the low-frequency region. Because the results of both narrow- and broad-banded spectra show an increase in kurtosis (which is relevant to the main research question), this simplification is considered irrelevant to the answer of the main research question. It is however still an important simplification to keep in mind.

A limitation of the experiments following the potential rogue wave as the basis for scaling, is the derived peak period. The prototype wave period is estimated by taking the average (long) wave period a few minutes prior to the considered event. This wave period is found to be 25 seconds. Including the bathymetry of the North Sea (30 meters depth) this results in relatively shallow water conditions ($k_d h_d = 0.45$). The experimental results therefore directly contribute to the knowledge gap in current literature as this generally considers relatively deep water conditions. The limitation however is the direct application to the North Sea. Typical regular and storm Dutch North Sea conditions describe a peak period of 7 and 12 seconds respectively (Bosboom and Stive, 2012; Paulsen et al., 2019), which means that North Sea peak wave periods are significantly smaller than the experimental wave period (relatively deep water conditions $kh>1$). However, as waves with a period of 25 seconds were actually measured (figure 1.6) in the North Sea, the experimental results can still be applicable for part of a North Sea wave record. Following, it must be questioned whether a long wave peak period is actually common at the Dutch North Sea, how often this period occurs, if there is a (additional/rogue wave) mechanism that increased the wave period or if the long waves are a data processing artefact. The first suggestion is insofar unlikely that this suggestion is rejected. Wave fields in the North Sea are simply not described by a peak period of 25 seconds. The second suggestion is of importance as an irregular sea includes a whole range of periods. Namely, waves do not only occur with a peak wave period of, for example, 7 seconds but also with a shorter and longer period of, for example, 3 and 10 seconds. This range in wave periods should be investigated using the data collected by the RVO and is of importance to assess in what capacity the experimental results can be applied to the North Sea. This is further discussed in the section of the main research question. Considering the third suggestion, in this thesis only the effects of bottom topography (which results in some cases in an increase in kurtosis) is researched. It is possible that other (un)known mechanisms exist that cause a significant increase in the peak wave period (due to the depth transition or another trigger). The last suggestion, whether the long waves are a processing artefact, is also probable but cannot be assessed as the field data has yet to be released. The use of the experimental data to answer the main research question therefore depends on the results of a field data analysis. This is taken into account in the conclusions section.

Bathymetry

The wave buoy that measured the potential rogue wave event is located in the vicinity of a large morphological feature, so-called sand ridge, of approximately 2.5 kilometers length, 8 meters height at a depth of 30 meters. Because this bell shaped sand ridge (figure 3.1) is impractical to model in the flume, the bathymetry is simplified to a continuous rectangle. To approach the slope of the sand ridge (1:200), a slope of 1:20 is attached to the rectangular model bathymetry for a number of tests. The effect of this simplified ridge shape, specifically shortening the slope, cannot be neglected as recent literature has addressed that this can have significant influence on the kurtosis (and thus probability of occurrence of rogue waves) (Gramstad et al., 2013; Zheng et al., 2020; Viotti and Dias, 2014; Zeng and Trulsen, 2012). This simplification is further addressed in the discussion of the main research question. In addition, if one observes the local bathymetry (figure 3.1), besides the large bell-shaped sand ridge, smaller features (small sand waves) can be identified in the cross-section. As the effects of these small features are still unknown, it is an important simplification to note.

The applied scaling of the bathymetry based on the buoy's location also brings up a limitation of the experiments. In the North Sea several sand ridges in different shapes are present. If the features are all significantly different the results with the applied scaling of $n_F = 1/80$ cannot easily be applied to the whole Dutch North Sea. However, using the bathymetry viewing tool provided by EMODnet (2020) one can observe that the sand ridges at the West coast are of the same order (±10 meters) and have the approximate same length (2-5 kilometers). However, also some exceptions are present, such a a sand ridge West of IJmuiden (52°39' N, 3°19' E) which has a height of 20 meters and length of approximately 3 kilometers. The features at the North (North of the Wadden Sea) are also somewhat different as their heights are significantly smaller (<4 meters). Another limitation is that just one cross-section of the sand ridge is modelled in the flume. The sand ridge is of course 3D, which means that if the wave direction differs, the cross-section (in the direction of the waves) changes.

3. Can an existing model based on narrow-banded second-order theory explain laboratory observations?

a) For typical North Sea wave periods

Recent literature, considering relatively deep water conditions, has shown that an increase in kurtosis (and thus probability of occurrence of rogue waves) is expected for wave fields propagating over a depth transition. In this thesis a statistical model (theoretical framework) valid up to second-order in steepness and narrow-banded wave fields is elaborated and, using the experimental data, evaluated for relatively shallow water conditions. The framework neglects the effects of viscosity, density differences, evanescent waves and surface tension. The proposed mechanism explains an increase in the probability of occurrence of rogue waves due to the presence of a depth transition (step, infinite slope). It is suggested that the depth transition generates free counterparts of the bound sub- and super-harmonic components. As these free components travel at different speeds peaks are localised and an increase in wave heights and thus kurtosis is expected. Fully non-linear numerical simulations and physical model tests have validated the model prediction for $0.57 < kh < 1.6$. This means that the development of the kurtosis and skewness in space, including the peak location and magnitude, are predicted accurately for these dimensionless depths (Li et al., 2020b). Deviations from the model are most pronounced for the deepest case where it is assumed that third-order effects play a significant role.

Considering regular North Sea conditions with $H_s = 1.5$ meters, $T_p = 7$ seconds (Bosboom and Stive, 2012), $h_d = 30$ m and $h_s = 22$ m, dimensionless water depths of $k_p h_d = 2.5$ and $k_p h_s = 1.9$ (with k_p the wave number following the peak wave period) are found. Using these parameters and a spectral bandwidth of 0.15 [-], the statistical model predicts a peak kurtosis of only 3.0133 [-]. The excess kurtosis, meaning the deviation from the linear model, is therefore only 0.0133 [-]. It must be noted that this prediction could deviate as higher-order effects are not included but are considered significant according to Li et al. (2020b). Using the results of a physical experiment, with somewhat similar conditions, analysed by Trulsen et al. (2020) that has shown no/negligible increase in kurtosis for $k_p h_d = 4.9$ and $k_p h_s = 1.6$, it can be concluded that the excess kurtosis including higher-order effects is still expected to be small ($\ll 0.1$). Concluding, the model prediction does not explain the higher-order effects which are expected to occur for regular North Sea conditions, but its prediction in kurtosis is assumed to be in the approximate same order. An important model assumption that must also be

discussed is the assumed infinite slope (step) of the depth transition. The sand ridge in the North Sea has a gentle slope of 1:200. This is considerably different from the model step. As the slope of the depth transition has a significant impact on the peak kurtosis, this simplification must be taken into account in the discussion and conclusion on the main research question (Gramstad et al., 2013; Zheng et al., 2020; Viotti and Dias, 2014; Zeng and Trulsen, 2012). Considering North Sea storm conditions; H_s = 9 meters, T_p = 12 seconds (Paulsen et al., 2019), h_d = 30 m and h_s = 22 m, dimensionless water depths of $k_p h_d$ = 1.06 and $k_p h_s$ = 0.87 are found. As these conditions are well within the validated range of the statistical model, it is assumed that the model explains the mechanism for storm wave conditions accurately. With a bandwidth of 0.15 [-] a peak kurtosis of 4.133 is predicted. Noting again that the influence of slope is not taken into account in this prediction. Last, it must be noted that an irregular sea includes a range of wave periods. To obtain a proper prediction for the North Sea, a whole range of existing wave periods (and heights) must be considered. This range in wave periods should be analysed using the field data collected by the RVO measurement campaign. Also, in this model directional effects are excluded. Again, Ducrozet and Gouin (2017) stressed that for a precise prediction of rogue wave occurrence one must include directional effects.

b) For long wave periods

To provide an answer to this research question, physical experiments have been performed in the Hydraulic Engineering laboratory at the Delft University of Technology and its results are analysed and compared to the statistical model. This model is introduced in section 2.5 and summarised in the discussion presented in question 3a.

The experiments in this thesis were performed in the range of $0.29 < kh < 0.56$ and are thus in a significantly shallower regime than current relatively deep water literature ($kh > 0.5$). To assess if the existing statistical model explains the laboratory observations, three characteristics of the measured and predicted kurtosis in space are compared: (1) the shape of the development of the kurtosis in space. (2) The peak location. (3) The values of the kurtosis along the flume length. These three characteristics in comparison with the laboratory results are further discussed below.

(1) The experimental results have shown that the distinct shape of the kurtosis in space can be identified in all tests (except for test 6a; with a steepness increase, where continuous wave breaking took place). Remarkable is therefore that even tests outside the second-order limit also show the predicted shape. (2) The kurtosis peak location using the experimental data is found to be located somewhat closer to the step than predicted by the model, with the exception of tests 3b and 6b; tests with a relatively low steepness. Due to the limited number of wave gauges it is however not possible to accurately quantify how much the experimental peak location is closer to the step. It is estimated that the ratio (defined as x_e/x_m with x_e and x_m the experimentally estimated and model peak locations respectively) lies between 55 till 95% for tests 1, 2, 3 and 4. (3) The overall value of the kurtosis at $x > 5$ m is significantly over predicted for tests 1, 2, 3 and 4 which lie on the second-order in steepness model limits and tests 1b and 3a, which are tests with a steepness increase. The prediction of the kurtosis is significantly under predicted by the model for tests with a relatively broad spectrum (tests 5, 6, 7, 8, 1a, 2a and 4a). This deviation between experiments and the model is hypothesised to be due to violation of the narrow-bandwidth assumption and/or its higher order non-linearity. On the contrary, the steepness decrease tests, 3b and 6b, which are well within the second-order in steepness limits, are predicted quite well considering all three characteristics. Namely, the theoretical prediction at almost locations along the flume lies within the 95% confidence bounds and the peak location seems not to be located closer or further away from the step. It is therefore questioned if tests 1, 2, 3 and 4 are considered correctly as tests within the model limits, because these tests actually lie on/just outside the Stokes second-order theory validity region and show significant deviation of the kurtosis at $x > 5$ m and peak location (see figure 6.10). Furthermore, as test 6b is described by a broad spectral bandwidth and is predicted quite well by the statistical model, it is reasoned that observed deviations during other tests are (mostly) due to higher order non-linearity and thus not due to hypothesised violation of the narrow-bandwidth assumption.

Can rogue waves arise as a result of the local bottom topography at the location of future offshore wind farms along the Dutch coast?

To answer the main research question the results of the physical experiments, model predictions and relevant literature are combined. Also, relevant identified simplifications and limitations of the physical and statistical model are taken into account and discussed. An answer will be provided for both North Sea regular ($k_p h_d = 2.5$, $k_p h_s = 1.9$), and storm ($k_p h_d = 1.06$, $k_p h_s = 0.87$) wave conditions.

The discussion of the third research sub-question has shown that an excess kurtosis of 0.0133 [-] and 1.133 [-] is expected for a representative peak wave period of 7 and 12 seconds and wave height of 1.5 and 9 meters for regular and storm wave conditions respectively using the statistical model developed by Li et al. (2020b). It is also shown that a significant excess kurtosis (>0.2 [-]) is expected for the relatively shallow water experiments and thus long waves ($T = 25$ s). An important limitation of the statistical model which will be discussed is the assumed infinite slope of the depth transition. Recent literature has shown that tests with waves propagating over a gentle depth transition show lower to no peaks in kurtosis in comparison with a steep depth transition (Gramstad et al., 2013; Zheng et al., 2020; Viotti and Dias, 2014; Zeng and Trulsen, 2012). Zheng et al. (2020) found for experiments with $kh_d = 1.06$ and $kh_s = 0.70$ (which is very similar to North Sea storm conditions with a peak period of 12 seconds) that the excess kurtosis decreased with a factor two for a slope of 1:20 and factor ten for a slope of 1:80. This would reduce the predicted excess kurtosis to 0.0013 [-] and 0.113[-] for a slope of 1:80 and regular and storm wave conditions respectively. In addition, as the slope of the considered sand ridge is 1:200 and therefore even more gentle than 1:80, it is expected that the reduction factor is even larger. On the contrary to these observations in relatively deep water literature, the physical experiments performed in this thesis have shown no to little deviation between the (excess) kurtosis for a step and a 1:20 slope. It is found that this observation is in accordance with the relatively shallow water numerical study by Sergeeva et al. (2011). This study investigated slopes up to 1:240 and concluded that the statistical parameters are independent of the transitional length and similarly thus the slope. It can therefore be concluded that for relatively deep water conditions the local slope of 1:200 reduces the peak kurtosis significantly and for relatively shallow water conditions the influence of slope is negligible.

Another important and relevant simplification of the model is the use of a single wave period for the prediction of the kurtosis. An irregular sea does not only consist of waves from a range of directions but also of waves from a range of wave periods. Also, for each prediction one significant wave height is considered. According to the model, underestimation of this wave height leads to underestimation of the peak kurtosis. Considering regular North Sea conditions, changing the wave height and wave period to 3 meters and 10 seconds respectively results in a peak excess kurtosis of 0.921 [-] (with the influence of slope this excess kurtosis is only < 0.0921 [-]). This excess kurtosis is significantly larger than 0.0133[-] and stresses the importance of a thorough field data analysis. Furthermore, the range of wave periods is also important as the experiments have shown that the long wave ($T = 25$ s) tests show a significant peak kurtosis ánd are not influenced by the slope. One can imagine that a (storm) wave field with a peak period of 12 seconds could contain waves with a period of 25 seconds. In that case, for that part of the wave record, the excess kurtosis is estimated to be significant and is not reduced by the influence of slope. Consequently, for the long waves, it can be concluded that the bathymetry in the North Sea can trigger rogue waves. The questions which are brought up in the second research sub-question; is a long wave peak period actually common at the Dutch North Sea, how often does this period occur, is there a (additional/rogue wave) mechanism that increased the wave period or is the long wave period a data processing artefact, are therefore very relevant but remain to be unanswered. This is because the field data has yet to be released and analysed. Considering regular North Sea conditions with a peak period of 7 seconds, long waves are thought to be less likely to occur and it is therefore concluded that no significant excess kurtosis is expected (predicted excess kurtosis reduced with a factor 10 is negligible).

An important point of discussion which remains unanswered is the (exact) quantitative effects of the physical and statistical model simplifications such as the use of one-directional waves, a Gaussian wave spectrum, one cross-section and a "smooth" bathymetry (not including the smaller features).

8.2 Conclusions

The objective of this thesis was to investigate whether there is a higher probability of occurrence of rogue waves atop depth transitions for a relatively shallow environment ($kh < 0.5$) and if this increased probability is expected in the Dutch North Sea. To achieve this objective, flume experiments have been performed at the Hydraulic Engineering laboratory of the Delft University of Technology. The experiments have been scaled using the long waves some minutes prior to a potential rogue wave measured during a RVO data campaign for sustainable wind energy (figure 1.6). The obtained experimental data is used as a comparison to an existing theoretical model, validated for a relatively deep regime ($kh \approx 1$), that describes a potential rogue wave mechanism induced by depth transitions. The results of the (relatively shallow water) experiments, the predictions of the theoretical model and relevant literature are combined in order to give achieve this thesis' objective. The conclusions of this thesis are listed below.

- According to several authors that analysed large sets of field data, the question whether statistically abnormal (rogue) waves exist still remains under debate.

- Using data from the physical experiment performed at the Hydraulic Engineering laboratory of the Delft University of Technology, it is shown that for relatively shallow water conditions ($kh < 0.5$) the increase in kurtosis for a step and 1:20 slope are equal. The results are therefore not in accordance with observations made in relatively deep water studies, where it is shown that gentler slopes show a reduced increase in kurtosis.

- It is found that test results within the limits of Stokes second-order theory can be described by a rogue wave mechanism proposed by Li et al. (2020b). This mechanism explains the increased kurtosis as the interaction between the transmitted wave field and second-order components: the free sub- and super-harmonic components generated by the depth transition. Figure 8.1 gives an overview of the prediction of the peak kurtosis due to a depth transition as a function of h_s/h_d and $k_{0d}h_d$ for $\delta = 0.15$ [-], $\epsilon_d = 0.01$ and $0.44 < k_{0d}h_d < 1.6$. This figure corresponds with the validated range of the framework, thus the lower limits of the experiments in this thesis that are within the limits of Stokes second-order theory and upper limits as found by Li et al. (2020b). It must be noted that for different spectral bandwidth and wave steepness the figure changes. Increasing the wave steepness results in more realistic predictions for the relatively deep water region but exceedance of the model limits in the relatively shallow water region.
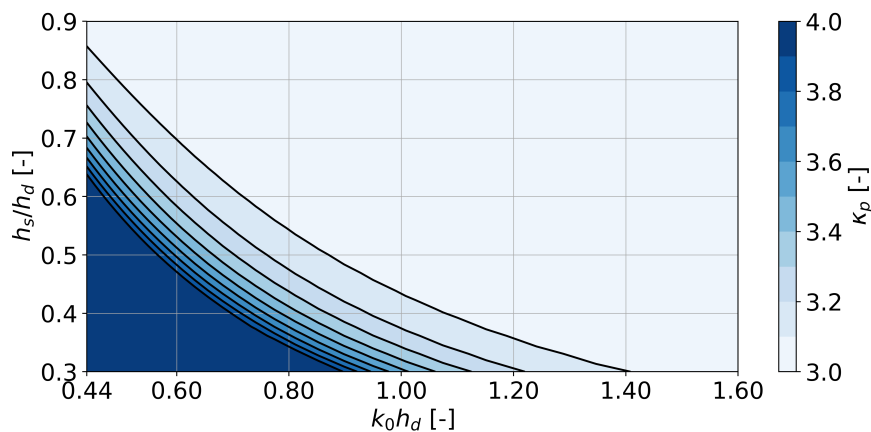
Figure 8.1: Statistical model prediction by Li et al. (2020b) of peak kurtosis κ_p as a function of h_s/h_d and $k_{0d}h_d$ for $\delta = 0.15$ [-] and $\epsilon_d = 0.01$. For this prediction, the slope of the depth transition is assumed infinite (step). An increase in steepness results in an increase in peak kurtosis (contours moving towards the right of the figure). It must be noted that increased steepness results in (increased) exceedance of the second-order limit of the model in the low $k_{0d}h_d$ region.

- It is found that test results on or beyond the Stokes second-order limit show deviation from the predicted kurtosis peak location and values of the kurtosis using the statistical model proposed by Li et al. (2020b). The distinct shape of the predicted kurtosis in space can however be found in all tests results. It is therefore concluded that for these tests the model partly explains the experimental results but lacks the inclusion of increased non-linearity and therefore the effects of higher-order components.

- Considering regular North Sea conditions, H_s = 1.5 m, T_p = 7 s (Bosboom and Stive, 2012), h_d = 30 m and h_s = 22 m, $k_p h_d$ = 2.5 and $k_p h_s$ = 1.9, no increase in the probability of occurrence of rogue waves is expected. The predicted excess kurtosis (including a range of wave periods and wave heights) in combination with the influence of slope (reducing the excess kurtosis with at least a factor 10), is considered negligible.

- Considering North Sea storm conditions, H_s = 9 m, T_p = 12 s (Paulsen et al., 2019), h_d = 30 m and h_s = 22 m, $k_p h_d$ = 1.06 and $k_p h_s$ = 0.87, the answer is twofold. This is, because the exact range in wave periods is yet unknown. If long waves as shown in figure 1.6 (T = 25 seconds and thus relatively shallow water conditions) occur frequently, a significant excess kurtosis (>0.2 [-]), thus deviation form the linear model, is expected. If these long waves do actually very rarely or do not occur (the waves in figure 1.6 could be a data processing artefact), no increased probability of occurrence of rogue waves is expected. This is because for relatively deep water conditions, it is expected that the approximate 1:200 slope of the sand ridges near future wind farm locations reduces the predicted excess kurtosis ($\approx$ 1) with at least a factor 10. The excess kurtosis is subsequently negligible.

8.3 Recommendations

Recommendations for further research are listed below. The recommendations considering the wave generator and the laser scanner are grouped together at the numbers 4 and 5 respectively.

1. Field data measured by the RVO data campaign must be analysed to obtain accurate regular North Sea and storm conditions at the locations of future offshore wind farms (and in the vicinity of sand ridges). Using these conditions accurate predictions of the excess kurtosis can be made using fully non-linear simulations, using the statistical model for narrow-banded wave fields up to second-order in steepness and 0.44 < kh < 1.6 or by an additional physical experiment. Ideally, wave buoys are spaced across a sand ridge at one (or more) future offshore wind farm locations. However, if no such cross section is already present it would be very expensive to deploy additional/move existing wave buoys. Similarly, it is assumed that an additional physical experiment (with an correctly scaled 1:200 bathymetry) is also quite costly. Taking these two considerations into account a numerical study would be recommended.

2. To assess possible increased damages to structures and/or vessels it is recommended to analyse the characteristics, such as wave period and wave height, of the rogue waves (defined as H/H_s > 2) identified in the field data-set. Using this method it will become clear if the rogue waves indeed pose a potential threat to wind turbines or that the impacts are not that significant. For example, one can imagine that "slamming" (breaking) waves lead to a concentrated heavy dynamic load on wind turbines while gentle waves, where the water surface "slowly" increases and decreases, smear their load on a much longer time scale. Considering vessels, potential threats are nose diving into a wave (remember the "walls of water") and rolling over by getting a "push" sideways. These threats mainly depend on the wave length and steepness of the waves and must therefore be investigated using field data.

3. As discussed in the conclusions, the physical experiments and their results are valid for a relatively shallow environment (kh < 0.5). This does not directly match the relatively deep water conditions considering typical regular and storm waves peak periods at the North Sea. It is therefore recommended to investigate which (shallow) locations in the North Sea correspond with the dimensionless water depths in this study. The experimental data can subsequently directly be applied to this location. A possible area of interest is the shallow Wadden Sea or slightly North of these islands. To obtain accurate wave conditions at these latter locations, field data collected and processed in the recent study by Teutsch et al. (2020) can be used. Additionally, the study found an increase in kurtosis North of the German Wadden island Norderney. If this location is indeed governed by a relatively shallow regime, the experimental results can be used as proof of the increased kurtosis due to depth transitions.

4. Considering the wave generation software AUKE/PC the following two recommendations are made. (1) A cutoff/high-pass filter is implemented if one calls an external file specifying the spectral density. It is shown that specifying a spectral density at the very low frequencies leads to large deviations between the desired (input) and generated (measured in the flume) spectra. (2) The sub-harmonic steering must be adjusted as it is shown that this calculated paddle movement is insufficient for relatively shallow water

conditions $kh < 0.91$. This is further elaborated in section 4.4.3. The used Matlab scripts to adjust the paddle signals can be found via `https://data.4tu.nl/Delft_University_of_Technology` and by typing "Doeleman" in the search box. The "Readme.txt" file provides information about each script file.

5. Considering the SICK laser scanner (set-up) the following recommendations are made. (1) It is recommended to mount the laser on a construction such that it is located between the flume and the crane (thus not on the ceiling). During the physical model tests the laser scanner was mounted on the ceiling to obtain a large scanning field. However, at the Hydraulic Engineering laboratory a crane, constructed across the width of the facility and regularly used, moves between the laser scanner and the flume. This means that measurements are interrupted if the crane moves into the scanning field. A possible solution is that crane operations are be postponed every time a flume test is performed. This is however not desireable as these crane operations must also continue. In addition, every time the crane moves across the laser scanner the cables (connecting the laptop and laser scanner) must be detached deteriorating the connection (the pins are thin and fragile). Using a construction between the flume and crane enough height can be maintained to obtain a sufficient scanning field and the two mentioned disadvantages are eliminated. (2) It is recommended to use seeding with the same density as water ($\rho = 1000$ kg/m^3). It is shown that the applied seeding (density smaller than water which means that it will start to float after some time) seems to "clump" leading to less accurate (or even no) measurements. The applied solution is to "declump" the seeding every morning with a scoop-net. This solution is however not quite ergonomic and it is thought that this could be more efficiently solved by using seeding that does not float and consequently probably will not clump. (3) It is recommended to critically determine the required angular resolution and scan frequency as unnecessary data collection results in large data files that will take much more time to process.

Bibliography

Adcock, T. A. A. and Taylor, P. (2014). The physics of anomalous ('rogue') ocean waves. *Reports on Progress in Physics*, 77(10).

Adcock, T. A. A., Taylor, P. H., Yan, S., Ma, Q. W., and Janssen, P. A. E. M. (2011). Did the draupner wave occur in a crossing sea? *Proceedings of the Royal Society A: Mathematical, Physical and Engineering Sciences*, 467(2134):3004–3021.

Bidlot, J., Cavaleri, L., Bertotti, L., Barbariol, F., Benetazzo, A., Janssen, P., and Wedi, N. (2016). What conditions led to the draupner freak wave? Retrieved from: `https://www.ecmwf.int/en/newsletter/148/meteorology/what-conditions-led-draupner-freak-wave`.

Bolles, C. T., Speer, K., and Moore, M. N. J. (2019). Anomalous wave statistics induced by abrupt depth change. *Physical Review Fluids*, 4(1).

Bosboom, J. and Stive, M. J. F. (2012). *Coastal dynamics I: Lecture notes CIE4305*. Delft: VSSD.

Brijder, M. (2020). Webinar metocean campaign, hollandse kust (west) wind farm zone. Retrieved from: `https://offshorewind.rvo.nl/file/download/55040687`.

Cavaleri, L., Benetazzo, A., Barbariol, F., Bidlot, J.-R., and Janssen, P. A. E. M. (2017). The Draupner Event: The Large Wave and the Emerging View. *Bulletin of the American Meteorological Society*, 98(4):729–735.

Cete, C. (2019). Quantifying the effect of woody vegetation on the wave loads on a dike using remote sensing. (Master's thesis, Technical University Delft) Retrieved from: `https://repository.tudelft.nl`.

Christou, M. and Ewans, K. (2014). Field Measurements of Rogue Water Waves. *Journal of Physical Oceanography*, 44(9):2317–2335.

Collins, C. (2013). Tropical cyclone generated rogue waves. Retrieved from: `http://www.waveworkshop.org/13thWaves/Papers/Tropical%20Cyclone%20Generated%20Extreme%20Waves%20-%20waveworkshop%20paper.pdf`.

Deltares (2021a). Programmable electromagnetic liquid velocity meter. Retrieved from: `https://www.deltares.nl/nl/faciliteiten/standaard-meetinstrumenten/`.

Deltares (2021b). Wave height meter. Retrieved from: `https://www.deltares.nl/nl/faciliteiten/standaard-meetinstrumenten/`.

Ducrozet, G. and Gouin, M. (2017). Influence of varying bathymetry in rogue wave occurrence within unidirectional and directional sea-states. *Journal of Ocean Engineering and Marine Energy*.

Dysthe, K., Krogstad, H., and Müller, P. (2008). Oceanic rogue waves. *Annual Review of Fluid Mechanics*, 40:287–310.

Dysthe, K., Krogstad, H., and Müller, P. (2010). Rogue waves. *Encyclopedia of Ocean Sciences*, pages 770–780.

EMODnet (2020). Bathymetry. Retrieved from: `https://portal.emodnet-bathymetry.eu/`.

Fernandez, L., Onorato, M., Monbaliu, J., and Toffoli, A. (2016). *Occurrence of Extreme Waves in Finite Water Depth*, chapter 3. Springer, second edition.

Flick, R. and Guza, R. (1980). Paddle generated waves in laboratory channels. 106:79–97.

Forristall, G. (1978). On the statistical distribution of wave heights in a storm. *Journal of Geophysical Research*, 83:2353–2358.

Forristall, G. (2008). How should we combine long and short term wave height distributions? volume 2.

Frostick, L. E., McLelland, S., and Mercer, T. (2011). Users guide to physical modelling and experimentation : Experience of the hydralab network.

Goda, Y. (2000). *Random Seas And Design Of Maritime Structures*, volume 15 of *Advanced series on ocean engineering*. World Scientific Publishing Co Pte Ltd.

Gramstad, O., Zeng, H., Trulsen, K., and Pedersen, G. K. (2013). Freak waves in weakly nonlinear unidirectional wave trains over a sloping bottom in shallow water. *Physics of Fluids*, 25(12).

Guedes Soares, C., Cherneva, Z., and Antão, E. (2003). Characteristics of abnormal waves in north sea storm sea states. *Applied Ocean Research*, 25(6):337 − 344.

Haver, S. (2004). A possible freak wave event measured at the draupner jacket, january 1 1995.

Haver, S. and Andersen, O. (2000). Freak waves: Rare realizations of a typical population or typical realizations of a rare population? volume 3.

Holthuijsen, L. (2007). *Waves in oceanic and coastal waters*, volume 9780521860284. Cambridge University Press.

Hughes, S. A. (1993a). Laboratory wave reflection analysis using co-located gages. *Coastal Engineering*, 20(3):223 − 247.

Hughes, S. A. (1993b). *Physical models and laboratory techniques in coastal engineering*. World Scientific.

Janssen, T. T. and Herbers, T. H. C. (2009). Nonlinear wave statistics in a focal zone. *Journal of Physical Oceanography*, 39(8):1948–1964.

Karin Magnusson, A. and Donelan, M. A. (2013). The Andrea Wave Characteristics of a Measured North Sea Rogue Wave. *Journal of Offshore Mechanics and Arctic Engineering*, 135(3).

Kashima, H., Hirayama, K., and Mori, N. (2014). Estimation of freak wave occurrence from deep to shallow water regions. *Coastal Engineering Proceedings*, 1(34):1–13.

Kharif, C. and Pelinovsky, E. (2003). Physical mechanisms of the rogue wave phenomenon. *European Journal of Mechanics, B/Fluids*, 22(6):603–634.

Kharif, C., Pelinovsky, E., and Slunyaev, A. (2009). *Rogue Waves in the Ocean*. Advances in Geophysical and Environmental Mechanics and Mathematics. Springer. ISBN: 978-3-540-88418-7.

Krogstad, H., Barstow, S., Mathisen, J., Lønseth, L., AS, F. O., Magnusson, A., and Donelan, M. (2008). Rogue waves 2008. In Olagnon, M. and Prevosto, M., editors, *Extreme Waves in the Long-Term Wave Measurements at Ekofisk Harald*. Ifremer.

Li, Y., Draycott, S., Adcock, T., and van den Bremer, T. (2021a). Surface wavepackets subject to an abrupt depth change. part ii: experimental analysis. *Journal of Fluid Mechanics*.

Li, Y., Draycott, S., Zheng, Y., Lin, Z., Adcock, T., and van den Bremer, T. (2020a). Supplementary information for: Why rogue waves occur atop depth transitions. Under review.

Li, Y., Draycott, S., Zheng, Y., Lin, Z., Adcock, T., and van den Bremer, T. (2020b). Why rogue waves occur atop depth transitions. Under review.

Li, Y., Zheng, Y., Lin, Z., Adcock, T., and van den Bremer, T. (2021b). Surface wavepackets subject to an abrupt depth change. part i: second-order theory. *Journal of Fluid Mechanics*.

Liu, P. (2007). A chronology of freaque wave encounters. *GEOFIZIKA*, 24(1):57–70. `https://www.glerl.noaa.gov/pubs/fulltext/2007/20070019.pdf`.

Ma, Y., Dong, G., and Ma, X. (2014). Experimental study of statistics of random waves propagating over a bar. *Coastal Engineering Proceedings*, 1:30.

Mackay, E. and Johanning, L. (2018). Long-term distributions of individual wave and crest heights. *Ocean Engineering*, 165:164 − 183.

Majda, A. J., Moore, M. N. J., and Qi, D. (2019). Statistical dynamical model to predict extreme events and anomalous features in shallow water waves with abrupt depth change. *Proceedings of the National Academy of Sciences*, 116(10):3982–3987.

Massel, S. (1983). Harmonic generation by waves propagating over a submerged step. *Coastal Engineering*, 7(4):357 − 380.

Moore, M. N. J., Bolles, C. T., Majda, A. J., and Qi, D. (2020). Anomalous waves triggered by abrupt depth changes: laboratory experiments and truncated kdv statistical mechanics.

Mori, N. and Janssen, P. A. E. M. (2006). On kurtosis and occurrence probability of freak waves. *Journal of Physical Oceanography*, 36(7):1471–1483.

Noordzeeloket (2020). Windparken in ontwikkeling. Retrieved from: `https://www.noordzeeloket.nl/functies-gebruik/windenergie-zee/in-ontwikkeling-op/`.

Olagnon, M. and Iseghem, S. V. (2000). Some cases of observed rogue waves and attempts to characterize their occurrence conditions.

Onorato, M., Residori, S., Bortolozzo, U., Montina, A., and Arecchi, F. T. (2013). Rogue waves and their generating mechanisms in different physical contexts. *Physics Reports*, 528(2):47–89.

Orszaghova, J., Taylor, P. H., Borthwick, A. G., and Raby, A. C. (2014). Importance of second-order wave generation for focused wave group run-up and overtopping. *Coastal Engineering*, 94:63 − 79.

Parker, B. (2020). The power of the sea. Retrieved from: `http://thepowerofthesea.com/images.html`.

Paulsen, B. T., de Sonneville, B., van der Meulen, M., and Jacobsen, N. G. (2019). Probability of wave slamming and the magnitude of slamming loads on offshore wind turbine foundations. *Coastal Engineering*, 143:76–95.

Rijksoverheid (2020). Waar staan en komen de windparken op zee? Retrieved from: `https://windopzee.nl/onderwerpen-0/wind-zee/waar/`.

RVO (2020). Home. Retrieved from: `https://offshorewind.rvo.nl/`.

Røsjø, B. and Hauge, K. (2011). Proof: Monster waves are real. Retrieved from: `https://partner.sciencenorway.no/feature-forskningno-geography/proof-monster-waves-are-real/1435235`.

Schober, C. and Calini, A. (2016). *Rogue Waves in Higher Order Nonlinear Schrödinger Models*, chapter 1. Springer, second edition.

Schäffer, H. A. (1996). Second-order wavemaker theory for irregular waves. *Ocean Engineering*, 23(1):47 − 88.

Sergeeva, A., Pelinovsky, E., and Talipova, T. (2011). Nonlinear random wave field in shallow water: variable korteweg-de vries framework. *Natural Hazards and Earth System Sciences*, 11(2):323–330.

SICK AG (2017). *Operating Instructions LMS5xx Laser Measurement Sensors*. Waldkirch, Germany. Retrieved from: `https://www.sick.com/ag/en/detection-and-ranging-solutions/2d-lidar-sensors/lms5xx/lms511-20100-pro/p/p216240`.

Skourup, J., Hansen, N.-E. O., and Andreasen, K. K. (1997). Non-Gaussian Extreme Waves in the Central North Sea. *Journal of Offshore Mechanics and Arctic Engineering*, 119(3):146–150.

Slunyaev, A., Pelinovsky, E., and Guedes Soares, C. (2005). Modeling freak waves from the north sea. *Applied Ocean Research*, 27:12–22.

Smith, C. (2007). Extreme waves and ship design. Retrieved from: `http://www.shipstructure.org/pdf/2007symp09.pdf`.

Stansell, P. (2004). Distributions of freak wave heights measured in the north sea. *Applied Ocean Research*, 26(1-2):35–48. Retrieved from: `https://www.sciencedirect.com/science/article/pii/S0141118705000052`.

Teutsch, I., Weisse, R., Moeller, J., and Krueger, O. (2020). A statistical analysis of rogue waves in the southern north sea. *Natural Hazards and Earth System Sciences*, 20(10):2665–2680.

The European Space Agency (2004a). Rare photo of a rogue wave. Retrieved from: `https://www.esa.int/ESA_Multimedia/Images/2004/06/Rare_photo_of_a_rogue_wave`.

The European Space Agency (2004b). Ship-sinking monster waves revealed by esa satellites. Retrieved from: `https://www.esa.int/Applications/Observing_the_Earth/Ship-sinking_monster_waves_revealed_by_ESA_satellites`.

The New York Times (2006). Storm surge the chief engineer of the stolt surf took photographs as the tanker met a rogue wave in 1977. Retrieved from: `https://archive.nytimes.com/www.nytimes.com/imagepages/2006/07/11/science/11wave.1.sectionspan.html`.

Trulsen, K. (2018). *Rogue Waves in the Ocean, the Role of Modulational Instability, and Abrupt Changes of Environmental Conditions that Can Provoke Non EquilibriumWave Dynamics*, chapter Part II. Springer Oceanography.

Trulsen, K., Raustøl, A., Jorde, S., and Rye, L. B. (2020). Extreme wave statistics of long-crested irregular waves over a shoal. *Journal of Fluid Mechanics*, 882:R2.

Trulsen, K., Zeng, H., and Gramstad, O. (2012). Laboratory evidence of freak waves provoked by non-uniform bathymetry. *Physics of Fluids*, 24(9).

van Leeuwen, P. J. and Klopman, G. (1996). A new method for the generation of second-order random waves. *Ocean Engineering*, 23(2):167 − 192.

Viotti, C. and Dias, F. (2014). Extreme waves induced by strong depth transitions: Fully nonlinear results. *Physics of Fluids*, 26:051705.

Walker, D., Taylor, P., and Taylor, R. (2004). The shape of large surface waves on the open sea and the draupner new year wave. *Applied Ocean Research*, 26(2-3):73–83. Retrieved from: `https://www.sciencedirect.com/science/article/pii/S0141118705000052`.

Zeng, H. and Trulsen, K. (2012). Evolution of skewness and kurtosis of weakly nonlinear unidirectional waves over a sloping bottom. *Natural Hazards and Earth System Sciences*, 12(3):631–638.

Zhang, J., Benoit, M., Kimmoun, O., Chabchoub, A., and Hsu, H.-C. (2019). Statistics of extreme waves in coastal waters: Large scale experiments and advanced numerical simulations. *Fluids*, 4:99.

Zheng, Y., Lin, Z., Li, Y., Adcock, T. A. A., Li, Y., and van den Bremer, T. S. (2020). Fully nonlinear simulations of unidirectional extreme waves provoked by strong depth transitions: The effect of slope. *Phys. Rev. Fluids*, 5:064804.

Appendices

Supplementary equations theoretical framework

In this appendix additional relevant equations that are used in the theoretical framework which is introduced in section 2.5 are presented. The equations from the statistical (irregular wave) model are repeated from Li et al. (2020b) including the method of notation. Tildes are therefore also used in this appendix to indicate random variables and the subscripts b and f denote the bound and free waves respectively. An even more in depth description of the model can be found in Li et al. (2020a)

As mentioned in section 2.5 two-dimensional potential-flow theory neglecting effects of viscosity, density differences, evanescent waves and surface tension is considered. The incoming wave field is considered to be staionary, constant in time, homogeneous, of the same kind and normally incident, perpendicular to the depth transition. Additionally assuming a normally distributed surface elevation, the envelope $\tilde{A}$ can be described by the Rayleigh distribution, see equation A.1 and phase $\tilde{\psi}$ by a uniform distribution with $0 \leq \tilde{\psi} \leq 2\pi$, see equation A.2. μ_0 Is the variance of the surface elevation.

$$f_{\tilde{A}}(A; \mu_0) = \frac{A}{\mu_0} \exp\left(-\frac{A^2}{2\mu_0}\right) \quad \text{for} \quad 0 < A < \infty \tag{A.1}$$

$$f_{\tilde{\psi}}(\psi) = \frac{1}{2\pi} \quad \text{for} \quad 0 \leq \tilde{\psi} \leq 2\pi \tag{A.2}$$

After solving the combines Stokes and multiple scales expansion (which is shortly discussed in section 2.5 and therefore not repeated here) the following expressions for the surface elevation at $x > 0$, thus the shallow side are obtained.

$$\tilde{\zeta}_s^{(1)} = |T_0|\tilde{A}\cos(\tilde{\psi} + \theta_{T_0}) \tag{A.3}$$

$$\tilde{\zeta}_s^{(2)}(x) = \tilde{\zeta}_s^{(20)}(x) + \tilde{\zeta}_s^{(22)}(x) \tag{A.4}$$

$$\tilde{\zeta}_s^{(20)}(x) = k_{0s}|T_0|^2 \tilde{A}^2 \left(C_{20,b} + C_{20,f} R_{20}(x)\right) \tag{A.5}$$

$$\tilde{\zeta}_s^{(22)}(x) = k_{0s}|T_0|^2 \tilde{A}^2 \left(C_{22,b}\cos(2\tilde{\psi} + 2\theta_{T_0}) + C_{22,f} R_{22}(x)\cos(2\tilde{\psi} + 2\theta_{T_0} + \psi_{22,f}(x))\right) \tag{A.6}$$

The second order bound $C_{20,b}$, $C_{22,b}$ and free $C_{20,f}$, $C_{22,f}$ coefficients including the phase shift $\psi_{22,f}(x)$ that arise in the solution of the surface elevation are determined using equation A.7, A.8, A.9, A.10 and A.11. T_0, T_{20}, and $T_{22,f}$ are the complex transmission coefficients which are obtained from the boundary conditions at the step and represent the size of the transmitted components. Similarly R is the reflection coefficient and thus represents a measure for the size of the reflected waves. k_{0s} is the wave number at the shallow water side, k_{20s} the super-harmonic wave number at the shallow water side, c_g the group velocity, h, k and ω the considered water depth, wave number and angular frequency respectively. θ Is the phase shift of the considered component due to the presence of the depth transition and is therefore equal to argument of its corresponding transmission coefficient ($\arg(T)$).

$$C_{20,b}(kh) = \frac{1}{4(gh - c_g^2)}\left(\frac{2gh - c_g^2}{2\sinh 2kh} + \frac{2gc_g}{\omega}\right) \tag{A.7}$$

$$C_{22,b}(kh) = \frac{\cosh kh(2\cosh^2 kh + 1)}{4\sinh^3 kh} \tag{A.8}$$

$$C_{20,f} = |T_{20,f}|/|T_0|^2 \tag{A.9}$$

$$C_{22,f} = 2\omega_0^2|T_{22,f}|/(gk_{0s}|T_0|^2) \tag{A.10}$$

$$\psi_{22,f}(x) = k_{20s}x - 2k_{0s}x + \theta_{T_{22,f}} - 2\theta_{T_0} \tag{A.11}$$

$R_{20}(x)$ And $R_{22}(x)$ are the non-dimensional envelope functions which are described by the following functions with A the deterministic envelope and $S(\omega)$ the considered wave spectrum. At infinite distance away from the depth transition (step) $R_{20}, R_{22} \to 0$ an homogeneous wave field adjusted to the new constant depth will be obtained.

$$R_{20}(x) = A^2(x/\sqrt{gh_s} - x/c_{g0s})/A^2(0) \tag{A.12}$$

$$R_{22}(x) = A^2(x/c_{g20s} - x/c_{g0s})/A^2(0) \tag{A.13}$$

$$A(t) = \int \sqrt{2S(\omega)}\cos((\omega - \omega_0)t)d\omega \tag{A.14}$$

The kurtosis and skewness, vertical and horizontal deviation from a normal distribution, can now be obtained using the coefficients and expressions presented above. The variance of the surface elevation on the shallow side is represented by μ_{0s} and is the product of the variance of the deep water side multiplied with the absolute value of the transmission coefficient squared ($|T_0|^2\mu_0$). Logically, the contribution to the kurtosis in space per component b, f and combined bf is given by equation A.16, A.17 and A.18 respectively. Again, it is stressed that the final expressions for the kurtosis and skewness in equation A.20 and A.19 are valid up to second-order and therefore do not include third or higher order effects.

$$C_2(x) = C_{20,b} + C_{22,b} + C_{20,f}R_{20}(x) + C_{22,f}R_{22}(x)\cos\psi_{22,f}(x) \tag{A.15}$$

$$\kappa_{2,b} = 3C_{20,b}^2 + 4C_{20,b}C_{22,b} + 3C_{22,b}^2 \tag{A.16}$$

$$\kappa_{2,f}(x) = 3C_{20,f}^2R_{20}^2 + 4C_{20,f}C_{22,f}R_{20}R_{22}\cos\psi_{22,f} + 3C_{22,f}^2R_{22}^2 \tag{A.17}$$

$$\kappa_{2,bf}(x) = (6C_{20,b} + 4C_{22,b})(C_{20,f}R_{20} + C_{22,f}R_{22}\cos\psi_{22,f}) \tag{A.18}$$

$$s(x) = 6k_{0s}\sqrt{\mu_{0s}}C_2(x) + \mathcal{O}(\mu_{0s}^{3/2}) \tag{A.19}$$

$$\kappa(x) = 3 + 24k_{0s}^2\mu_{0s}\left(\kappa_{2,b} + \kappa_{2,bf}(x) + \kappa_{2,f}(x)\right) + \mathcal{O}(\mu_{0s}^2) \tag{A.20}$$

Laser scanner seeding

During the physical experiments a 2D LiDAR Laser scanner has been used, in addition to the eight wave gauges, to measure the surface elevation. As the fresh water in the flume is clear, three liters of dry seeding mixed over a length of approximately 20 meters (±2 meters before the step till ±18 meters behind the step, located at $x = 0$) is added to ensure that the laser pulses are reflected at the water surface. The used seeding is the SPHERICEL $^{®}$ 60P18 which has a $d_{50} = 19$ μm and density of 600 kg/m^3. This means that the hollow glass spheres slowly start to move towards the water surface when the water is not continuously mixed. During the first set of experiments (with the step) it was noticed that the amount of seeding seemed to decrease (visually and using the RSSI, Received Signal Strength Indicator, values). To investigate whether this observation could be due to dissipation or the discharge of highly concentrated water to the sewer, the concentration in terms of NTU (which is a measure for the turbidity) was measured at the start of each experimental day during the second set of experiments (with the slope) at several locations along the flume. Before a sample of the water in the flume was taken, first the seeding was mixed over depth.

Table B.1 shows an overview of the measured seeding concentration at several locations along the flume. At each location the concentration was measured thrice and hereafter averaged to decrease the error of the measurements. The last column on the right shows the average of the turbidity at the measured locations in front of the gravel beach. The average turbidity of the water discharged to the sewer (in order to lower the water depth from 0.55 m to 0.27 m) was found to be equal to 12 NTU. Considering the turbidity levels shown in table B.1, this outlet is not considered to be a possible explanation of 'disappearing' seeding. In addition, it can be observed in table B.1 that for day 1 till 4 the turbidity levels and therefore the concentration seemed to decrease, however at the fifth and last day of the experiments, turbidity levels reached again approximately the same value as was measured during day 1 and 2. As the turbidity was measured twice that day, it is assumed that the increased NTU values are not due to a measurement error. Summarising, because these high concentrations were measured at the last day, it is not likely that the seeding dissipated.

	x = -6 [m]	x = 0 [m]	x = 7.5 [m]	x = 17 [m]	x = 30 [m]	Mean x = -6 till 17 [m]
	NTU	NTU	NTU	NTU	NTU	NTU
Day 1	-	96	77	116	-	96
Day 2	-	45	118	89	2.4	84
Day 3	86	78	90	43	2.3	74
Day 4	121	53	75	41	1.6	73
Day 5 morning	54	103	88	81	3.8	82
Day 5 afternoon	19	169	89	77	1.3	89

Table B.1: Overview seeding analysis. Concentration of seeding in terms of NTU (turbidity) at several locations along the flume with x = 0 the start of the step and thus end of the slope.

Another possible explanation of the visually decreased seeding and lower RSSI values, is the clumping of the seeding. This 'clumping' can clearly be observed in figure B.1a and B.1b. In addition, it could have been possible that the seeding accumulated behind the wave paddle. However, since it was not possible to measure the NTU at this location and because visually no significant difference was found (using pictures taken every morning) it is concluded that this accumulation is not the direct cause. Also, because the seeding is not found to dissipate or to be discharged into the sewer, it is concluded that the clumping of the seeding is the cause of the lower RSSI values over time.

Figure B.1: *Pictures taken of the flume showing the seeding at the water surface in the morning before mixing and testing. a) Shows the seeding at the first day of the second set of tests. b) Shows the seeding at the fifth and last day of the second experimental set. Figure (b) results in lower RSSI values.*

C

Reflection analysis: Vertical array and propagation method

In this appendix relevant equations for the vertical array or also called co-located gauge method are presented. Next, the equations for the adjusted Guza method are shown. In addition, a reflection propagation method is discussed.

C.1 Relevant equations vertical array reflection analysis

The vertical array method is a frequency domain reflection analysis technique using linear wave theory that links the surface elevation and the horizontal particle velocity at each frequency component i using a velocity transfer function. The governing equations are presented below. The derivation starts with determination of the irregular linearly imposed velocity potential for waves on a flat bottom in equation C.1 with k the wavenumber, ω the angular frequency, h water depth, a amplitude, t time, x distance ϵ the phase angle and z the location in the water column ($z = 0$ and $z = -h$ representing the water surface and sea bottom respectively). The expressions for the surface elevation η and horizontal velocity u are found using the dynamic boundary condition at the surface and using the spatial derivative, see equations C.2, C.3 and C.4 (Hughes, 1993b,a). It can now be observed that the surface elevation and the velocity is linked to each other with the velocity transfer function Z_i in equation C.5. Using these equations and the vertical array of wave gauges and velocity meters, the surface elevation signal can now be split into the incoming and reflected wave field.

$$\Phi(x, z, t) = -\frac{ga_I}{\omega} \frac{\cosh k(h+z)}{\cosh kh} \sin(kx - \omega t + \epsilon_I) + \frac{ga_R}{\omega} \frac{\cosh k(h+z)}{\cosh kh} \sin(kx + \omega t + \epsilon_R) \tag{C.1}$$

$$\eta = \frac{1}{g} \left[\frac{\partial \Phi}{\partial t} \right]_{z=0} \qquad u = -\frac{\partial \Phi}{\partial x} \tag{C.2}$$

$$\eta(x, z, t) = \sum_{i=1}^{\infty} \left[a_{Ii} \cos(k_i x - \omega_i t + \epsilon_{Ii}) + a_{Ri} \cos(k_i x + \omega_i t + \epsilon_{Ri}) \right] \tag{C.3}$$

$$u(x, z, t) = \sum_{i=1}^{\infty} \left[a_{Ii} Z_i \cos(k_i x - \omega_i t + \epsilon_{Ii}) - a_{Ri} Z_i \cos(k_i x + \omega_i t + \epsilon_{Ri}) \right] \tag{C.4}$$

$$Z_i = \frac{gk_i}{\omega_i} \frac{\cosh k_i(h+z)}{\cosh k_i h} \tag{C.5}$$

C.2 Relevant equations adjusted Guza method

The adjusted Guza method presented in this section is a variant on the vertical array method shown in section C.1. Again, surface elevation and velocity measurements are linked to each other with the velocity transfer function Z, equation C.10. This method however considers long waves (for these experiments <0.2 Hz) and therefore waves within the shallow water limit Hughes (1993b). This means that the free waves propagate with the shallow water speed $\sqrt{gh}$ and all waves have a constant velocity over depth. In addition, knowing that the bound waves travel approximately with the speed of the average group c_{gp}, the following equations are derived. Again, η, u and h represent the surface elevation, horizontal velocity and water depth respectively.

$$\eta = \eta_I - \eta_R \tag{C.6}$$

$$u = u_I - u_R \tag{C.7}$$

$$\eta_I = \frac{\eta\sqrt{gh} + hu}{c_{gp} + \sqrt{gh}} \tag{C.8}$$

$$u_I = \frac{c_{gp}}{h}\eta_I \tag{C.9}$$

$$Z = \frac{c_{gp}}{h} \tag{C.10}$$

C.3 Reflection propagation method

Due to limited availability of velocity meters, not at all wave gauge locations a vertical array could be set-up. Using the vertical array method based on linear theory, the reflections in the total wave field are calculated and are then propagated towards a new location x using equation C.11. a_i Is the discrete spectral amplitude, f_i the discrete frequency considered, t is time, ϵ the discrete phase and k_i the wavenumber. As the adjusted Guza method only allows for the separation of free and bound sub-harmonics, the calculated incoming wave field for WG2 till WG8 will theoretically be incorrect. This is because, besides the bound sub-harmonics, free sub-harmonic components arise due to interactions with the depth transition. These free sub-harmonics travel in the same direction as the bound waves and are part of the incoming wave field. These waves are however not detected as incoming waves and therefore incorrectly labelled as reflections. As the detected reflections in the low-frequency region after the depth transition are therefore already theoretically incorrect, there is no point to test/apply the propagation method.

$$\eta_x = \sum_{i=1}^{N} a_i \cos(2\pi f_i t + \epsilon_i + k_i x) \tag{C.11}$$

As during half of the tests 6 EMFs were used, the propagation method is tested using the following step-by-step plan:

1. Linear theory does not include correct separation of incoming and reflected waves for the low- and high-frequencies, therefore a high- and low-pass filter is used to eliminate frequencies below 0.2 Hz and above 0.8 Hz in the surface elevation (wave gauge) and velocity signals (EMF). Using these limits no significant spectral density is lost, see figure 5.3.

2. The total wave field at the last wave gauge; WG8, see figure 3.6, is split into reflected and incoming waves.

3. The total wave field at WG6 (x≈6 m distance from WG8), WG5 (x≈8 m) and WG3 (x≈15 m) are also split into reflected and incoming waves.

4. The reflected waves from WG8 are propagated using equation C.11 to WG6, WG5 and WG3.

5. The time lag between the propagated and 'true' reflections is determined by finding the phase lag which leads to the smallest correlation coefficient.

6. The propagated and true reflections are plotted with the correlation coefficient in the plot title.

Because due to, for instance, energy loss or a small difference in calibration, the amplitudes of the true and propagated might not match. An empirical constant (for propagated reflections) must be used to find a right fit. To avoid this empirical constant to be of influence of how well the signals match, the dimensionless correlation coefficient, ρ, is used.

Figures C.1, C.2 and C.3 present the results of the step-by-step plan for test 2 (water depth of 0.5 meter, spectral bandwidth of 0.15 and spectral amplitude of 5.36 centimeter). Remarkable is that ρ decreases for increasing distance from WG8. This makes sense as with increasing distance other factors or processes might play a role that are not accounted for. It must be concluded that the propagation method presented in this section is not sufficient as the correlation between the two signals is too small. At some points, for example, the true and propagated reflections have an opposite sign. This would make data processing results using the identified incident wave field even worse than 'just' using the total wave field.
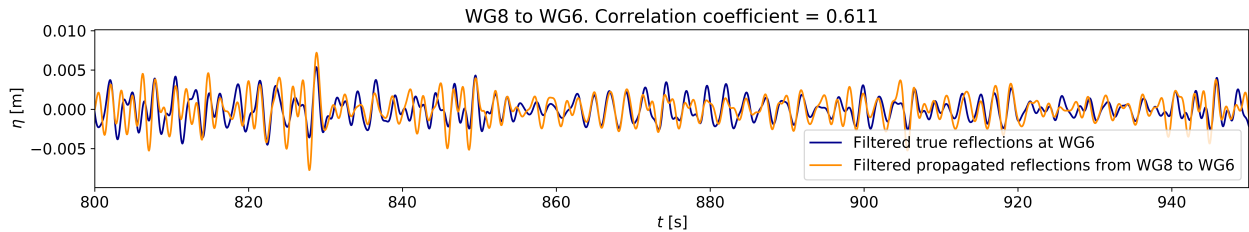
Figure C.1: Propagated (WG8) and true reflections at WG6, x≈6 meter distance away from WG8, ρ=0.611.
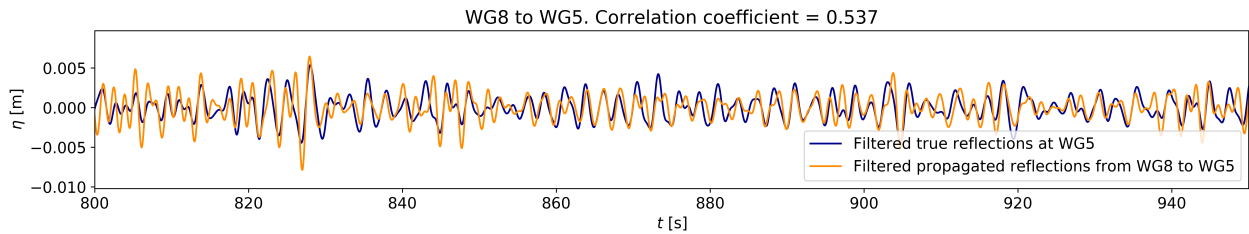
Figure C.2: Propagated (WG8) and true reflections at WG5, x≈8 meter distance away from WG8, ρ=0.537.
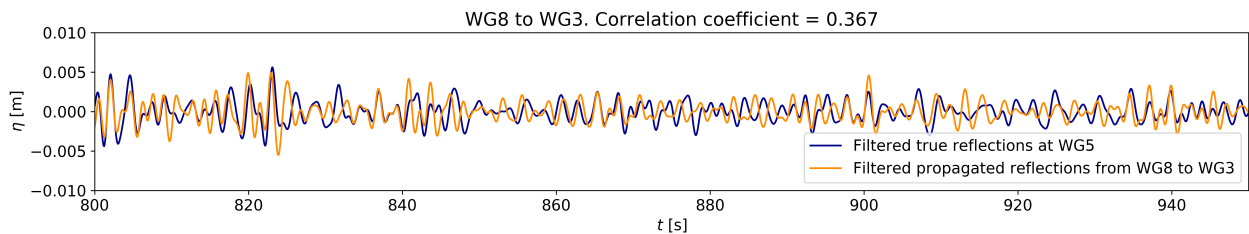
Figure C.3: Propagated (WG8) and true reflections at WG5, x≈15 meter distance away from WG8, ρ=0.367.

D

Additional information data processing and data analysis

In this appendix table D.1 is given which provides additional information regarding chapters 5 and 6. The left column of the table presents the mean reflection coefficient K_r at WG1 (x = -3 m) between 0.2 < f < 0.6 Hz. This is the frequency region with highest spectral densities. It must be noted that the reflection coefficient is quite strongly dependent on the absolute values of the wave gauges and velocity meters. Because it was noticed for test 7 and 8 that the wave gauges and velocity meters differed much more than for the other tests, the velocity meter data for these tests is multiplied with 0.8 for more logical results. The reflection coefficients are still however on the high side, which might be because there are actually that many reflections or that the velocity meter should be multiplied with an even lower constant than 0.8. In addition, during test 5 and 4a the velocity meter at WG1 showed unrealistic 'wiggles'. For this reason the reflection coefficients for these tests are calculated at WG2. Also, it can be observed that no reflection coefficient is calculated for test 1 and 1a. This is because the velocity meters were not submerged on time (these were the first two tests) and therefore showed large wiggles which are not part of the wave motion.

The second and third column of the table show the spectral deviation $(1 - H_{m0gaus}/H_{m0})$ per test. It can be observed that tests 1a, 2a 4a, 3b and 6b were not performed with a 1:20 slope. The four right columns show the skewness and kurtosis of the waves at WG1 and the measured wave paddle motion.

No.	Step $Kr_{(0.2-0.6)Hz}$ [-]	Step $1 - H_{m0gaus}/H_{m0}$ [-]	Slope	Step s_{waves} [-]	κ_{waves} [-]	$s_{pad,m}$ [-]	$\kappa_{pad,m}$ [-]
1	-	8.2%	4.9%	0.08	3.0	-0.1	3.3 ±0.18
2	16.5%	7.4%	4.5%	0.07	3.0	-0.13	3.3 ±0.17
3	15.7%	5.8%	4.1%	0.05	3.0	-0.07	3.2 ±0.15
4	18.1%	5.4%	10%	0.02	3.0	-0.04	3.2 ±0.14
5	18.5%	18.1%	19.0%	0.11	4.1	0.0	3.3 ±0.15
6	36.1%	22.8%	21.9%	0.14	4.2	-0.01	3.4 ±0.17
7	51.4%	42.9%	41.0%	0.21	5.2	-0.04	3.7 ±0.19
8	59.8%	36.0%	34.2%	0.1	5.1	0.06	3.5 ±0.18
1a $\delta\uparrow$	-	27.3%	-	0.41	4.6	0.0	3.5 ±0.18
2a $\delta\uparrow$	17.5%	26.0%	-	0.31	4.4	-0.02	3.5 ±0.17
4a $\delta\uparrow$	16.3%	22.9%	-	0.18	4.3	-0.02	3.4 ±0.18
1b $kA\uparrow$	12.2%	11.4%	9.1%	0.16	3.1	-0.13	3.4 ±0.20
3a $kA\uparrow$	15.9%	10.5%	9.0%	0.09	3.1	-0.03	3.4 ±0.16
6a $kA\uparrow$	53.6%	45.4%	45.0%	0.81	6.3	0.01	3.8 ±0.21
3b $kA\downarrow$	19.1%	3.5%	-	0.01	2.9	-0.06	3.0 ±0.13
6b $kA\downarrow$	36.4%	3.6%	-	-0.01	2.9	0.0	2.9 ±0.10

Table D.1: Additional information reflections, wave spectra and wave paddle analysis.

Additional figures of the development of the kurtosis in space

In this appendix the results of the development of the kurtosis in space for all tests are shown. The order is similar to the presented test program. The model predictions are obtained using the spectral significant wave height derived at the first wave gauge (x = -3 m).
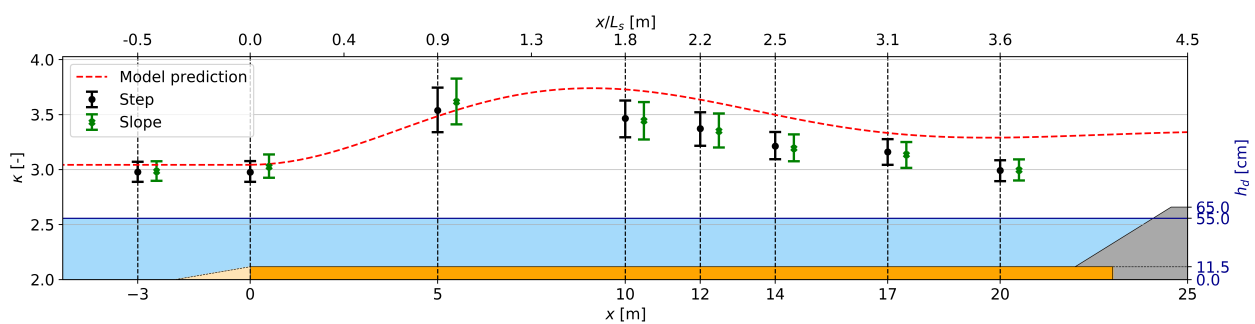
Figure E.1: Test 1. Development of the kurtosis κ in space. Start of the step at x = 0. The 95% confidence bounds of the kurtosis obtained from the experiment are shown in black and green with a step and slope respectively. The model prediction is shown with a red dashed line.
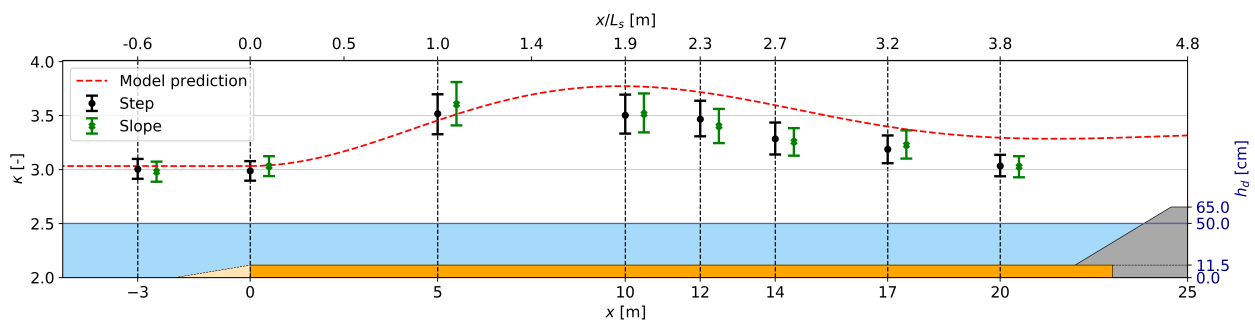
Figure E.2: Test 2. Development of the kurtosis κ in space. Start of the step at x = 0. The 95% confidence bounds of the kurtosis obtained from the experiment are shown in black and green with a step and slope respectively. The model prediction is shown with a red dashed line.
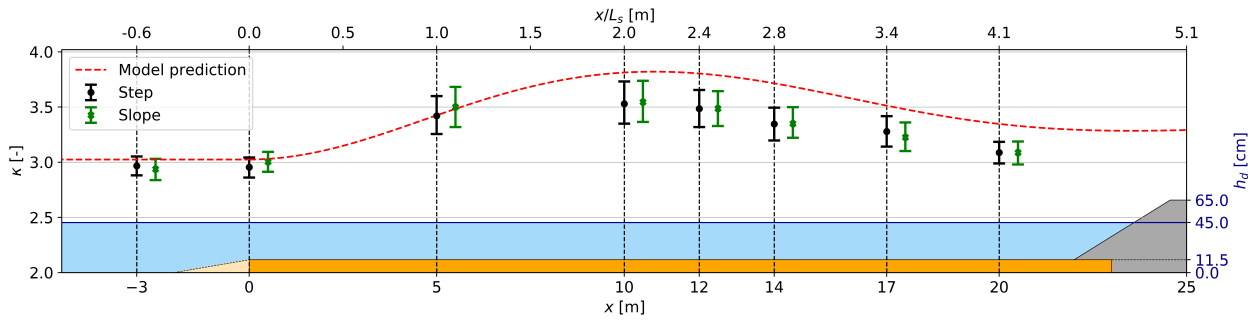
Figure E.3: Test 3. Development of the kurtosis κ in space. Start of the step at x = 0. The 95% confidence bounds of the kurtosis obtained from the experiment are shown in black and green with a step and slope respectively. The model prediction is shown with a red dashed line.
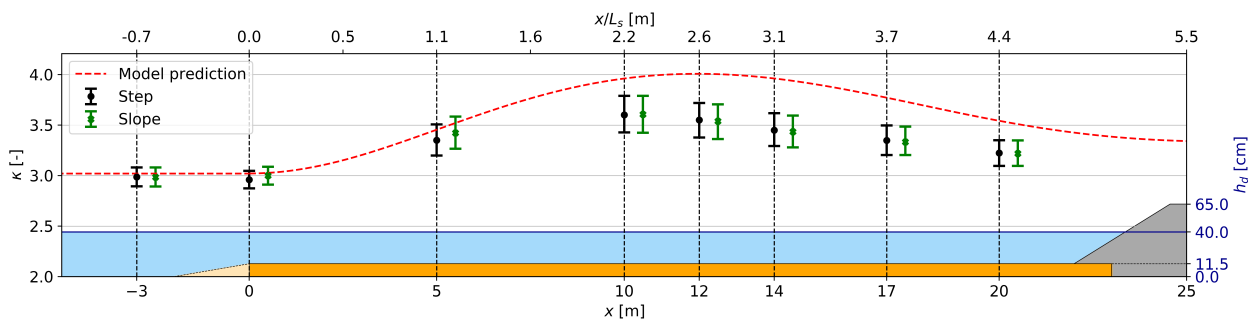
Figure E.4: Test 4. Development of the kurtosis κ in space. Start of the step at x = 0. The 95% confidence bounds of the kurtosis obtained from the experiment are shown in black and green with a step and slope respectively. The model prediction is shown with a red dashed line.
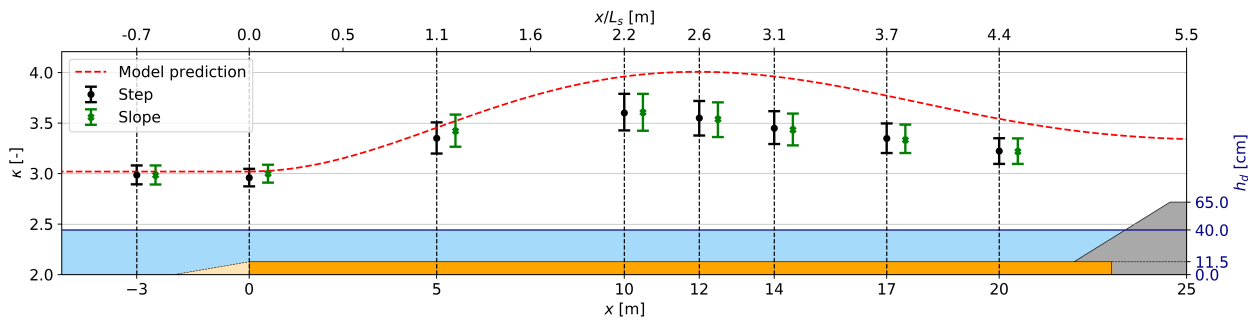
Figure E.5: Test 4. Development of the kurtosis κ in space. Start of the step at x = 0. The 95% confidence bounds of the kurtosis obtained from the experiment are shown in black and green with a step and slope respectively. The model prediction is shown with a red dashed line.
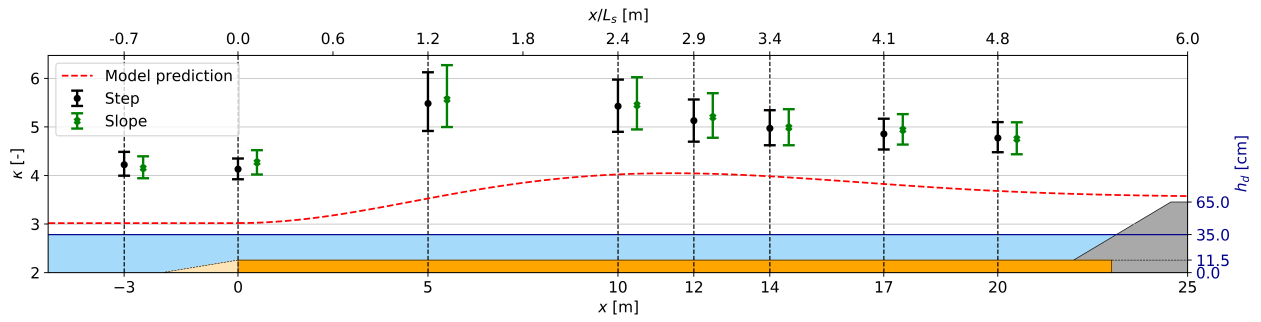
Figure E.6: Test 6. Development of the kurtosis κ in space. Start of the step at x = 0. The 95% confidence bounds of the kurtosis obtained from the experiment are shown in black and green with a step and slope respectively. The model prediction is shown with a red dashed line.
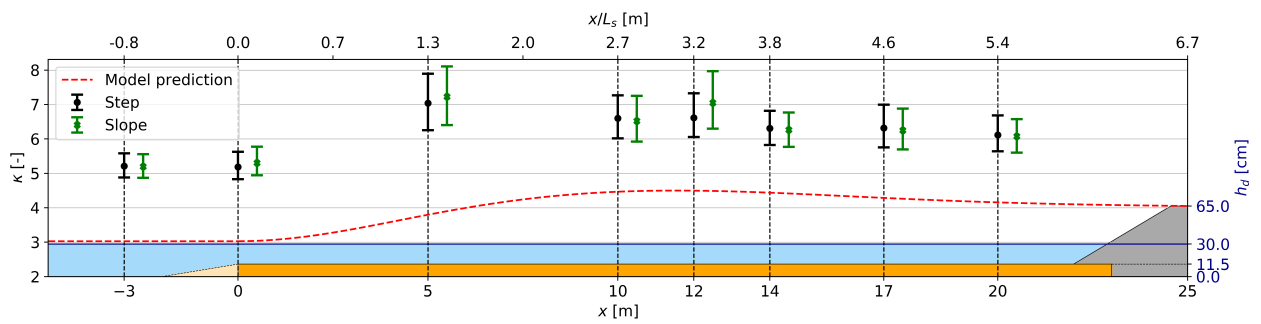
Figure E.7: Test 7. Development of the kurtosis κ in space. Start of the step at x = 0. The 95% confidence bounds of the kurtosis obtained from the experiment are shown in black and green with a step and slope respectively. The model prediction is shown with a red dashed line.
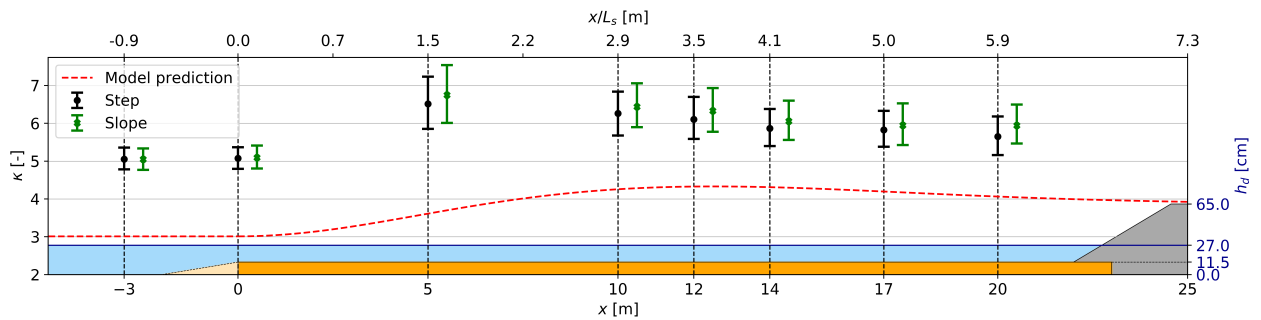
Figure E.8: Test 8. Development of the kurtosis κ in space. Start of the step at x = 0. The 95% confidence bounds of the kurtosis obtained from the experiment are shown in black and green with a step and slope respectively. The model prediction is shown with a red dashed line.
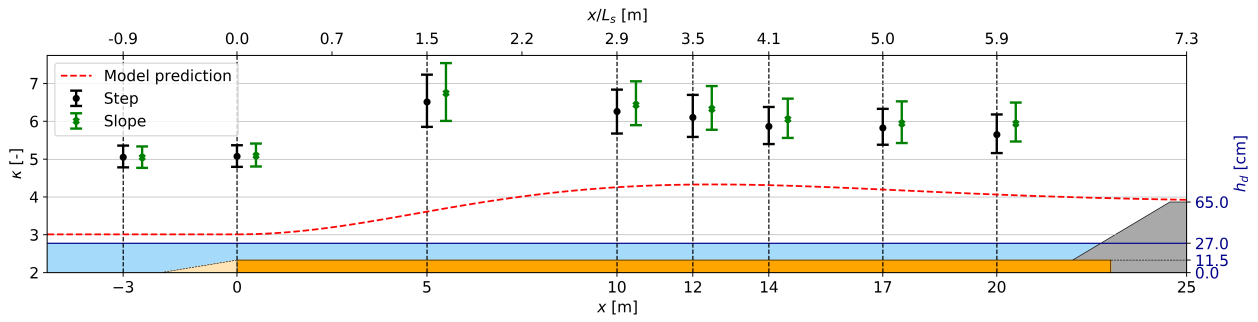
Figure E.9: Test 1a, 2a and 4a bandwidth increase. Development of the kurtosis κ in space. Start of the step at x = 0. The 95% confidence bounds of the kurtosis obtained from the experiment are shown in black, green and purple for tests 1, 2 and 4 with an bandwidth increase respectively. The respective model predictions are shown with a black, green and purple dashed line.
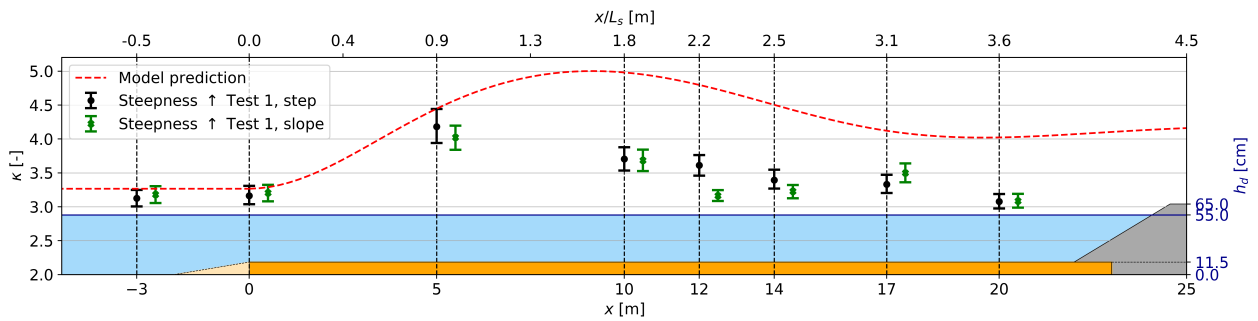
Figure E.10: Test 1b steepness increase. Development of the kurtosis κ in space. Start of the step at x = 0. The 95% confidence bounds of the kurtosis obtained from the experiment are shown in black and green with a step and slope respectively. The model prediction is shown with a red dashed line.
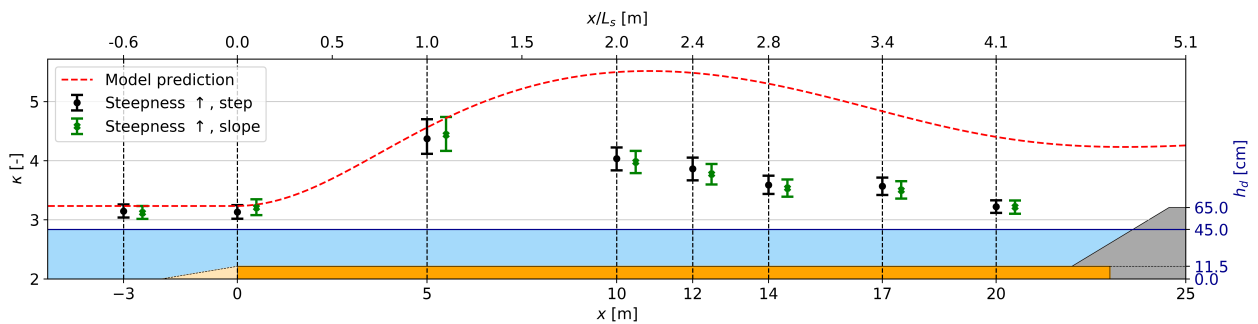
Figure E.11: Test 3a steepness increase. Development of the kurtosis κ in space. Start of the step at x = 0. The 95% confidence bounds of the kurtosis obtained from the experiment are shown in black and green with a step and slope respectively. The model prediction is shown with a red dashed line.
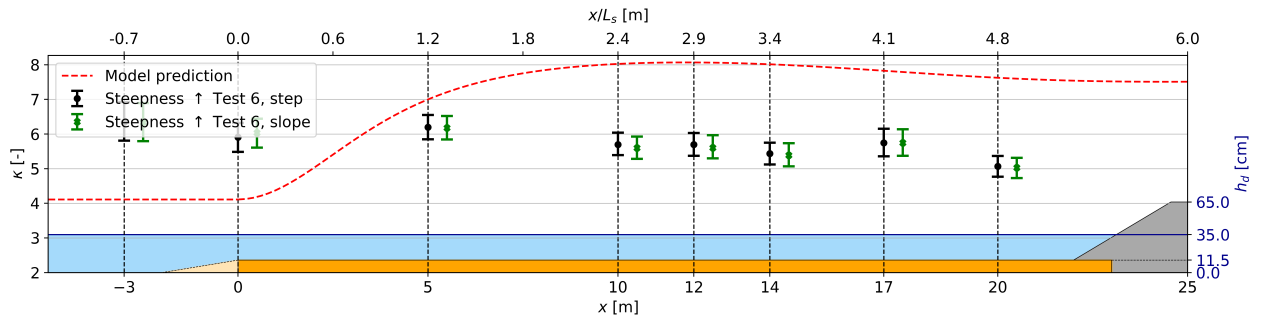
Figure E.12: Test 6a steepness increase. Development of the kurtosis κ in space. Start of the step at $x = 0$. The 95% confidence bounds of the kurtosis obtained from the experiment are shown in black and green with a step and slope respectively. The model prediction is shown with a red dashed line.
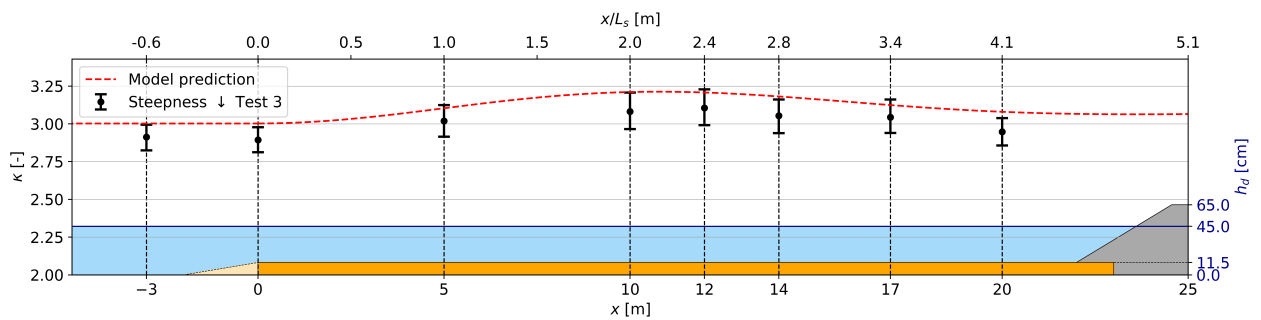
Figure E.13: Test 3b steepness decrease. Development of the kurtosis κ in space. Start of the step at $x = 0$. The 95% confidence bounds of the kurtosis obtained from the experiment are shown in black for a test with a step. The model prediction is shown with a red dashed line.
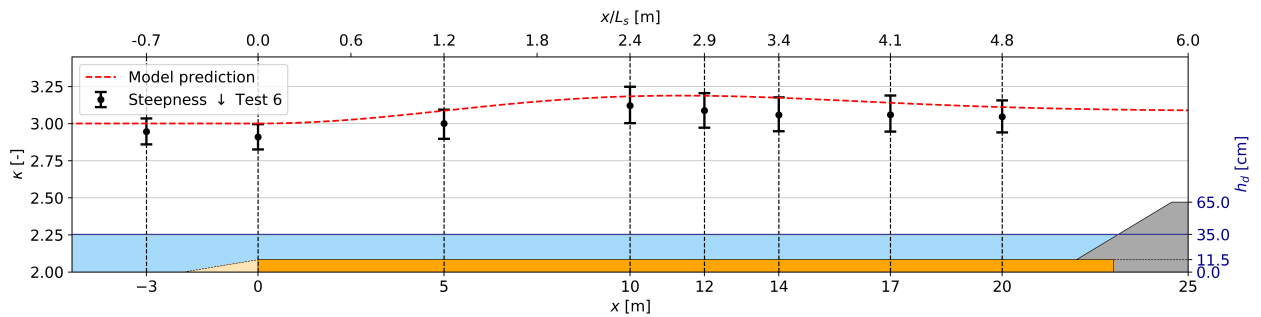
Figure E.14: Test 6b steepness decrease. Development of the kurtosis κ in space. Start of the step at $x = 0$. The 95% confidence bounds of the kurtosis obtained from the experiment are shown in black for a test with a step. The model prediction is shown with a red dashed line.

Additional figures second-order wave generation at TU Delft

In this appendix all figures for the assessment of the second-order wave generation at the Hydraulic Engineering laboratory facility of the TU Delft are presented. Per case (parameters given in table F.1) the following figures are shown:

1. The input time series (wave group to be generated)

2. First-order generation no ARC

3. Super-harmonics first-order generation no ARC

4. Second-order generation no ARC

5. Super-harmonics second-order generation no ARC

6. First-order generation with ARC

7. Second-order generation with ARC

8. Adjusted paddle signal no ARC

9. Adjusted paddle signal with ARC

10. Adjusted paddle signal no ARC in calculated but with ARC during generation (ACS)

11. Spectral analysis

12. Paddle signal analysis

Figure 1 shows the wanted wave group as a function of time. Figures 2 until 10 show the wave group propagating through the flume. The super- and sub-harmonic waves are filtered from the total surface elevation and are multiplied with a factor 5 and 7 respectively with respect to the total surface elevation for visualisation. The y-axis in these figures represent the distance away from the wave paddle. The last wave gauge is thus the top line with 'wiggles'. At the end of the flume, where total reflection takes place, a horizontal black line is drawn. It can clearly be seen that the waves reflect and start travelling back to the wave paddle (bottom of the figure). The propagation speed of the wave groups is shown with a dashed blue line. The speed of the (spurious) free sub-harmonics is indicated as the shallow water speed (the sub-harmonic waves are of such long length that the theory of shallow water depth holds) and is shown with a brown line. The speed of the (spurious) free super-harmonics is indicated as the super-harmonic speed which is calculated using twice the peak frequency. This is also shown with a brown line. Figure 11 can be used to analyse the spectra. The top left plot shows the desired wave group (and its envelope shown in gold). The right plots show the measured wave groups using second-order generation no ARC, with ARC and the adjusted paddle signal ACS from top to bottom respectively. ACS is short for a signal that does not include ARC in the calculation (of the paddle movement file) but does include ARC during generation. The bottom left plot shows the spectra obtained from the wave groups using a 'block' length of 7. This means that the spectral average over 7 discrete frequencies is taken. This enhances visualisation. Figure 12 can be used for analysis of the difference in paddle movement. The top two plots show the first- and second-order steering signal that have been calculated using the AUKE/PC software with respect to time. The bottom plot shows the sub-harmonic second-order paddle movement for second-order generation with and without ARC and the adjusted signals with and without ARC. In addition, theory, explained in section 4.4 is plotted on top to ensure that the theoretical and applied paddle signals match.

Case	kh [-]	T_{peak} [s]	kA [-]
1	1.44	1.25	0.28
2	0.91	1.75	0.1
3	0.53	2.8	0.044

*Table F.1: Parameter overview per case for the second-order generation assessment*

F.1   Case 1
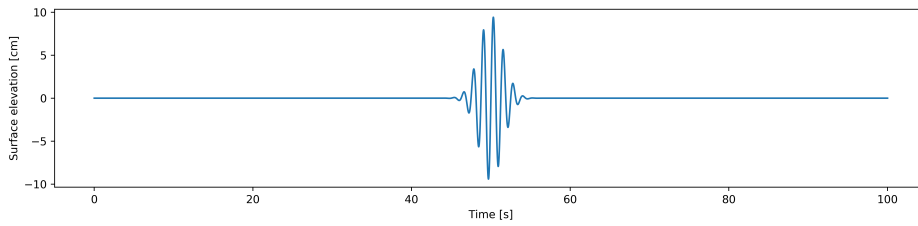
Figure F.1: Case 1, figure 1: input time series with η the surface elevation.
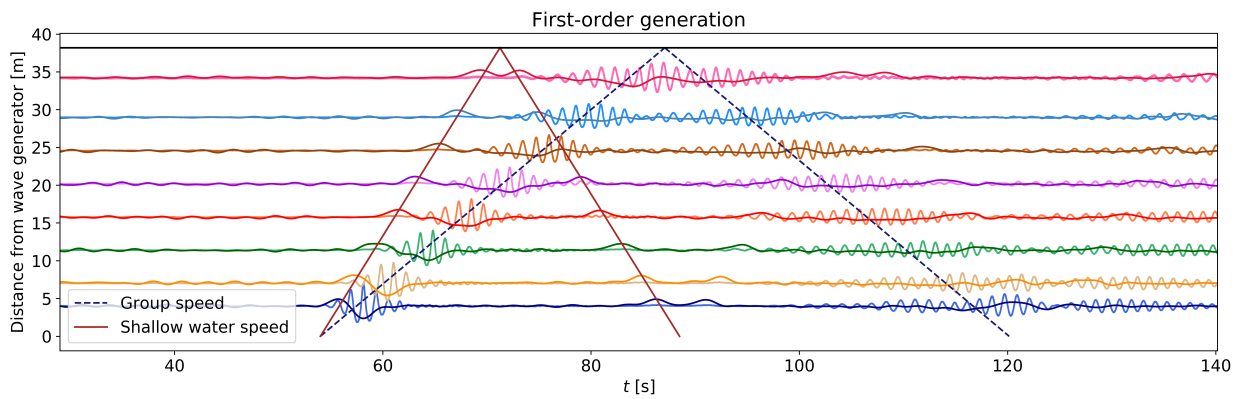
Figure F.2: Case 1, figure 2: first-order wave generation. The total surface elevation (lighter lines) and sub-harmonic waves (darker lines) are shown.
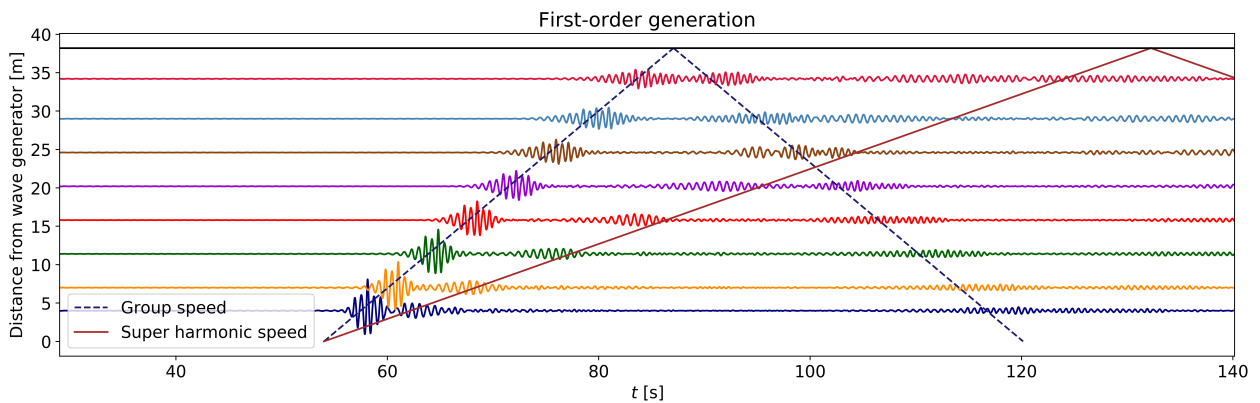
*Figure F.3: Case 1, figure 3: first-order wave generation. Super-harmonic components propagating through the flume are shown.*
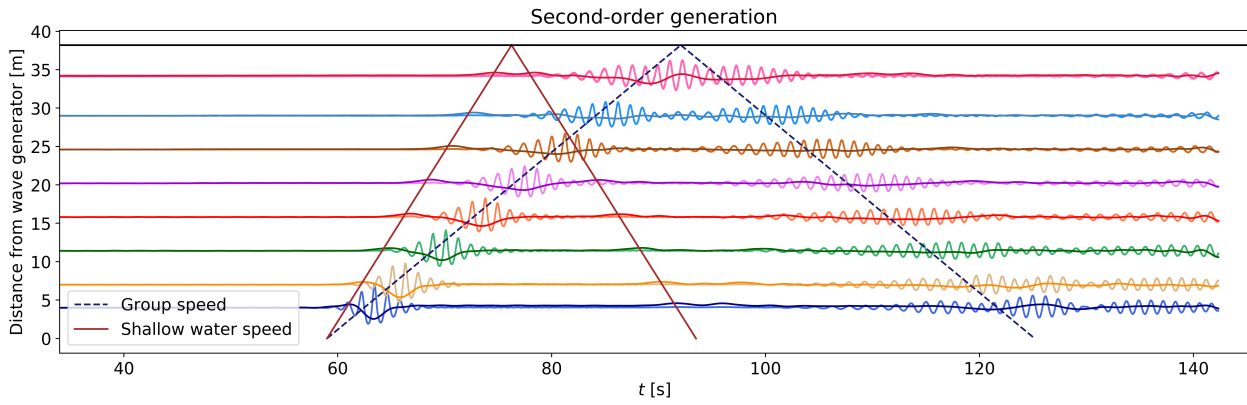
Figure F.4: Case 1, figure 4: second-order wave generation. The total surface elevation (lighter lines) and sub-harmonic waves (darker lines) are shown.
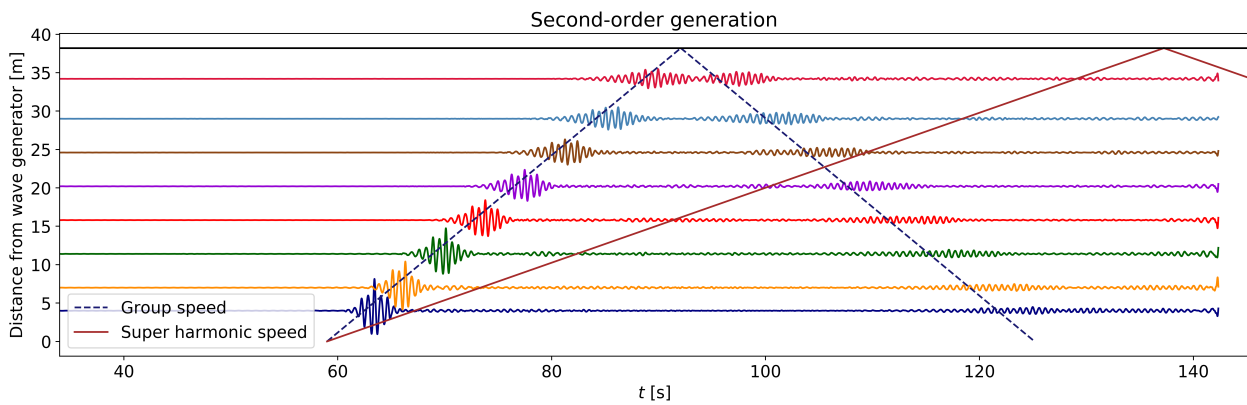

Figure F.5: Case 1, figure 5: second-order wave generation. Super-harmonic components propagating through the flume are shown.
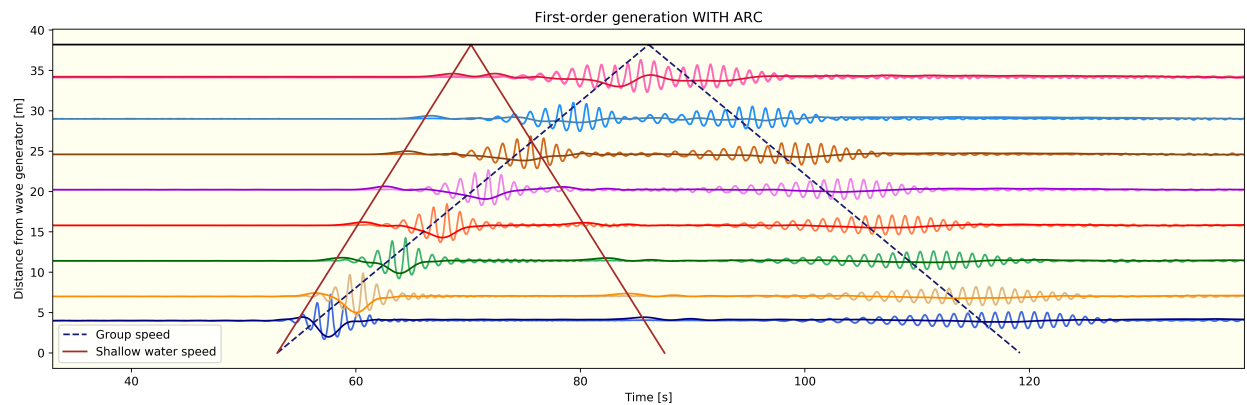
Figure F.6: Case 1, figure 6: first-order wave generation with ARC. The total surface elevation (lighter lines) and sub-harmonic waves (darker lines) are shown.
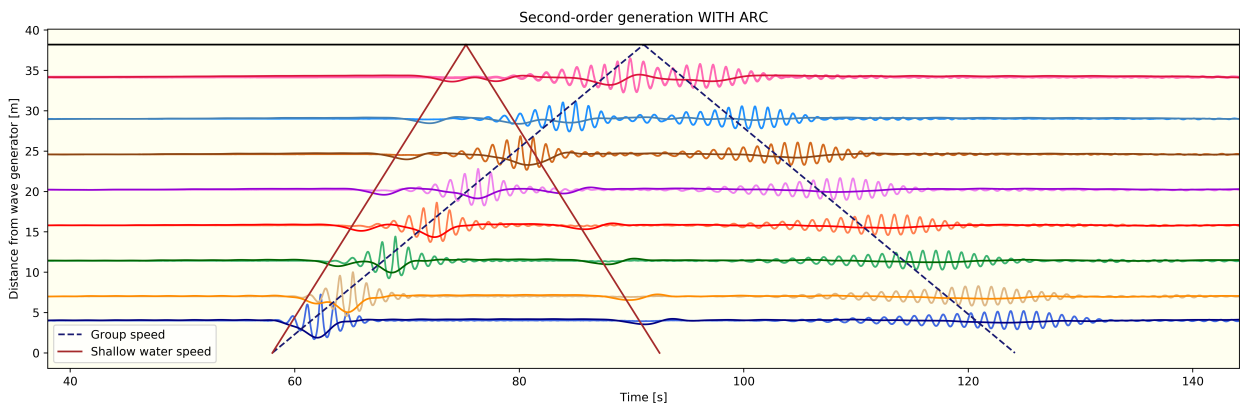
Figure F.7: Case 1, figure 7: second-order wave generation with ARC. The total surface elevation (lighter lines) and sub-harmonic waves (darker lines) are shown.
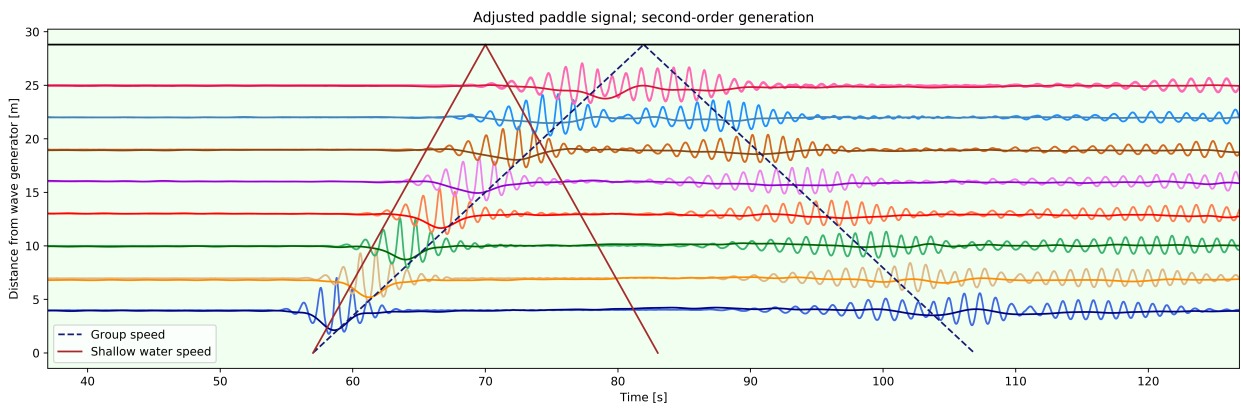
Figure F.8: Case 1, figure 8: adjusted paddle signal no ARC. The total surface elevation (lighter lines) and sub-harmonic waves (darker lines) are shown.
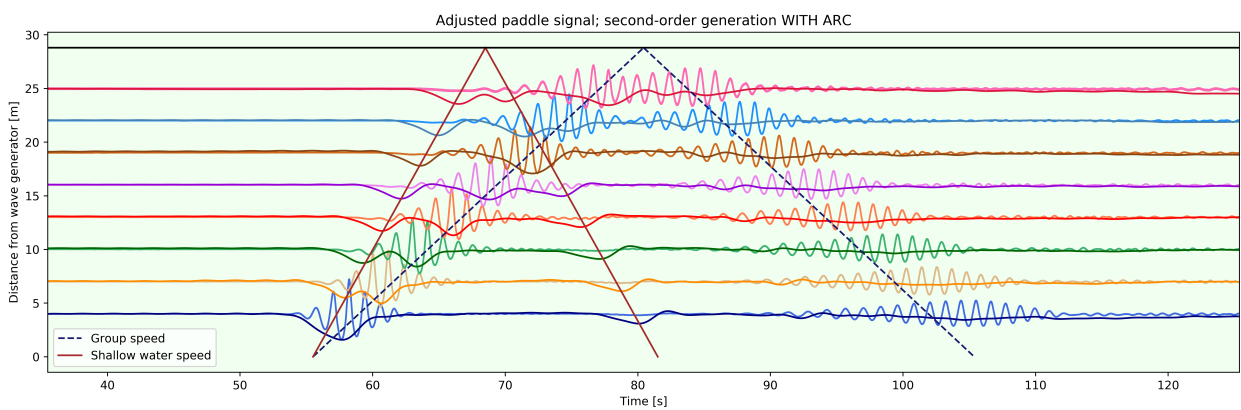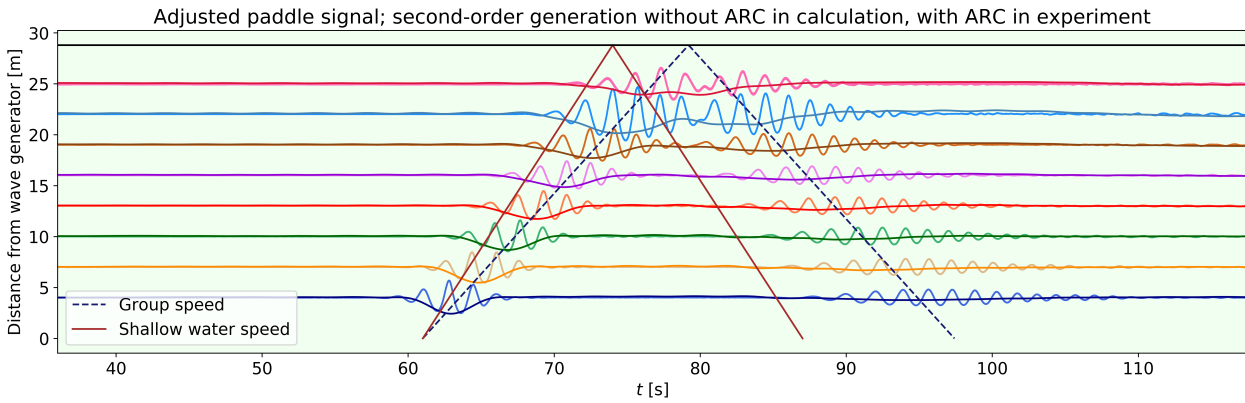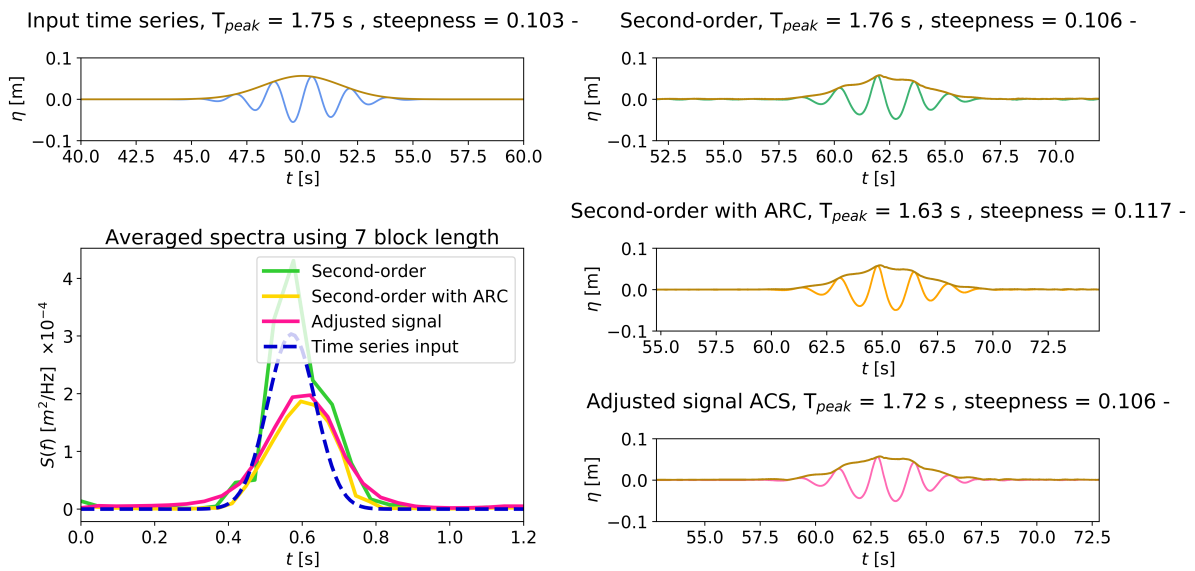

Figure F.9: Case 1, figure 9: adjusted paddle signal with ARC. The total surface elevation (lighter lines) and sub-harmonic waves (darker lines) are shown.
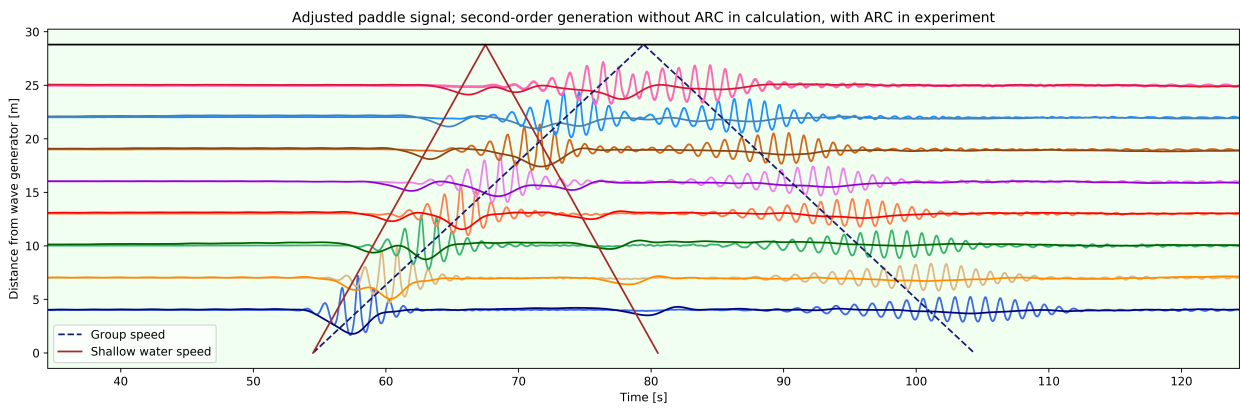
Figure F.10: Case 1, figure 10: adjusted paddle signal ACS. The total surface elevation (lighter lines) and sub-harmonic waves (darker lines) are shown.
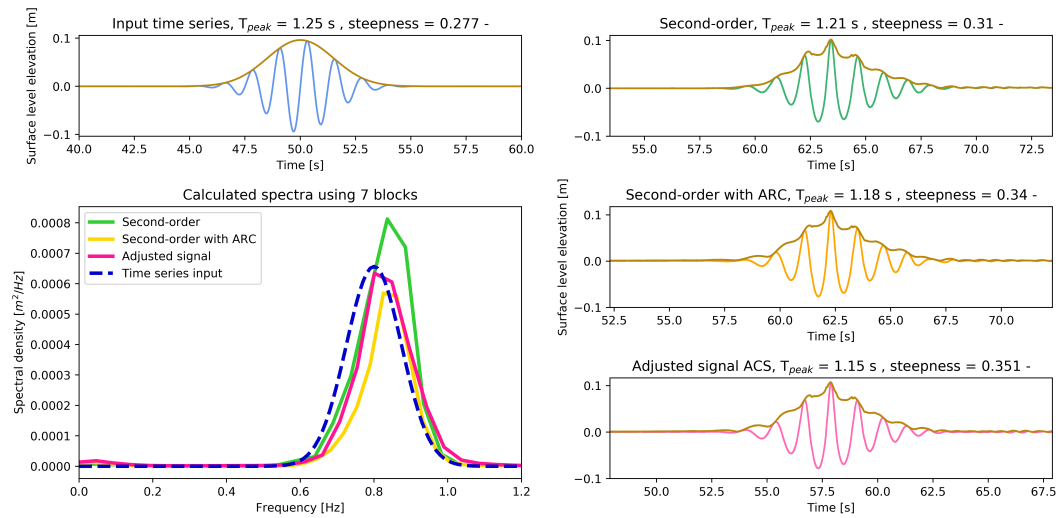
Figure F.11: Case 1, figure 11: spectral analysis
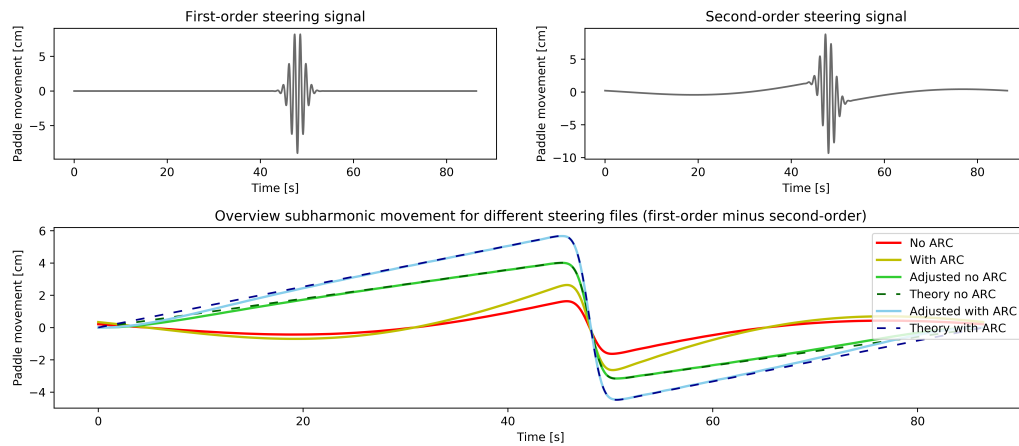
Figure F.12: Case 1, figure 12: wave paddle analysis

F.2   Case 2
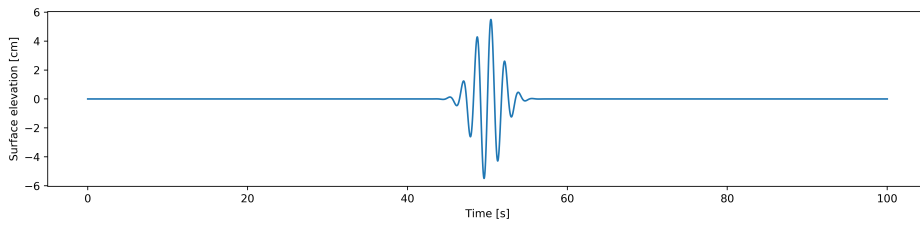
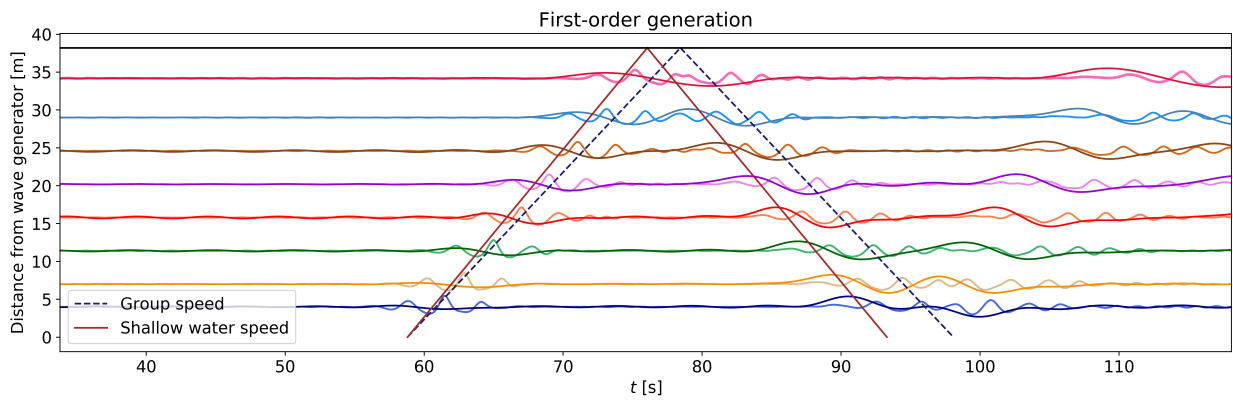Figure F.13: Case 2, figure 1: input time series with η the surface elevation.
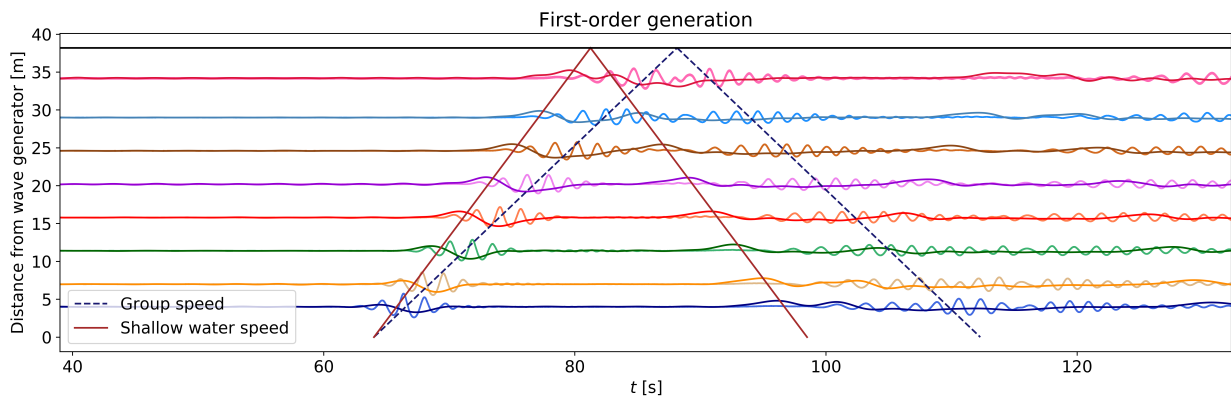
Figure F.14: Case 2, figure 2: first-order wave generation. The total surface elevation (lighter lines) and sub-harmonic waves (darker lines) are shown.
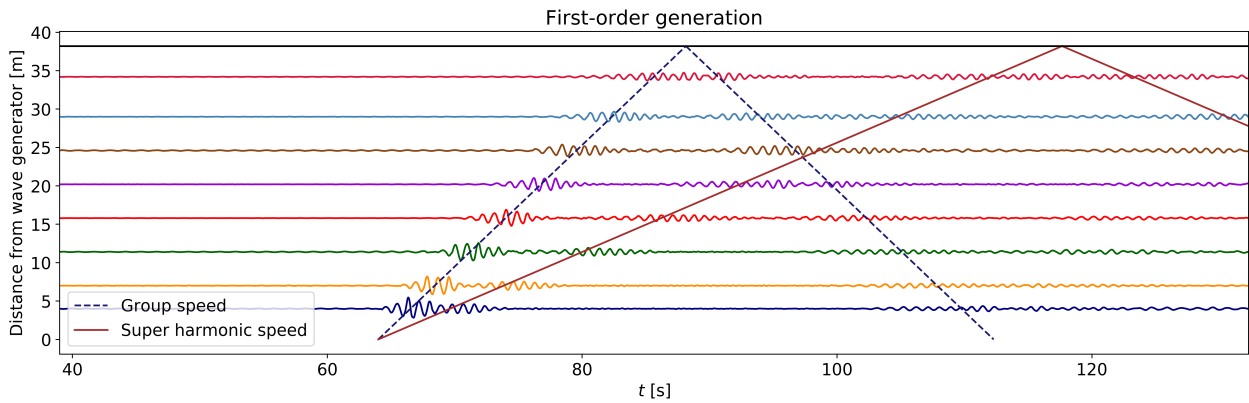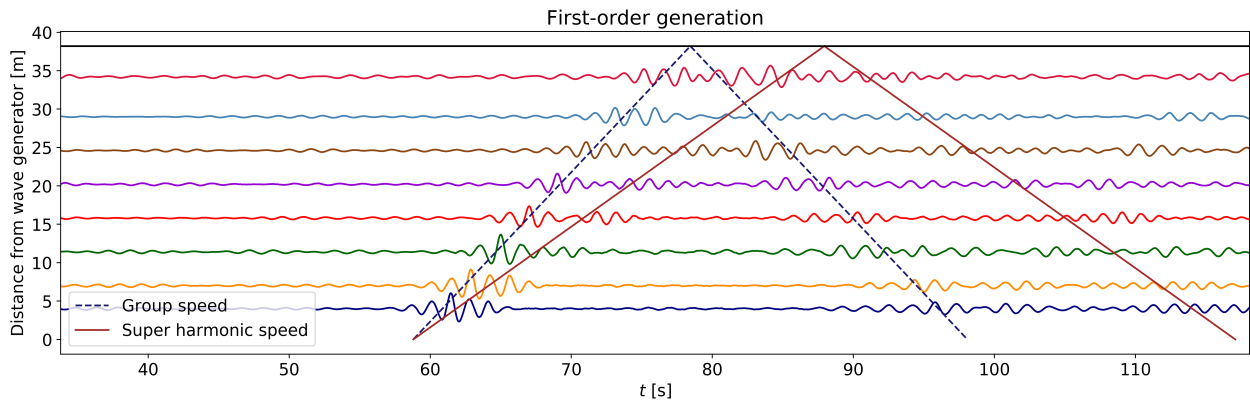

Figure F.15: Case 2, figure 3: first-order wave generation. Super-harmonic components propagating through the flume are shown.
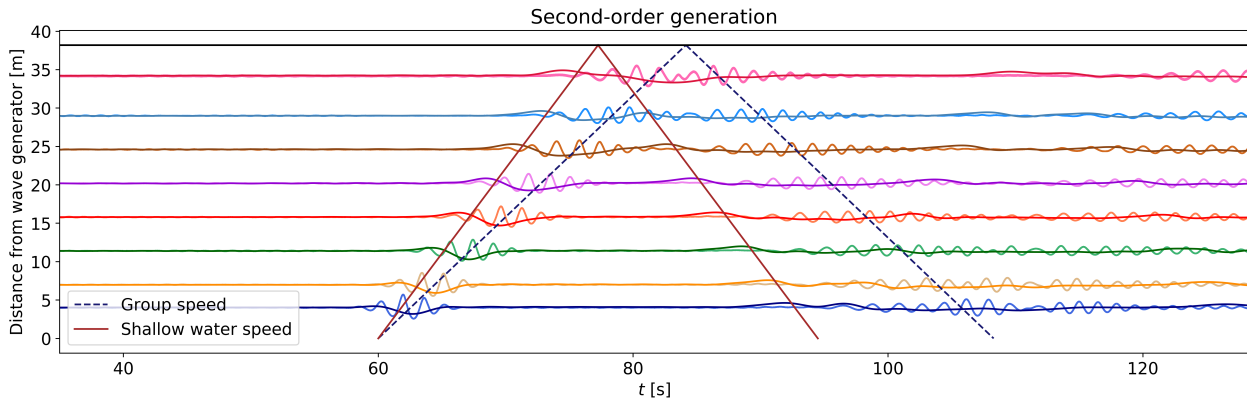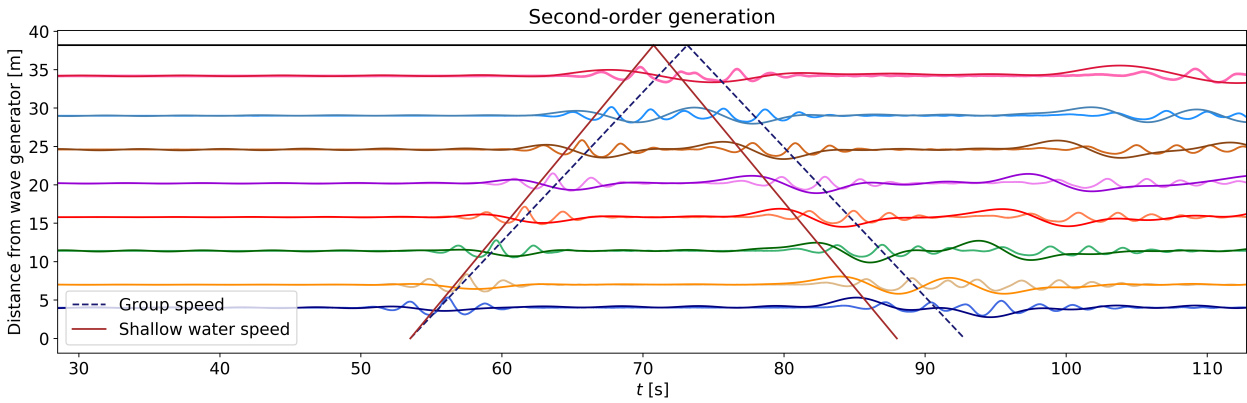
Figure F.16: Case 2, figure 4: second-order wave generation. The total surface elevation (lighter lines) and sub-harmonic waves (darker lines) are shown.
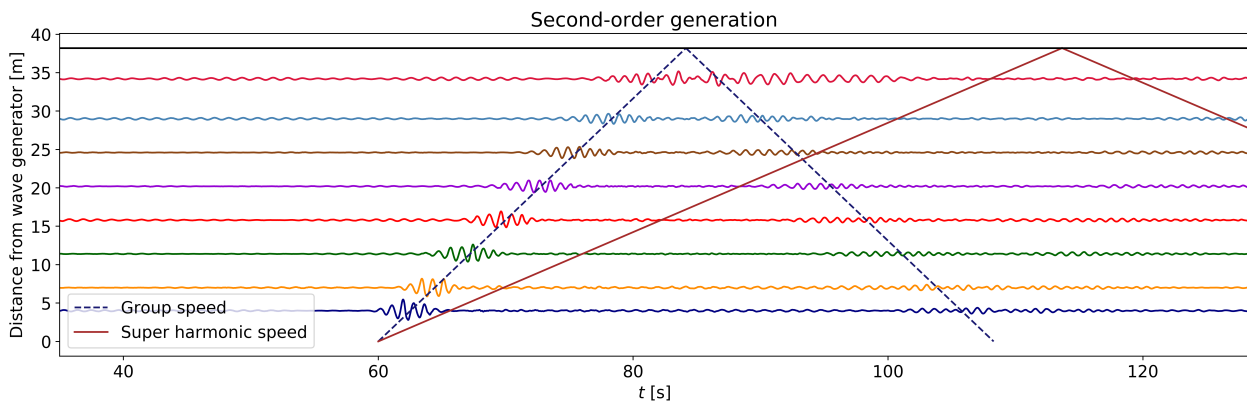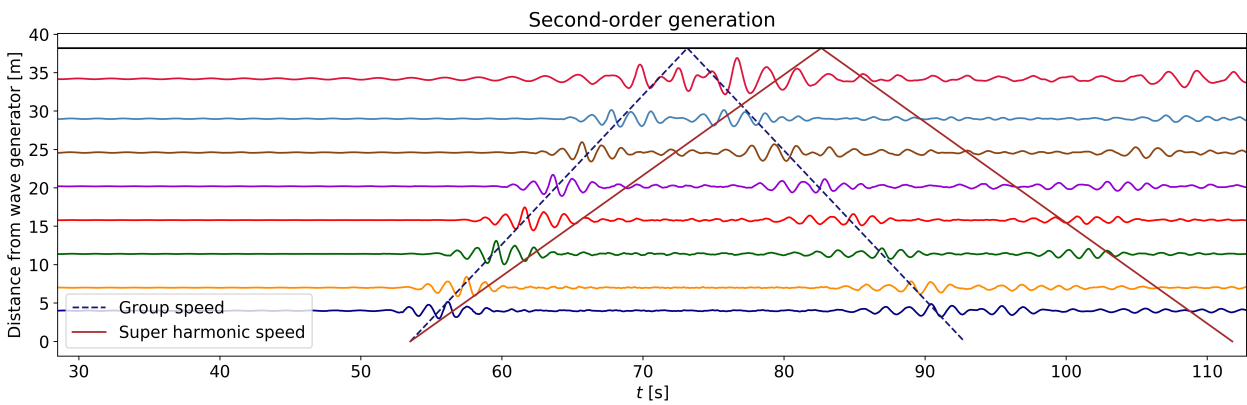

Figure F.17: Case 2, figure 5: second-order wave generation. Super-harmonic components propagating through the flume are shown.
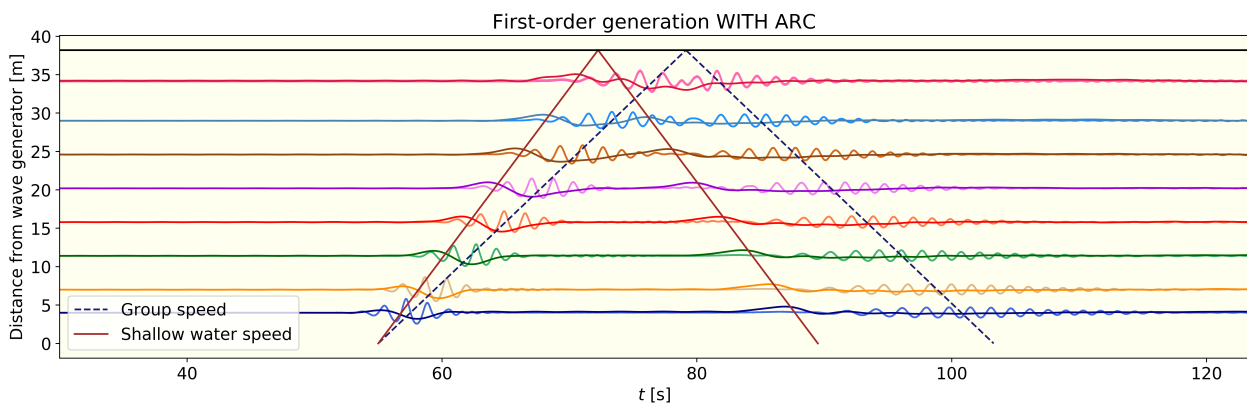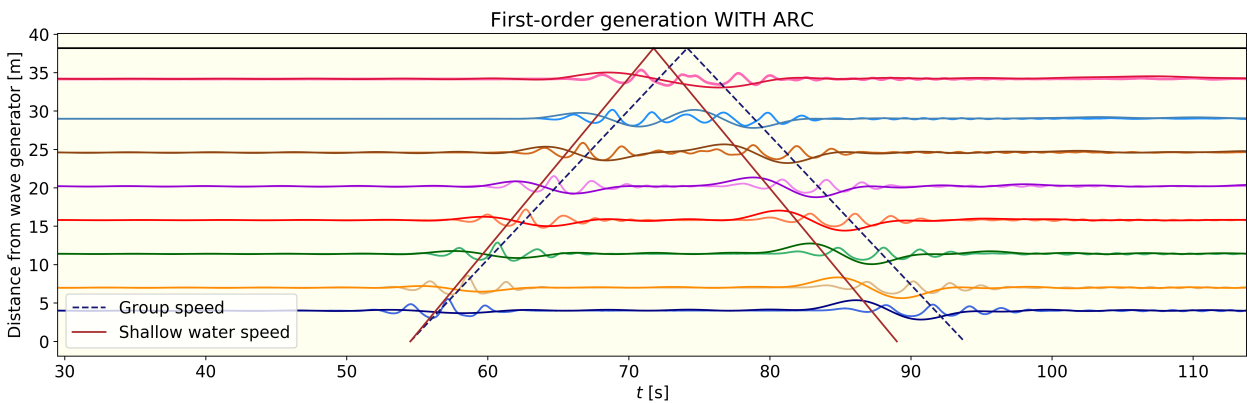

Figure F.18: Case 2, figure 6: first-order wave generation with ARC. The total surface elevation (lighter lines) and sub-harmonic waves (darker lines) are shown.
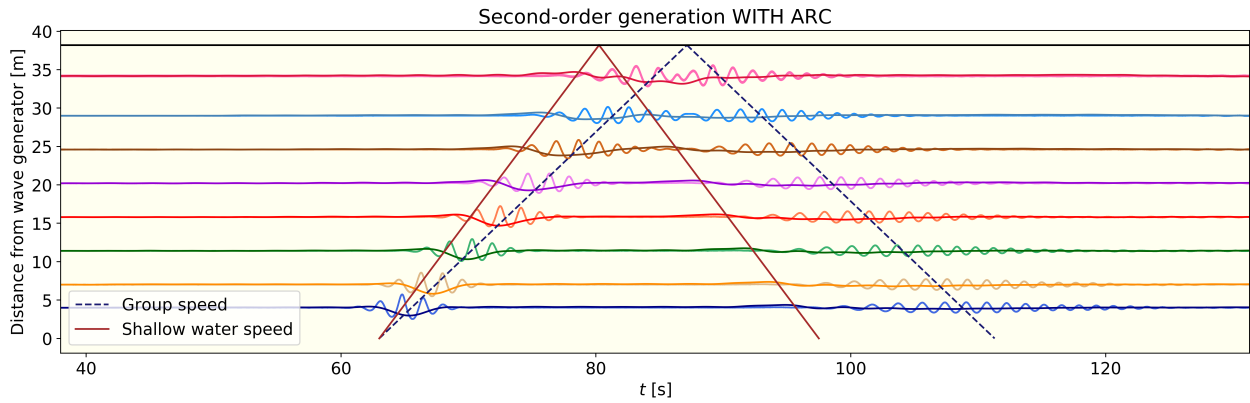
Figure F.19: Case 2, figure 7: second-order wave generation with ARC. The total surface elevation (lighter lines) and sub-harmonic waves (darker lines) are shown.
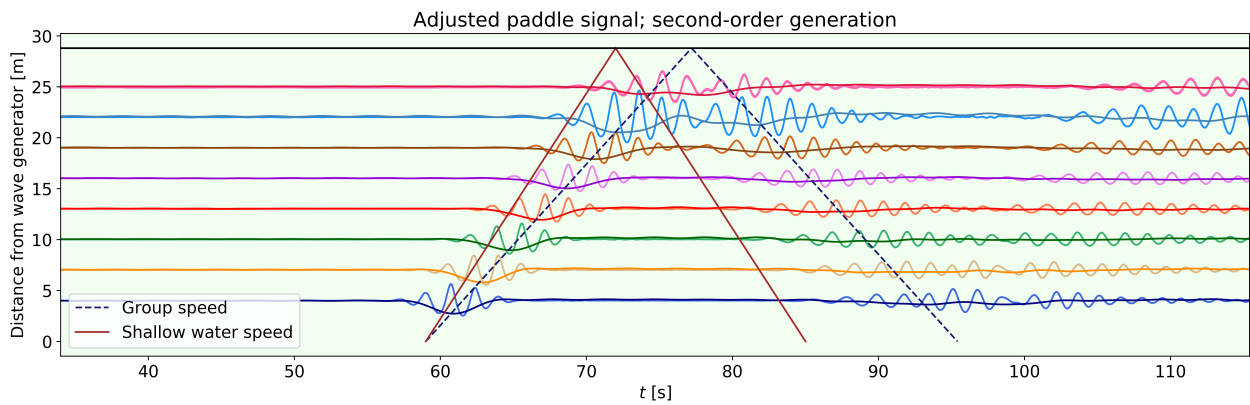
Figure F.20: Case 2, figure 8: adjusted paddle signal no ARC. The total surface elevation (lighter lines) and sub-harmonic waves (darker lines) are shown.
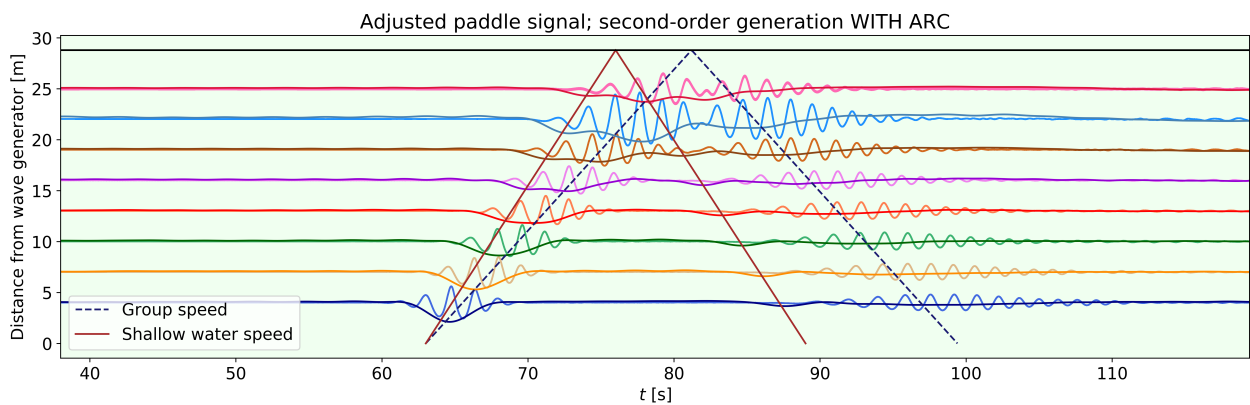
Figure F.21: Case 2, figure 9: adjusted paddle signal with ARC. The total surface elevation (lighter lines) and sub-harmonic waves (darker lines) are shown.

Figure F.22: Case 2, figure 10: adjusted paddle signal ACS. The total surface elevation (lighter lines) and sub-harmonic waves (darker lines) are shown.

Figure F.23: Case 2, figure 11: spectral analysis
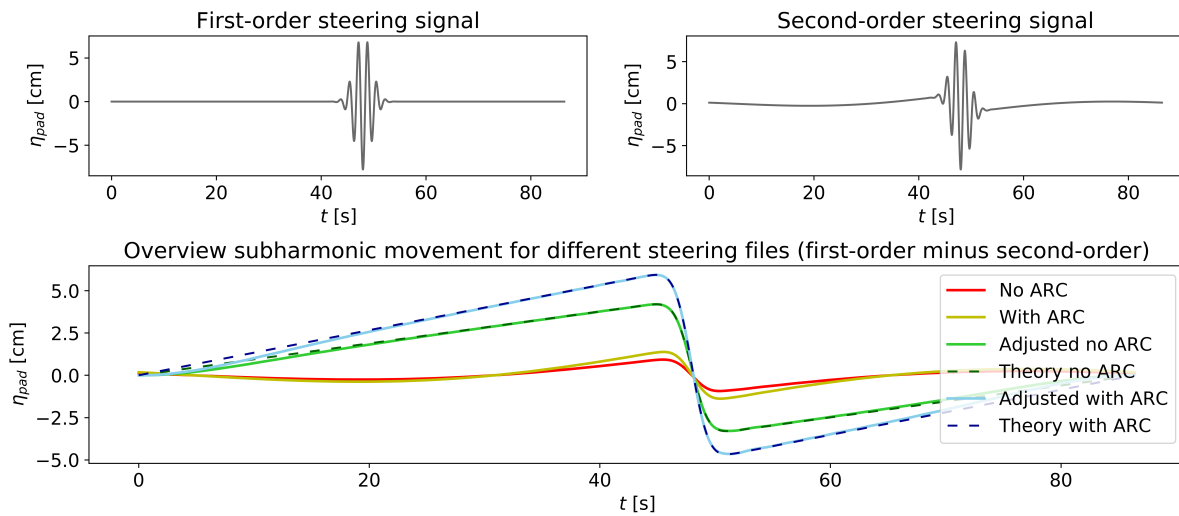
Figure F.24: Case 2, figure 12: wave paddle analysis

F.3 Case 3
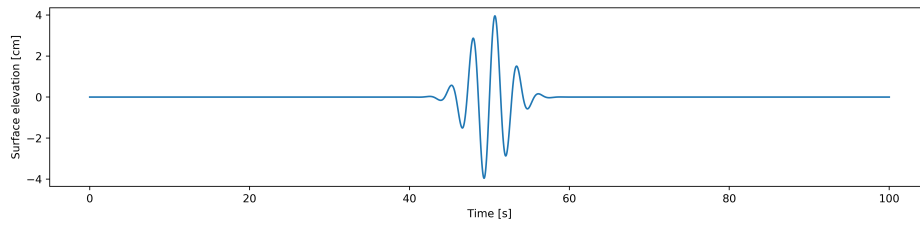
Figure F.25: Case 3, figure 1: input time series with η the surface elevation.

Figure F.26: Case 3, figure 2: first-order wave generation. The total surface elevation (lighter lines) and sub-harmonic waves (darker lines) are shown.

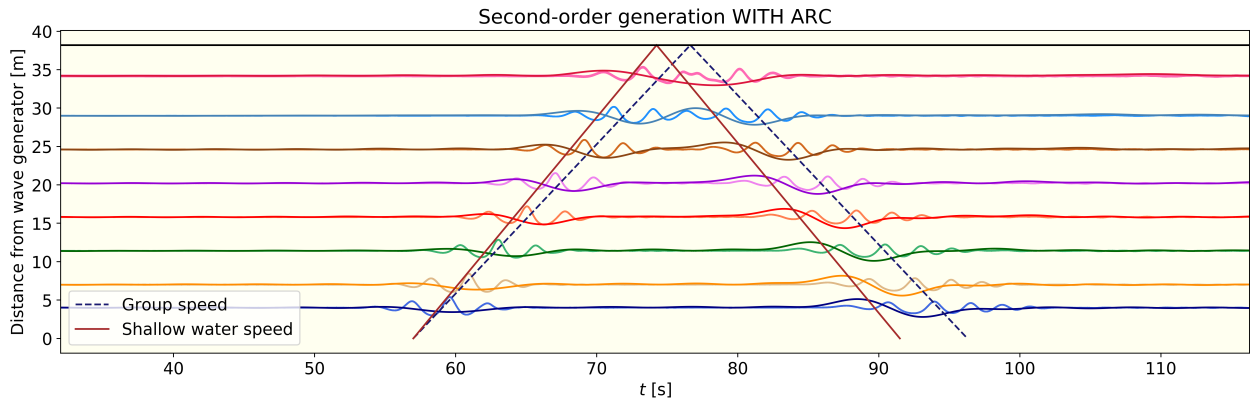Figure F.27: Case 3, figure 3: first-order wave generation. Super-harmonic components propagating through the flume are shown.

Figure F.28: Case 3, figure 4: second-order wave generation. The total surface elevation (lighter lines) and sub-harmonic waves (darker lines) are shown.


Figure F.29: Case 3, figure 5: second-order wave generation. Super-harmonic components propagating through the flume are shown.

Figure F.30: Case 3, figure 6: first-order wave generation with ARC. The total surface elevation (lighter lines) and sub-harmonic waves (darker lines) are shown.

Figure F.31: Case 3, figure 7: second-order wave generation with ARC. The total surface elevation (lighter lines) and sub-harmonic waves (darker lines) are shown.
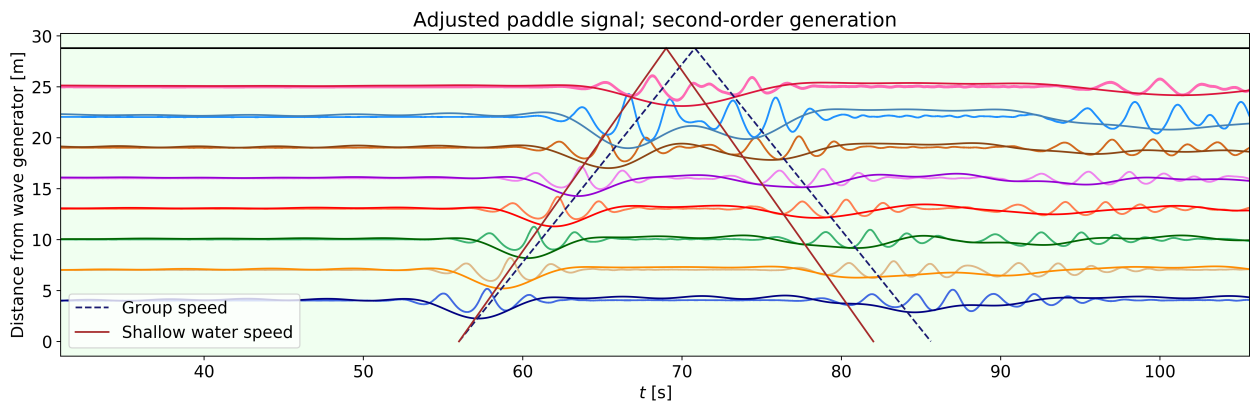
Figure F.32: Case 3, figure 8: adjusted paddle signal no ARC. The total surface elevation (lighter lines) and sub-harmonic waves (darker lines) are shown.
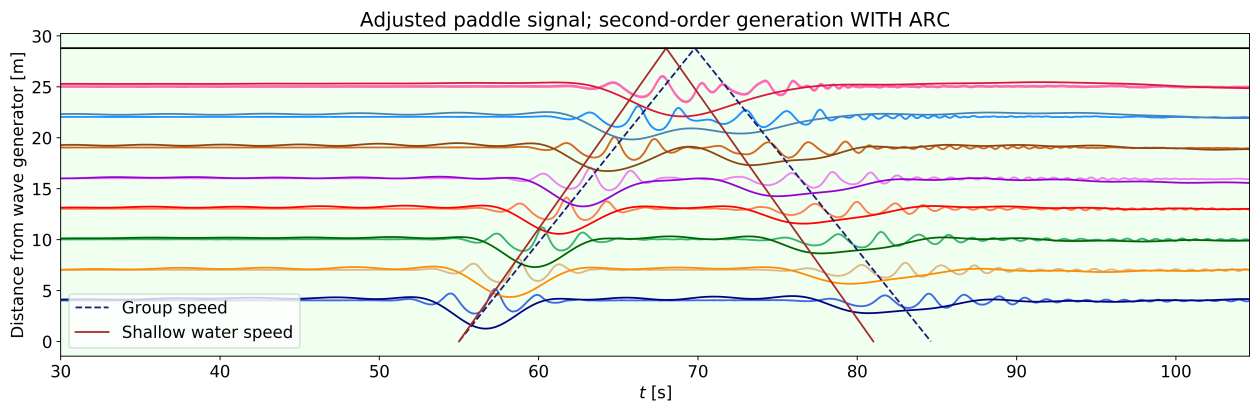

Figure F.33: Case 3, figure 9: adjusted paddle signal with ARC. The total surface elevation (lighter lines) and sub-harmonic waves (darker lines) are shown.
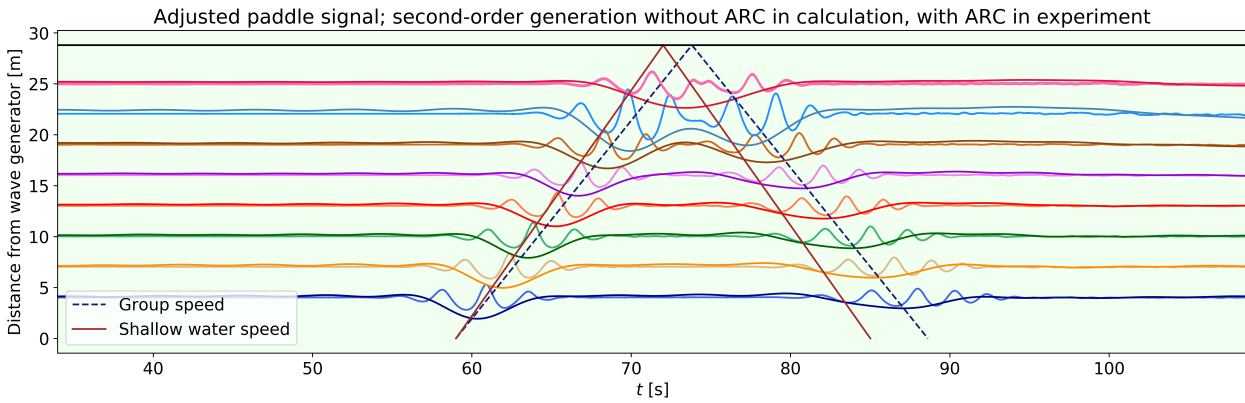
Figure F.34: Case 3, figure 10: adjusted paddle signal ACS. The total surface elevation (lighter lines) and sub-harmonic waves (darker lines) are shown.
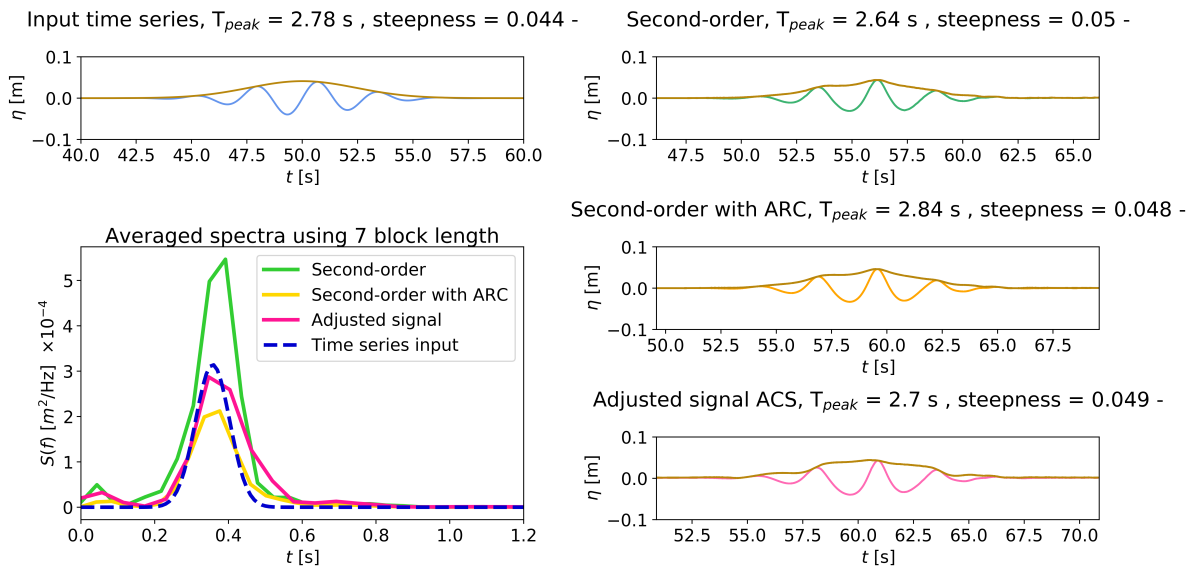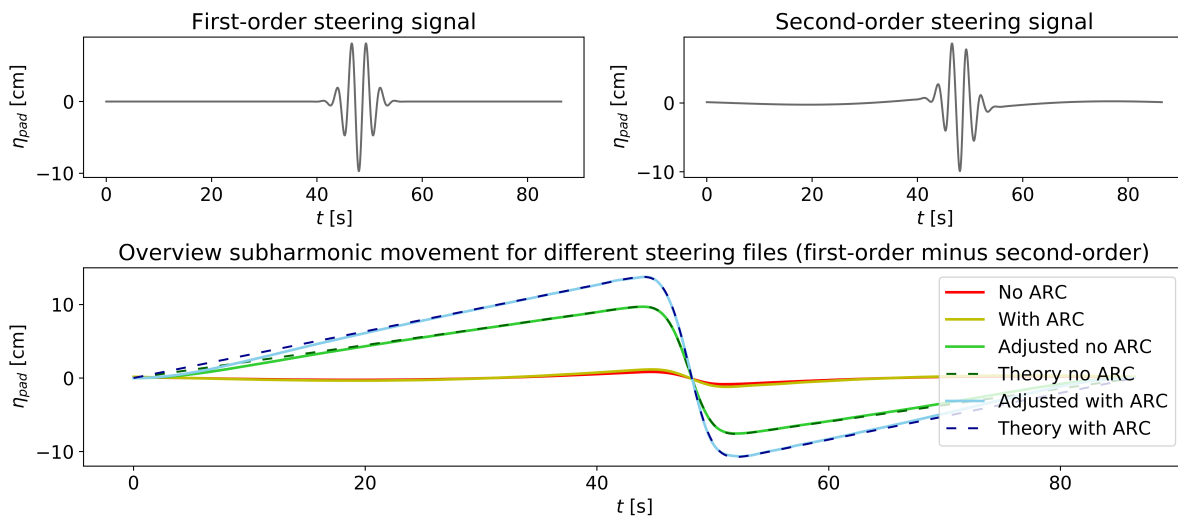

Figure F.35: Case 3, figure 11: spectral analysis

Figure F.36: Case 2, figure 12: wave paddle analysis